# FABRICATION OF ZINC OXIDE MICRO-NANOSTRUCTURES AND THEIR APPLICATIONS IN GAS SENSING AND NANOCOMPOSITES

by

**Hongbin Cheng**

BS, Tsinghua University, P.R. China, 1995

MS, Tsinghua University, P.R. China, 1998

MS, National University of Singapore,Singapore, 2000

Submitted to the Graduate Faculty of

the Swanson School of Engineering in partial fulfillment

of the requirements for the degree of

Doctor of Philosophy

University of Pittsburgh

2009

UNIVERSITY OF PITTSBURGH

SWANSON SCHOOL OF ENGINEERING

This dissertation was presented

by

Hongbin Cheng

It was defended on

August 25, 2009

and approved by

Dr. John A. Barnard, Professor, Department of Mechanical Engineering and Materials Science

Dr. William S. Slaughter, Associate Professor, Department of Mechanical Engineering and Materials Science

Dr. Patrick Smolinski, Associate Professor, Department of Mechanical Engineering and Materials Science

Dr. Jiping Cheng, Research Assistant Professor, Department of Materials Research Institute, Pennsylvania State University

Dissertation Director: Dr. Qing-Ming Wang, Associate Professor, Department of Mechanical Engineering and Materials Science

**FABRICATION OF ZINC OXIDE MICRO-NANOSTRUCTURES AND THEIR APPLICATIONS IN GAS SENSING AND NANOCOMPOSITES**

Hongbin Cheng, PhD

University of Pittsburgh, 2009

To date, one-dimensional ZnO micro/nanostructures have been attracting much attention for wide potential applications due to their unique electrical, piezoelectric, optoelectronic, and photochemical properties. The overall objective of this dissertation is to grow various ZnO micro and nanostructures using a novel microwave thermal evaporation-deposition approach, to explore the application of ZnO nanostructures in gas sensing, and to fabricate and characterize multifunctional ZnO nanowires-polyimide nanocomposite. Therefore, three parts were included in this study: (1) A novel thermal evaporation-deposition method using microwave energy was investigated. Batch of ZnO structures including microtubes, microrods, nanotubes, nanowires and nanobelts have been successfully synthesized in the microwave system with a unique source materials-substrate configuration and a desirable temperature profile. These products are pure, structurally uniform, and single crystalline. The photoluminescence (PL) exhibits strong ultraviolet emission at room temperature, indicating potential applications for short-wave light-emitting photonic devices. (2) Piezoelectric crystal langasite bulk acoustic wave (LGS) resonator based high temperature gas sensor was fabricated. Ordered ZnO nanowire arrays were grown on the langasite resonator as the sensitive layer by two-step hydrothermal method at low temperature. The gas sensor coated with ZnO nanowire arrays exhibited good sensitivity to $NO_2$ and $NH_3$. The response of the sensor is fast due to the large surface area of ZnO nanowires. In addition, this work demonstrates that the combination of nanowire arrays with langasite

thickness shear mode resonators could provide a promising high temperature gas sensing platform with both high sensitivity and enhanced response speed. (3) The nanocomposite with controlled alignment of ZnO nanowires in the polyimide matrix was achieved using self-alignment method and external electric field assisted method. For the the self-alignment process, the morphologies of the designed nanocomposites were dramatically influenced by the viscosity of the polymer and the geometrical structure of ZnO nanowires. For the nanocomposite prepared by the electric field assisted alignment, the density and the alignment degree of ordered ZnO nanowires significantly depended on the magnitude and the frequency of the applied ac electric field. The DC offset voltage had strong effect on the deposition sites of nanowires. The resultant nanocomposite devices exhibited great dielectric constant and conductivity enhancement at room temperature due to the interfacial effect between ZnO nanowires and the polymer matrix. These nanocomposites combining the superb properties of ZnO nanowires with the polyimide matrix provide a smart material candidate for multifunctional applications that require self-sensing and self-actuation capabilities. The self-alignment method and electric field assisted alignment method also provide a bright route to combine superb properties of nanomaterials with the lightweight, flexibility, and manufacturability of dielectric polymers for future generations of multifunctional materials.

## TABLE OF CONTENTS

## LIST OF TABLES

## LIST OF FIGURES

## ACKNOWLEDGEMENTS

First I would like to express my sincere appreciation to my advisor, Dr. Qing-Ming Wang, for his guidance, support, and encouragement throughout my dissertation work. He is a wonderful person and a great mentor. His optimism, patience and words of kindness have made my doctoral experience immensely enjoyable.

I would like to thank my committee members, Dr. John A. Barnard, Dr. William S. Slaughter, Dr. Patrick Smolinski, and Dr. Jiping Cheng. Thank you for your time and constructive criticisms for this thesis. Dr. Cheng deserves special acknowledgement for his useful discussion and help in the fabrication of ZnO nanostructures using microwave energy.

I also would thank all my group members: Tao Zhang, Qingming Chen, Fang Li, Lifeng Qin, Qian Chen, Chengliang Sun, Shaying Hu, and Jie Huang. In particular, I appreciate the contribution of Lifeng's work on devices measurement and characterization.

Lastly, I have to give my thanks to my parents, whose supports were essential in getting me to where I am today, have shared with me the ups and downs in my life. Of course, it is my honor to dedicate this thesis to my dear wife Ranhui Duan. Her support, encouragement and companionship have turned my life into a pleasant journey during my PhD study.

# 1.0 INTRODUCTION

To date, one-dimensional ZnO micro/nanostructures have been attracting much attention for wide potential applications due to their unique electrical, piezoelectric, optoelectronic, and photochemical properties. This dissertation includes three parts on ZnO nanomaterials: growing ZnO micro-and nano-structures using microwave thermal evaporation-deposition approach, exploring the application of ZnO nanostructures for gas sensing and fabricating multifunctional ZnO nanowires/polymer nanocomposites. In this chapter, background information on these three topics will be reviewed first.

## 1.1 ZINC OXIDE AND VARIETIES OF SYNTHESIS TECHNIQUES

### 1.1.1 General material properties of zinc oxide

Zinc oxide (ZnO) is a piezoelectric, transparent, semiconducting oxide. It is widely used as a catalyst [1], sensor [2], piezoelectric transducer [3], surface acoustic wave propagator [4], and photonic material [5]. With a wide bandgap of 3.37 eV and a large excitation binding energy (60 meV), ZnO exhibits near-UV emission, and resistance to high temperature electronic degradation. In addition, ZnO is the hardest of the II-VI semiconductors (therefore more resistant to wear), as well as one of the most piezoelectric semiconductors ($d_{33}$ = 12.4 x $10^{-12}$ C/N). ZnO

crystallizes in three forms: hexagonal wurtzite, cubic zincblende, and the rarely observed cubic rocksalt. The non-centrosymmetric wurtzite is the most common crystal structure with polar surfaces [6]. The structure of ZnO can be simply described as a series of alternating planes composed of tetrahedrally coordinated $Zn^{2+}$ and $O^{2-}$ ions, stacking alternatively along the c-axis (Figure 1.1) [7]. The Zn-O distance is 1.922Å parallel to the c-axis and 1.973Å in the other three directions of the tetrahedral arrangements of nearest neighbors. The lack of the inversion symmetry in the ZnO tetrahedral structure is the origin of its piezoelectricity and pyroelectricity. Another important feature of ZnO is polar surfaces. The most common polar surface is the basal plane. The oppositely charged ions produce positively charged $Zn^{-}$ (0001) and negatively charged $O^{-}$ $(000\bar{1})$ surfaces, resulting in a spontaneous polarization along the c-axis and vastly different properties in Zn-terminated and O-terminated plane. The other two commonly observed facets for ZnO are $\{2\bar{1}\bar{1}0\}$ and $\{011\bar{0}\}$, which are non-polar surfaces and have lower energy than the {0001} facets.

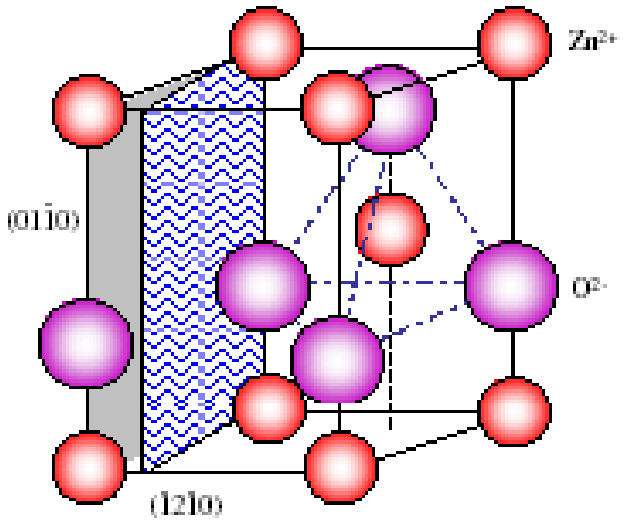


**Figure 1.1.** Wurtzite structural model of ZnO [7]

### 1.1.2 Zinc oxide nanostructure synthesis techniques

ZnO has been under intensive investigation since the 1950s. In particular, with the advance of the nanotechnology in the recent years, one-dimensional (1D) ZnO nanostructures have received broad attention due to unique electrical, optical, chemical and mechanical properties compared to their bulk (3D), thin film (2D) and nanoparticles (0D) counterparts. A variety of methods exist for 1D ZnO nanostructures growth. For consolidation, methods have been categorized as either vapor transport synthesis [8], or solution-based chemistry synthesis [9].

**Vapor Transport Synthesis**

In vapor transport synthesis, Zn and oxygen or oxygen mixture vapor are transported and react with each other, forming ZnO nanostructures. There are several ways to generate Zn and oxygen vapor. Decomposition of ZnO is a direct and simple method [10]. However, it is limited to very high temperatures (~1400°C). Another direct method is to heat up Zn powder under oxygen flow [11]. This method facilitates relative low growth temperature (500~700°C), but the ratio between the Zn vapor pressure and oxygen pressure needs to be carefully controlled in order to obtain desired ZnO nanostructures. It has been observed that the change of this ratio contributes to a large variation on the morphology of nanostructures. The indirect methods to provide Zn vapor include metal-organic vapor phase epitaxy [12] and carothermal method [13]. For metal-organic vapor phase epitaxy, organometallic Zn compound, diethyl-zinc, is used under appropriate oxygen or $N_2O$ flow. For the widely used carbothermal method, ZnO powder is mixed with graphite powder as source material. At about 800-1100 °C, graphite reduces ZnO to form Zn and $CO/CO_2$ vapors. Zn and $CO/CO_2$ later react and result in ZnO nanocrystals. The

advantages of this method lie in that the existence of graphite significantly lowers the decomposition temperature of ZnO.

According to the difference on nanostructure formation mechanisms, the extensively used vapor transport process can be categorized into the catalyst free vapor-solid (VS) process and catalyst assisted vapor-liquid-solid (VLS) process. Synthesis utilizing VS process is usually capable of producing a rich variety of nanostructures, including nanowires, nanorods, nanobelts and other complex structures [10]. In this process, ZnO powder was decomposed into $Zn^{2+}$ and $O^{2-}$ at ~1350 °C, then under Ar carrier gas, nanostructures were deposited onto an alumina substrate at a low temperature zone.

Although diverse nanostructures can be obtained in the VS process, this method obviously provides less control on the geometry, alignment and precise location of ZnO nanostructures. Controlled growth of ZnO nanostructures has been achieved by catalyst assisted VLS process [13].In this process, various nanoparticles or nanoclusters have been used as catalysts, the formation of eutectic alloy droplet occurs at each catalyst site, followed by the nucleation and growth of solid ZnO nanowire due to the supersaturation of the liquid droplet. Incremental growth of the nanowire taking place at the droplet interface constantly pushes the catalyst upwards. Thus, such growth method inherently provides site-specific nucleation at each catalytic site.

**Solution-based chemistry synthesis**

Solution-based chemistry synthesis is defined by any chemical reaction that requires a liquid. As a generic method for synthesis, this method has been vital to the production of a diversity of materials that are often difficult to make using vapor transport synthesis. Typically,

solution-based methodologies provide materials with high yield and uniformity. The most important and common techniques for ZnO synthesis are hydrothermal [14] and sol-gel synthesis [15].

Hydrothermal synthesis is a subset of solvothermal synthesis which involves water at elevated conditions (temperature and pressure). The basic principle is that small crystals will homogeneously nucleate and grow from solution when subjected to high temperatures and pressures. During the nucleation and growth process, water is both a catalyst and occasionally a solid-state phase component. Under the extreme conditions of the synthesis vessel (autoclave or bomb), water often becomes supercritical, thereby increasing the dissolving power, diffusivity, and mass transport of the liquid by reducing its viscosity. In addition, the ability to tune the pressure of the vessel provides an avenue to tailor the density of the final product. When compared to other methodologies, hydrothermal synthesis is environmentally benign, inexpensive, and allows for the reduction of free energies for various equilibriums. Materials that are made hydrothermally are generally high-quality, single crystals with a diversity of shapes and sizes. Although hydrothermal synthesis is an established synthesis route within the ceramics industry, it has recently been rekindled within the scientific community by synthesizing one-dimensional nanostructures, such as carbon nanotubes and oxide nanowires. As of recent, hydrothermal synthesis has been used to synthesize well-aligned ZnO nanorods on GaN substrates for optical applications [14].

The sol-gel process, as the name implies, involves the evolution of inorganic networks through the formation of a colloidal suspension (sol) and gelation of the sol to form a network in a continuous liquid phase (gel). The precursors for synthesizing these colloids consist of a metal/metalloid surrounded by various reactive ligands. Metal alkoxides are most popular

because they react readily with water. At the functional group level, three reactions are generally used to describe the sol-gel process: hydrolysis, alcohol condensation, and water condensation. However, the characteristics and properties of a particular sol-gel inorganic network are related to a number of factors that affect the rate of hydrolysis and condensation reactions, such as pH, temperature and time of reaction, reagent concentrations, catalyst nature and concentration, aging temperature and time, and drying. ZnO nanorods have been synthesized with preferred crystallographic orientations using the sol-gel method [15].

## 1.2 MICROWAVE PROCESSING OF MATERIALS

Microwaves are electromagnetic radiation with wavelengths ranging from about 1 mm to 1 m and frequencies between 300 MHz to 300 GHz, respectively. However, only very few frequency bands in this range are allowed for research and industrial applications to avoid interference with frequency bands used in telecommunication. The most common microwave frequency used for research is 2.45 GHz; the other allowable frequencies are 915 MHz, 30 GHz, and 83 GHz for some specific applications. Microwave energy has been in use for over 50 years in a variety of applications such as food processing, rubber vulcanization, textile and wood products, and drying of ceramic powders. Use of microwave technology in material science and processing is quite popular now. The areas where it has been applied include: process control, drying of ceramic sanitary wares, calcination, and decomposition of gaseous species by microwave plasma, powder synthesis, and sintering of oxide ceramics and some non-oxide systems [16].

**Microwave-material interactions**

Microwaves can interact with materials through several loss mechanisms. These mechanisms include electronic polarization, ionic vibration, ion jump relaxation, conduction, and interfacial polarization [17].

Electronic polarization and ionic vibration are resonance phenomena and, if operable during microwave heating, have the potential to directly change the ion jump frequency. Electronic polarization would alter the energy barrier to be overcome by the jumping ion, and ionic vibration would alter the frequency of attempted jumps. Microwave frequencies are in the range of $10^9$ to $10^{10}$ Hz, and the ion jump frequency is of the order of the Debye frequency, which is about $10^{13}$ Hz. Since electronic polarization occurs at even higher frequencies than ionic vibration, this loss mechanism is not thought to be operable at microwave frequencies either. Thus it can be concluded that electronic polarization and ionic vibration are not important loss mechanisms for microwave heating.

Ion jump relaxation in a crystalline ceramic occurs when an aliovalent ion and vacancy form an associated pair. (An aliovalent ion is an impurity cation or anion with a valence different from that of its host sublattice.) An aliovalent ion-vacancy pair has a dipole moment associated with it that responds to the applied electric field. The vacancy is thought to jump around the aliovalent ion to align its dipole moment with the electric field. Interfacial polarization occurs at a structural inhomogeneity such as a grain boundary, dislocation, or vacancy cluster. In an ionic lattice there will be a localized disruption in electroneutrality at such a structural inhomogeneity with a net dipole moment that will align itself with the applied field.

Conduction is mostly of interest at low frequencies. This type of loss mechanism occurs when vacancies are not associated with other defects, and hence are not localized. Unassociated

vacancies are much more mobile than associated pairs and migrate in response to the electric field.

**Characteristics of microwave heating**

Material dielectric properties are usually discussed in terms of the dielectric constant and the loss tangent. The dielectric constant is a measure of the ability of the material to retard microwave energy as it passes through; the tangent loss is a measure of the ability of the material to dissipate the energy. In other words, tangent loss represents the amount of input microwave energy that is lost in the material by being dissipated as heat. Thus, a material with high tangent loss is easily heated up by the microwave energy. According to their microwave properties, materials can be divided into three categories as shown in Figure 1.2 [16]. Materials with very low loss tangents allow microwaves to pass through with very little absorption and are said to be transparent to microwaves. Materials with extremely high loss tangents, i.e. metals, reflect microwaves and are said to be opaque. Materials with intermediate loss tangents will absorb microwaves.

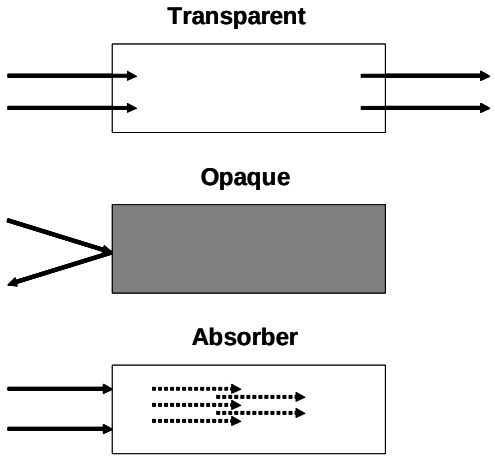


**Figure 1.2.** Interaction of microwave with materials [16]

The power dissipated in a dielectric material undergoing microwave heating is given by the following formula [17]:

$$P_A = 2\pi f \varepsilon_0 \varepsilon''_{eff} |E|^2 \quad (1)$$

$$D_p = \frac{\lambda_0}{2\pi\left(2\varepsilon'\right)^{1/2}}\left[\left(1+\left(\varepsilon''_{eff}/\varepsilon'\right)^2\right)^{1/2}-1\right]^{-1/2} \quad (2)$$

where $P_A$ is absorbed power per unit volume, $D_p$ is depth of penetration, $f$ frequency of the field, $\varepsilon_0$ permittivity of free space, $\lambda_0$ free space wavelength of the microwave radiation, $E$ mean square internal electric field, $\varepsilon'$ and $\varepsilon''_{eff}$ and are the relative values of the dielectric constant and loss factor, respectively. The internal electric field is dependent on $\varepsilon'$ and $\varepsilon''_{eff}$ as well as the field within the cavity.

One of the unique features of microwave heating is the inverted temperature profile. In contrast to conventional heating, microwave-heated materials usually exhibit higher temperatures in their interior than on the surface. The inverted profiles can be explained with Equations (1) and (2) in combination with surface emissivity. Many materials have sufficient values of $\varepsilon''_{eff}$ to allow deep penetration and deposition of microwave energy. Although energy is deposited on the surface as well as in the interior, it is also radiated from the surface. Surface radiation occurs more rapidly (especially at high temperatures) than thermal conduction can deliver heat from the interior and, consequently, the surface remains cooler. Furthermore, there are some processes that can benefit from the inverted profiles.

In many conventional methods involving resistant/radiation/convection heating, the thermal energy is absorbed on the surface of the work-piece and then it is transferred towards the inside via thermal conductivity; so there is an energy transfer through the thermal conductivity

mechanism in these methods, and therefore the process is slow. Such methods are not very energy efficient. On the other hand in case of microwave heating, the electromagnetic energy is absorbed by the material as a whole (also known as volumetric heating) due to microwave-matter coupling and deep penetration, and then is converted into heat through dielectric (in case of ceramics), magnetic permittivity/eddy currents (metals) loss mechanisms. Since there is an energy conversion and no thermal conductivity mechanism involved, the heating is very rapid, uniform and highly energy efficient. These two processes are fundamentally different in their heating mechanisms, and hence often result in a vastly different product. Figure 1.3 shows the comparison of conventional and microwave heating patterns.

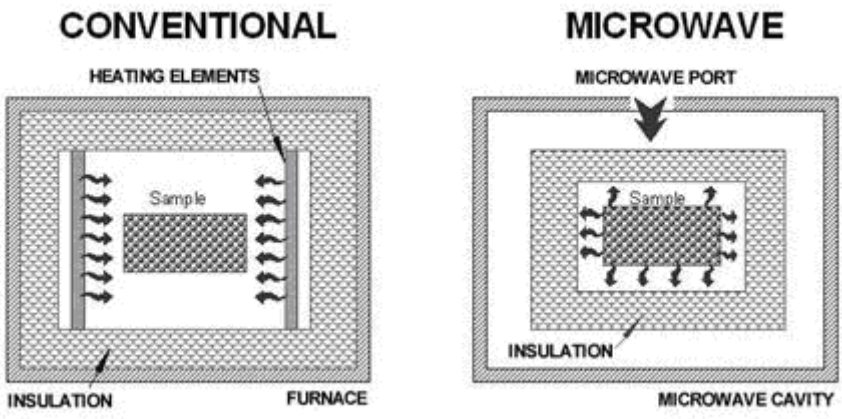


**Figure 1.3.** Comparison of conventional and microwave heating patterns [18]

**Advantages of microwave heating process**

Microwave heating is a bulk heating in which the electromagnetic field interacts with the material as a whole. The heating occurs nearly instantaneously and the speed of heating is often possible to accomplish in seconds or minutes compared with much slower conventional heating

method. Uniform heating may occur throughout the material, avoiding the large temperature gradients that happen in the conventional heating systems. In the microwave heating, the energy couples directly to the material being heated. It is not expended in heating the air, walls of the oven, conveyor or other parts. This can lead to significant energy savings and selective heating. The instantaneous on-off nature of the heating and the ability to change the degree of heating by controlling the output power of the microwave source generator means fast, efficient, and accurate control of heating. Since high surface temperatures are not usually generated, overheating of the surface and case hardening, which are common with conventional heating methods are eliminated. This often helps to improve the product quality. Many chemicals and physical reactions are also promoted by the heat generated by this method, resulting in desirable chemical and physical effects: puffing, drying, melting, protein denaturation, starch gelatinization.

## 1.3 THICKNESS SHEAR MODE (TSM) RESONATOR

### 1.3.1 Basic theory of thickness shear mode (TSM) resonator

The thickness shear mode(TSM) resonator, widely referred to as a quartz crystal microbalance(QCM), typically consists of a thin disk of AT-cut quartz with circular electrode patterned on both sides, as shown in Figure 1.4. Due to the piezoelectricity and crystalline orientation of the quartz, an applied alternating voltage between these electrodes results in a shear deformation of the crystal. The crystal can be electrically excited in a number of resonant thickness shear modes. The displacement maxima of shear waves occur at the crystal faces

(Figure 1.4, right), making the device sensitive the surface perturbations. The resonator is typically incorporated in an oscillator circuit, where the oscillation frequency tracks the crystal resonance and indicates mass accumulation on the device surface. This microbalance capability has facilitated a lot of gas and liquid sensor applications.

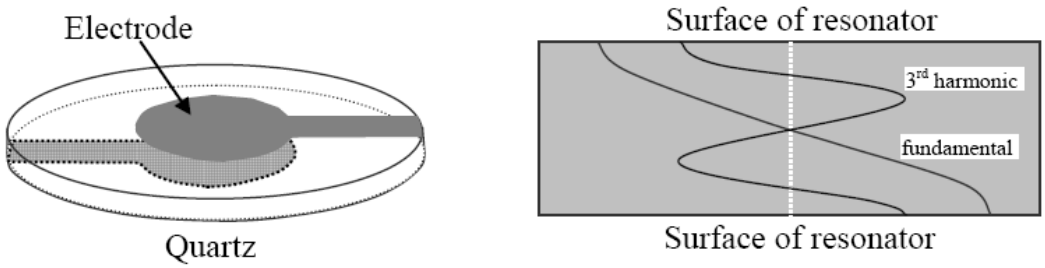


**Figure 1.4.** Schematic of a thickness shear mode quartz resonator [19]

When an alternating voltage is applied across the TSM resonator electrodes, shear wave having opposite polarities are generated at the electrodes on the two faces of the crystal resonator. The waves are generated only at the electrodes because those are the only regions in the crystal where the piezoelectric source varies spatially. The displacement $u_x$ in the crystal is a superposition of these waves [20]:

$$u_x(y,t) = \left(Ae^{jky} + Be^{-jky}\right)e^{j\omega t} \qquad (3)$$

where A and B are constants, $\omega$ is the angular excitation frequency ($\omega = 2\pi f$), k is the wave number, t is time, and $j = (-1)^{1/2}$. The resonant condition for the TSM resonator can be determined by tracing the path of one propagating shear wave, which may be thought to start at the top electrode, propagate through the thickness of the quartz thickness, reflect at the bottom surface with phase shift of $\pi$, and then return to their origin where it reflects again with phase

shift of π. The wavelength λ, the resonant frequency $f_N$, and the shear wave velocity $v_s$ for resonance are given by [20]:

$$\lambda = \frac{2h_s}{N} \tag{4}$$

$$f_N = \frac{Nv_s}{2h_s} \tag{5}$$

$$v_s = \left( \frac{u_q}{\rho_q} \right)^{1/2} \tag{6}$$

where $N$ : odd integers, $h_s$ : thickness of resonator, $\mu_q$ : shear stiffness, and $\rho_q$ : mass density of resonator.

The presence of displacement maxima at the crystal surfaces makes the thickness shear mode very sensitive to surface mass accumulation. Mass that is rigidly bound moves synchronously with the crystal surface, perturbing the TSM resonant frequency. The relation between surface mass accumulation and resonant frequency change can be derived from a simple Rayleigh criterion. The Rayleigh criterion states that resonance in a mechanical system occurs at frequencies at which the peak kinetic energy $U_k$ exactly balances the peak potential energy $U_p$ [20]. The accumulation of mass on the crystal surface causes an increase in kinetic energy without changing the potential energy. This assumes that the mass layer is sufficiently thin and rigid and the displacement is uniform across its thickness. The Rayleigh hypothesis indicates that when mass accumulates on the surface, the resonant frequency must change to rebalance kinetic and potential energies. The peak kinetic energy and the peak potential energy $U_p$ are given by:

$$U_k = \frac{\omega^2 u_{xo}^2}{2} \left( \rho_s + \frac{\rho_s h_s}{2} \right) \tag{7}$$

$$U_p = \frac{\mu_q k^2 u_{xo}^2 h_s}{4} \tag{8}$$

By balancing peak kinetic and potential energy from Equation (7) and (8), a relationship between resonant frequency $\omega$ and surface mass density $\rho_s$ is given by:

$$\left(\frac{\omega_o}{\omega}\right)^2 = 1 + \frac{2\rho_s}{h_s \rho_q} \tag{9}$$

where $\omega_0 = (N\pi / h_s)(\mu_q / \rho_q)^{1/2}$ is the unperturbed resonant frequency when $\rho_s = 0$.

For a small mass change (i.e. 2% or less), a linear approximation can be made and Equation (9) can be rewritten as:

$$\frac{\Delta f}{f_o} = -\frac{\rho_s}{h_s \rho_q} \tag{10}$$

Equation (10) indicates that a fractional shift in resonant frequency is equal to a fractional change in mass. By combining Equation (4), (5), (6) and (10), we obtain the so-called Sauerbrey equation, commonly used to relate change in TSM resonant frequency to changes in surface mass density $\rho_s$:

$$\Delta f = -\frac{2 f_1^2 \rho_s}{(\mu_q \rho_q)^{1/2}} \tag{11}$$

where $f_1$=fundamental frequency, $\rho_s$=mass/area of the sensitive layer whose mass is changing, $\rho_q$=mass/volume of resonator, $\mu_q$=shear stiffness.

The Sauerbrey equation makes the assumption of ideal mass layer (no energy lost). On a TSM resonator, a film is considered ideal if it is thin and rigid, and therefore moves synchronously with the oscillating surface. More quantitatively, the acoustic phase shift $\phi$ across the film must fulfill $\phi << \pi$, in which the phase shift can be calculated using:

$$\phi = \omega h_s \left( \frac{\rho}{G} \right)^{1/2} \tag{12}$$

where $\rho$ : film density, $G$ : shear modulus, $h_s$ : thickness.

Furthermore, a quality factor $Q$ can be defined:

$$Q = \frac{f_0}{\Delta f} \tag{13}$$

where $f_o$ is the resonant frequency and $\Delta f$ is the width at half-height. $Q$ represents the resonant stability of the resonator and affects the resolution at which the resonant frequency can be measured. Hence, for high resolution mass detection, a high $Q$ is necessary.

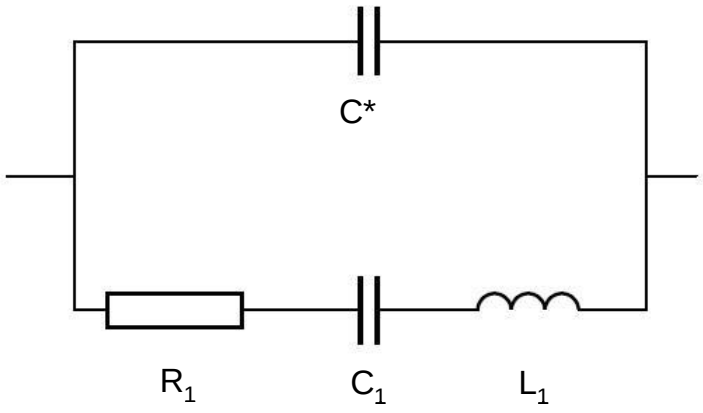


**Figure 1.5.** Butterworth-van-Dyke (BVD) equivalent circuit of unperturbed TSM resonator near the series resonant frequency

The acoustic device uses a piezoelectric substrate material in which the electric field generated between electrodes couples to mechanical displacement. This allows electrical excitation and detection of mechanical resonances. In order to establish the relationship between the measured electrical response and the mechanical properties, the resonant system can be approximated by an equivalent circuit model know as Butterworth-van Dyke (BVD) circuit [21]

as shown in Figure 1.5. In the BVD circuits, we use $C^*$ representing the parasitic capacitance. For the resonators as practical sensors, the parasitic capacitance not only includes the static capacitance $C_0$ , but also includes a capacitance $C_p$ that arises in the test fixture. $R_1$ , $C_1$ and $L_1$ give the motional contributions due to the electromechanical coupling of the piezoelectric material. The static capacitance dominates the electrical behavior far from resonance and the motional contribution dominates near the resonance. The model provides simulation of the TSM resonator electrical characteristic near the resonant frequency. The elements of the circuit correspond to physical properties of the resonator as listed below:

$$C_0 = \frac{\varepsilon_{22} A}{h_s} \tag{14}$$

$$C_1 = \frac{8K^2 C_0}{(N\pi)^2} \tag{15}$$

$$L_1 = \frac{1}{\omega_s^2 C_1} \tag{16}$$

$$R_1 = \frac{\eta_q}{\mu_q C_1} \tag{17}$$

where,

$\eta_q$ : effective viscosity

$\mu_q$ : shear stiffness

$k^2$ : electromechanical coupling coefficient

$\rho_q$ : mass density

$\omega_s$ : angular series resonant frequency (unperturbed)

$\varepsilon_{22}$ : dielectric permittivity

$A$ : electrode area

$h_s$ : resonator thickness

The total TSM resonator admittance can be determined from inspection of the BVD circuit model [20]:

$$Y(\omega) = j\omega C^* + \frac{1}{Z_m} \tag{18}$$

where the motional impedance for the unperturbed resonator is

$$Z_m = R_1 + j\omega L_1 + \frac{1}{j\omega C_1} \tag{19}$$

In addition, two different resonance frequencies are defined. The series resonant frequency $f_s$ is defined as the frequency at which the motional reactance is zero.

$$f_s = \frac{1}{2\pi (L_1 C_1)^{1/2}} \tag{20}$$

The parallel resonance frequency $f_p$ is defined as the frequency at which the total reactance (motional plus static admittances) is zero.

$$f_p = \frac{1}{2\pi}\left[\frac{1}{L_1}\left(\frac{1}{C_1} + \frac{1}{C^*}\right)\right]^{1/2} \tag{21}$$

When the resonator has a surface perturbation, the motional impedance increases which is represented by the equivalent circuit model in Figure 1.6. The additional motional impedance $Z_e$ is given by:

$$Z_e = \frac{N\pi}{4K^2\omega_s C_0}\left(\frac{Z_s}{Z_q}\right) \tag{22}$$

where $Z_q = \left(\rho_q \mu_q\right)^{1/2}$ is the quartz shear wave characteristic impedance and $Z_s = \frac{T_{xy}}{v_x}\Big|_{y=0}$, is the shear mechanical impedance at the device surface, $T_{xy}$ is shear stress (force per area in the x-direction on a y-normal plane), $v_x$ is surface shear particle velocity in the x-direction.

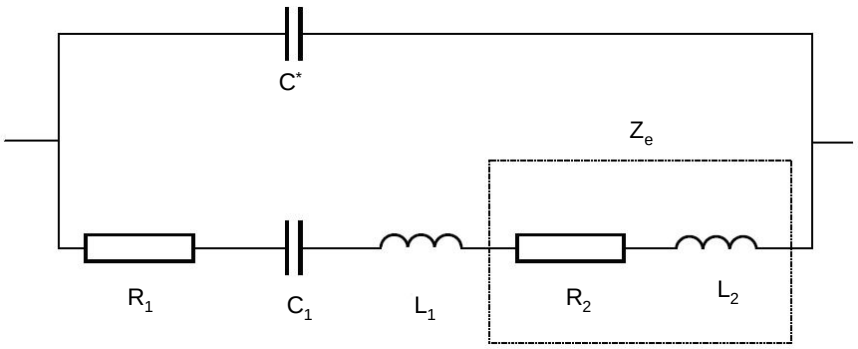


**Figure 1.6.** Lumped element equivalent circuit model for the perturbed resonator

Let $Z_e = R_2 + j\omega L_2$, the motional impedance elements $L_2$ and $R_2$ are related to the mechanical impedance contributed by the surface perturbation and can be defined as:

$$R_m = \frac{N\pi}{4K^2\omega_s C_0}\left(\frac{\mathrm{Im}(Z_s)}{Z_q}\right) \tag{23}$$

$$L_m = \frac{N\pi}{4K^2\omega_s C_0}\left(\frac{\mathrm{Im}(Z_s)}{Z_q}\right) \tag{24}$$

The motional impedance is now given by:

$$Z_m = \left(R_1 + R_2\right) + j\omega\left(L_1 + L_2\right) + \frac{1}{j\omega C_1} \tag{25}$$

Since the series resonant frequency is defined as the point where motional inductance and capacitance resonate, the motional inductance $L_2$ causes a shift in series resonant frequency (relative to the unperturbed case) given by:

$$\Delta f_s = -\frac{L_2 f_s}{2(L_1 + L_2)} \approx -\frac{L_2 f_s}{2L_1} \tag{26}$$

For an ideal mass layer, the surface mechanical impedance associated with the mass layer is:

$$Z_s^{masslayer} = \frac{T_{xy}}{v_x}\Big|_{y=0} = j\omega\rho_s \tag{27}$$

Combining Equation (22) and (27) gives the additional motional impedance element $L_2$ and $R_2$:

$$L_2 = \frac{2\omega_s L_1 \rho_s}{N\pi\sqrt{\mu_q \rho_q}} = \frac{N\pi\rho_s}{4K^2\omega_s C_0\sqrt{\mu_q \rho_q}} \tag{28}$$

$$R_2 = 0 \tag{29}$$

The shift in series resonant frequency could be obtained by substituting Equation (28) into Equation (26), giving the Sauerbrey Equation, similar to that obtained from a mechanical derivation Equation (9):

$$\Delta f_s \approx -\frac{L_2 f_s}{2L_1} = -\frac{2 f_s^2 \rho_s}{N(\mu_q \rho_q)^{1/2}} \tag{30}$$

### 1.3.2 Thickness shear mode resonator sensors for chemical sensing

Utilizing the resonator as a chemical sensor is a matter of selecting a suitable film which responds to the target chemical species. The sensitive layer, which is chemically or physically bound to the sensor surface, acts as a chemically sensitive and selective element that immobilizes a finite mass of some chemical species from the environment. Resultant changes in physical and /or chemical properties of the sensitive layer, in turn, perturb the underlying acoustic wave device. Perturbations of acoustic wave resulting from the interaction of the coated layer with one or more analytes constitute the basis for detection and quantitation. Typically, such a response is

a change in mass, which can be accurately measured by the resonator. The mass sensitivity of a resonator is defined as [22]:

$$S_f = 2f^2/(\rho_q v) \tag{31}$$

where $f$ : resonant frequency, $\rho_q$ : density of resonator, and $v$ : velocity of shear wave. Note that percentage mass change must be less than 2% for Equation (31) to be valid. To maximize mass sensitivity, the most obvious way is to increase the resonant frequency of the resonator. In the case of TSM acoustic resonators, this could be done by reducing the resonator thickness in term of Equation (5). However, this also increases its response to other perturbations. Hence, the more acceptable approach is to increase the sensitivity of the active film towards the target chemicals.

As we know, the interactions of the sensitive layer towards the target chemicals can be organized into two broad categories; physical and chemical. These two interactions involving adsorption are referred to as physisorption and chemisorption, respectively. Physisorption often has little or no energetic activation barrier, and involves relatively weak, long range van der Waals interactions. As a result, physisorption is typically quite reversible at room temperature, but relatively nonselective. Chemisorption involves greater redistribution of electron density and the formation of a chemical bond. In addition, the chemical bonds of the sorbing species may be broken as new bonds are formed via reaction with the coated layer, causing the adsorbate to lose its original identity. More often than physical interactions, chemical processes are activated, meaning that a finite energetic barrier must be overcome for adsorption to occur.

When all other properties are equal, it is found that the interactions between the sensitive layer and the target chemicals are significantly affected by the reactive area of the coating. Therefore, it is clear that a film having higher surface area results in a larger number of analyte molecules being adsorbed for a given ambient-phase analyte concentration, the consequences of

which are enhanced sensitivity and limit of detection. For reactive and adsorptive coatings, higher surface area translates to higher capacity and thus greater dynamic range. For traditional high surface area solid adsorbents suitable for sensor coating are granular microporous materials such as activated charcoal, silica gel, alumina gel, porous polymers, and molecular sieves. For most such materials, high adsorption capability arises from the presence of large numbers of micropors.

## 1.4 MICROFABRICATION BACKGROUND

Micro-fabrication or micromachining are the techniques for fabricating of miniature structures, at micron or smaller scales. It was originally used for semiconductor devices in integrated circuit fabrication. Now they are extended to be used for the fabrication of sensors, microreactors, microelectromehcanical systems (MEMS), microanalytical systems and micro-optical systems. The basic techniques include deposition of thin film, patterning, and etching.

Deposition is that thin film materials are deposited or grown on the substrates which usually are the silicon wafers. Deposition processes range from simple spin-on methods, where a material in liquid form is deposited on wafer and the wafer is spun at high speeds to evenly spread a thin film of material across the substrate, to more complex physical and chemical methods that utilize complex chemical reactions and physical phenomena to deposit films. Two general methods exist for deposition of thin films: physical vapor deposition (PVD) and chemical vapor deposition (CVD). Each deposition method has intrinsic advantages and limitations in terms of the quality, type and range of material that can be deposited, as well as concerns related to equipment, cost and complexity.

In this study, sputtering is the method we used to deposit the electrodes. Sputtering is also the PVD method most preferred in industrial fields. The objective of this deposition process is to controllably transfer atoms from a source (solid target) to a substrate where film formation and growth proceed atomistically. The target material can be almost any solid (alloys or compounds, both insulating and conducting) thus making the sputtering technique widely used [23]. In this process, the gaseous plasma discharges are used to bombard the surface materials off of a target which is made of the material to be deposited. Atoms are then displaced (sputtered) and carried to the substrate by a potential difference between the target and the substrate (the target serves as the cathode, while the substrate wafer acts as the anode). The plasma is a partially ionized gas containing a great deal of energy. Heavy inert gases (usually argon ions) are used to provide the energetic ions which are discharged onto the target. This discharge results from a current flowing through the low pressure gas (medium or high vacuum), and some of the discharges can glow due to light emission from excited atoms. The discharge particles can be either neutral or ionic. However, ions are preferred since they can be controlled by an electric field. In the deposition process, more than one target can be used and deposition can be made at the same time on all targets, or in a predetermined order.

In the sputtering process, any material can be deposited stoichiometrically, and a uniform film deposition rate can be obtained over large areas. As well, the kinetic energy distribution of sputtered atoms is close to the energy needed for the displacement of surface atoms, therefore there is no extra leftover energy, which could damage the deposited surface. Due to these properties, the sputtering is the most widespread using method of PVD techniques.

Sputtering can be divided into four categories: (1) direct current (DC), (2) radio frequency (RF), (3) magnetron, (4) reactive. There are important variants within each category

(e.g., DC bias) and even hybrids between categories. In DC sputtering a high voltage DC source (in the range of kilovolts) is used to create and sustain the plasma, with the sputtering target being the cathode of the discharge, and with the substrate (and vacuum chamber walls) acting as the anode. Argon is the most commonly used sputtering gas. DC sputtering requires the use of only conductive targets. This is due to the nature of the target cathode which accumulates charge, and would not allow for the flow of charge if it were non-conducting. In order to overcome this, Radio frequency voltage can be used to create a capacitive environment around a non-conducting target in order to create a discharge. Radio frequency sputtering was invented as a means of depositing insulating thin films. Below about 50 kHz, ions are sufficiently mobile to establish a complete discharge at each electrode on each half-cycle. Direct current sputtering conditions essentially prevail at both electrodes, which alternately behave as cathodes and anodes. Above 50 kHz two important effects occur. Electrons oscillating in the glow region acquire enough energy to cause ionizing collisions, reducing the need for secondary electrons to sustain the discharge. Secondly, RF voltages can be coupled through any kind of impedance so that the electrodes need not be conductors. This makes it possible to sputter any material irrespective of its resistivity. Typical RF frequencies employed can range from 5 to 30 MHz. However, 13.56 MHz has been reserved for plasma processing by the Federal Communications Commission and is widely used. RF sputtering essentially works because the target self-biases to a negative potential. Once this happens, it behaves like a DC target where positive ions bombardment sputters away atoms for subsequent deposition. Negative target bias is a consequence of the fact that electrons are considerably more mobile than ions and have little difficulty in following the periodic change in the electric field.

Though DC/RF sputtering is the most popular technique due to its simplicity, it is not efficient. And thin film might be damaged due to the increase in temperature which can be caused by the energetic electrons bombarding the surface of the substrate. Another technique magnetron sputtering will enhance the sputtering performance. For the magnetron sputtering technique, bar or horseshoe magnets are places behind the target. Therefore, the magnetic field lines first emanate normal to the target, then bend with a component parallel to the target surface and finally return, completing the magnetic circuit. Electrons emitted from the cathode are initially accelerated toward the anode, executing a helical motion in the process. When they encounter the region of the parallel magnetic field, they are bent in an orbit back to the target. Electrons stay in the negative glow region with a circular motion before collisions may drive them back toward anode. By suitable design of target magnets, a "race track" will be produced where the electrons hop around at high speed. Because of the intense ionized gas above the "race rack", target erosion by sputtering occurs within it. In our study, a magnetron sputtering system ATC1300 (AJA International, North Scituate, MA) was used to deposited electrode on the sample.

Patterning techniques are used to create features on the micrometer or nanometer scales in the thin film layers. The most powerful of patterning techniques is the photolithographic (also optical lithography) process. It uses light to transfer a geometric pattern through a photomask to a light-sensitive chemical (photoresist) on the substrate. Photolithography involves three primary steps; deposition of a photosensitive emulsion layer (termed photoresist, or simply resist), ultraviolet exposure of the wafer and resist to some pattern, and subsequent develop of the wafer to remove unwanted photoresist and then get the exposed pattern. A resist is applied to the surface using a spin-coating machine. This device holds the wafer of semiconductor, using a

vacuum, and spins it at high-speed (3000-6000 rpm) for a period of 15-30 seconds. A small quantity resist is dispensed in the centre of the spinning wafer. The rotation causes the resist to be spread across the surface of the wafer with excess being thrown spun off. Close to the centre of the wafer, the variation in the thickness of resist is around 30 nm. Preparation of the resist is concluded by a pre-bake, where the wafer is a gently heated in a convection oven and then a hotplate to evaporate the resist solvent and to partially solidify the resist. The photomask is created by a photographic process and developed onto a glass substrate. The cheapest masks use ordinary photographic emulsion on soda lime glass, while Chrome on quartz glass is used for the high-resolution deep UV lithography. Alignment of the mask is critical and must be achieved in for x-y as well as rotationally. Industrial photolithography machines use automatic pattern recognition to achieve the registration alignment. Depending on the design of the photolithography machine, the mask may be in contact with the surface, very close to the surface or used to project the mask onto the surface of the substrate. During the exposure process, the resist undergoes a chemical reaction. Depending on the chemical composition of resist, it can react in two ways when the light strikes the surface. The action of light on a positive resist causes it to become polymerized where it has been exposed to the light. A negative resist has the reverse property. Exposure to UV-light causes the resist to decompose. After the developing process, a negative of the mask remains as a pattern of resist. Although not necessary for all processing, to further harden and remove any residue of the developer, the wafer undergoes a post-bake process. Figure 1.7 shows the basic steps of the photolithographic process.

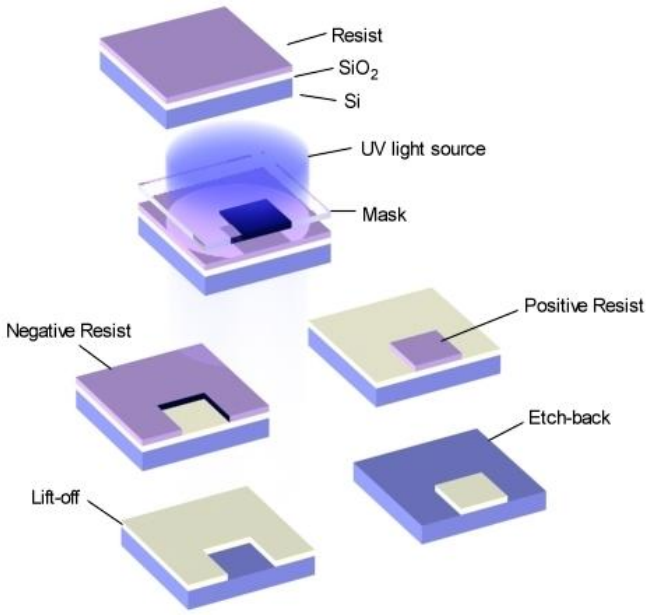


**Figure 1.7.** Basic photolithography process

The final step involves the removal, or etching, of materials in desired areas by physical or chemical means to create the microstructure. The patterned photoresist serves as a material template for the definition of microstructures. Patterns can be etched directly into the silicon substrate, or into a thin film which in turn can be used as a mask for subsequent etches. Many etching forms including wet-chemical, dry-chemical, and physical etching techniques are all used in MEMS processing.

In our study, we use wet etch process to achieve the final electrode pattern. Wet etching involves using solutions with diluted chemicals to dissolve the unprotected areas of a thin film or substrate. There are numerous wet etchants used, depending on the material to be removed. Wet etching can either be isotropic etching or anisotropic etching depending on the structure of the materials or the etchants used. For bulk micromachining, both isotropic and anisotropic etchants exist. If the material is amorphous or polycrystalline, wet etching is always isotropic etching. Each etchant removes material at a specific rate at a certain temperature, and thus the etch time

varies as a function of material and thickness. The chemical reaction that occurs varies from etchant to etchant as well. Wet etching is easy to apply, and it needs inexpensive equipment and facility.

## 1.5 POLYMER-MATRIX NANOCOMPOSITES AND ALIGNMENT TECHNIQUES

### 1.5.1 Polymeric nanocomposites

Polymer composites are manufactured commercially for many diverse applications such as sporting goods, aerospace components, automobiles, etc. In the last 20 years, there has been a strong emphasis on the development of polymeric nanocomposites, where novel properties have been attained by successfully imparting the nanoscale filler materials into the polymer matrix. Nanoscale materials have a large surface area for a given volume [24]. Since many important chemical and physical interactions are governed by surfaces and surface properties, a nanostructured material can have substantially different properties from a bulk material of the same composition. Typical nanomaterials currently under investigation include nanoparticles, nanotubes, nanofibers, fullerenes, and nanowires. In general, these materials are classified by their geometries into three classes: particle, layered, and fibrous materials [25, 26]. Carbon black, silica nanoparticle, polyhedral oligomeric sislesquioxanes (POSS) can be classified as nanoparticle reinforcing agents while nanofibers and carbon nanotubes are examples of fibrous materials [26]. When the filler has a nanometer thickness and a high aspect ratio (30–1000) plate-like structure, it is classified as a layered nanomaterial (such as an organosilicate) [27].

In general, nanomaterials provide reinforcing efficiency because of their high aspect ratios [24]. The properties of a nanocomposite are greatly influenced by the size scale of its component phases and the degree of mixing between the two phases. Depending on the nature of the components used (layered silicate or nanofiber, cation exchange capacity, and polymer matrix) and the method of preparation, significant differences in composite properties may be obtained [28]. For example, Figure 1.8 represents three main types of composites for layered silicate materials [29]. When the polymer is unable to intercalate (or penetrate) between the silicate sheets, a phase-separated composite is obtained, and the properties stay in the same range as those for traditional microcomposites. In an intercalated structure, where a single extended polymer chain can penetrate between the silicate layers, a well-ordered multilayer morphology results with alternating polymeric and inorganic layers. When the silicate layers are completely and uniformly dispersed in a continuous polymer matrix, an exfoliated or delaminated structure is obtained. In each case, the physical properties of the resultant composite are significantly different.

Analogously, in fibrous or particle-reinforced polymer nanocomposites (PNCs), dispersion of the nanoparticle and adhesion at the particle–matrix interface play crucial roles in determining the mechanical properties of the nanocomposite. Without proper dispersion, the nanomaterial will not offer improved mechanical properties over that of conventional composites, in fact, a poorly dispersed nanomaterial may degrade the mechanical properties [29]. Additionally, optimizing the interfacial bond between the particle and the matrix, one can tailor the properties of the overall composite, similar to what is done in macrocomposites. For example, good adhesion at the interface will improve properties such as interlaminar shear strength, delamination resistance, fatigue, and corrosion resistance.

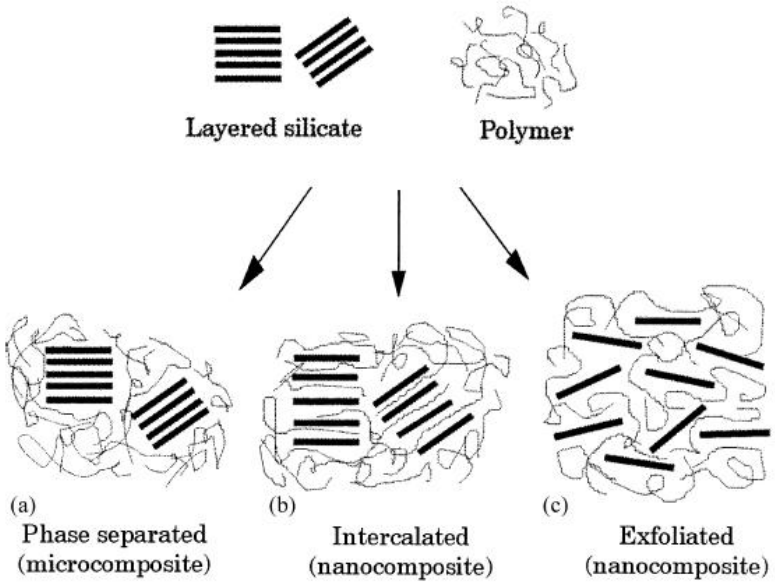


**Figure 1.8.** Scheme of three main types of layered silicates in polymer matrix [29]

### 1.5.2 Alignment techniques

Mechanical properties of nanocomposites such as stiffness and strength, and functional properties such as electrical, magnetic and optical properties, are linked directly to the alignment of the nanotubes/nanofibers [30]. However, due to the nanoscale dimensions of nanomaterials, achieving desired tube and nanofiber alignment is a major challenge for developing high-performance nanotube and nanofiber-reinforced nanocomposites [31]. Therefore, to align nanotubes and nanofibers in selected locations and directions in a controlled way has been a long-standing issue [32]. Techniques to overcome this issue are studied through the following different techniques: magnetic field-induced alignment [33], electric field assisted alignment [34], surface chemistry method [35] and shear force method [36].

**Magnetic field induced alignment**

Kimura et al. first discovered that mechanically anisotropic composites could be obtained through the use of a high magnetic field to align nanotubes in a polyester matrix. The monomer solution of unsaturated polyester is mixed with MWNTs and subjected to a constant magnetic field of 10T. Polymerizing this MWNT-monomer dispersion under the magnetic field freezes the alignment of MWNTs in the polyester matrix. The setup for the preparation of nanotube-polymer composites inside a magnet is illustrated in Figure 1.9 [33].

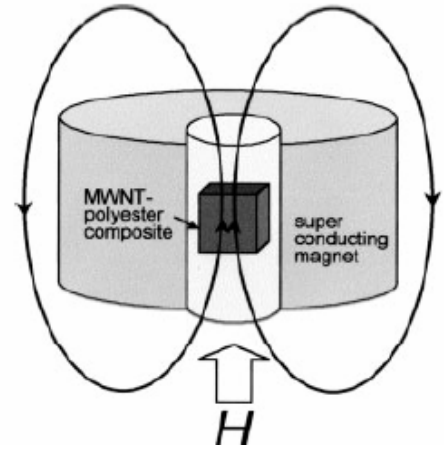


**Figure 1.9.** Setup for the preparation of MWNT-polymer composites inside a magnet [33]

**Electric field assisted alignment**

Due to the highly anisotropic polarisability of nanotubes, nanotube alignment can be achieved by using electric fields to direct nanotubes dispersion in the polymer matrix. Figure 1.10 shows a schematic of the alignment and photopolymerization apparatus [34]. In this process, SWNTs were aligned via AC field-induced dipolar interactions among the nanotubes in a liquid matrix followed by immobilization by photopolymerization under continued application of the electric

field. Alignment of SWNTs was controlled as a function of magnitude, frequency, and application time of the applied electric field.

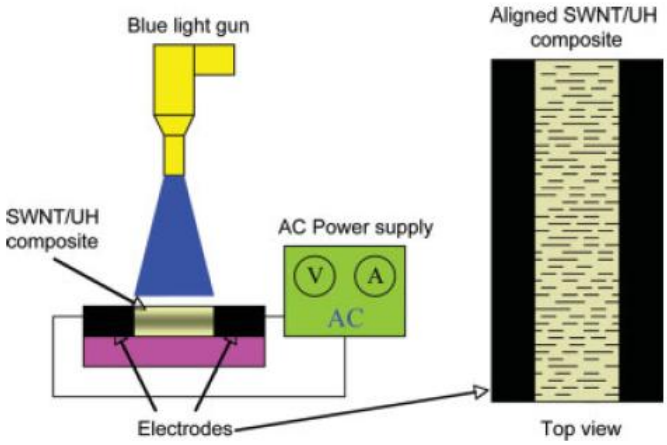


**Figure 1.10.** Experimental setup of photopolymerization of SWNT/UH composite under an electric field [34]

### Surface Chemistry Method

A surface chemistry method is a new technology which enables reliable deposition of individual SWNTs on chemically-functionalized nanolithographic patterns [35]. Coulombic attraction between the positively charged-$NH_2$ groups on the surface with the negatively charged SWNT suspension may exist. Therefore, nanotubes will bend in order to align well with the functionalized patterns, showing that the interaction of nanotubes with $NH_2$ groups on the surface is quite strong.

### Shear Force

The melt mixing method followed by spinning and extruding was proposed to result in the alignment of nanotubes in nanocomposites as well [36]. Fibers of CNTs and nanofibers spun or

extruded from super-acid suspensions exhibit preferred orientation along their axes. Usually, nanotubes and polymer were first mixed by screw and followed by extrusion to result in a certain degree of tube alignment in nanocomposites.

## 2.0 RESEARCH OBJECTIVE

The objective of this research is to fabricate ZnO micro and nanostructures using microwave thermal evaporation-deposition approach and to explore applications of ZnO nanostructures in gas sensing and multifunctional nanocomposite.

Today many synthesis techniques have been developed to fabricate one-dimensional ZnO micro/nanostructures in forms of nanowires, nanobelts, micro/nanotubes, and nanocones. However, the controlled on-chip growth still remains a challenge that inhibits the exploration of ZnO nanostructures for potential applications. Especially, fundamental issues related to the processing-structure-property relationship have not been studied in details. Another limitation is the high production cost due to the complex equipment, long processing time and low growth rate. In this study, a novel thermal evaporation-deposition approach using microwave energy will be investigated for the batch fabrication of ZnO micro and nanostructures. We also try to evaluate various processing conditions and characterize the grown ZnO micro and nanostructures.

The langasite (LGS) crystal has become a promising candidate for acoustic devices due to its superior characteristics at high temperature compared with quartz. Gas sensors using novel nanostructured materials as the active layer have demonstrated great promise as they have faster response and higher sensitivity than planar sensor configurations, due to their dramatically increased sensing surface area and strong binding properties. Therefore, it is believed that the combination of ZnO nanostructure with high temperature acoustic wave resonator such as

langasite thickness shear mode (TSM) resonators will provide an ideal gas sensor platform for both higher sensitivity and enhanced response speed. In this research, we are focusing on fabricating the langasite resonator high temperature gas sensor using ZnO nanowire array as the sensitive layer. $NO_2$ and $NH_3$ as target gases will be used to investigate the sensing performance at elevated temperature conditions.

Polymer-based nanocomposites are becoming an attractive set of organic-inorganic materials due to their multifunction and many potential applications. One of our objectives is to combine ZnO nanowires with polyimide polymer matrix to develop a novel polymeric nanocomposite for multifunctional applications that require self-sensing and self-actuation capabilities. We propose to design ZnO nanowires-polymer composites in which ZnO nanowires in the polymer matrix is micro-tailored by itself or external electric field. The goal is to achieve controlled alignment and dispersion of ZnO nanowires in the polyimide matrix, resulting in a composite that combines electrostrictive and piezoelectric properties of ZnO nanowires with the polyimide polymer matrix.

# 3.0 FABRICATION AND CHARACTERIZATION OF ZINC OXIDE MICRO AND NANOSTRUCTURES

## 3.1 INTRODUCTION

Over the past few years, considerable effort has been placed on the fabrication of nanostructures, and semiconductor materials have become the focal research point because of an increasing need in the industry. As a versatile semiconductor, ZnO has been attracting much attention recently for the potential applications in UV lighting-emitting devices [37], gas sensor [38], solar cell [39], and field emitter [40]. To date, various one-dimensional ZnO micro/nanostructures have been realized in forms of nanowires [37], nanobelts [41], micro/nanotubes [42,43], and nanocones [44]. A few processing methods for obtaining ZnO nanostructures have been developed. Although the fabrication of ZnO nanostructures has been demonstrated in the above studies, the controlled on-chip growth still remains a challenge that inhibits the exploration of the one-dimensional ZnO nano-structures for potential applications. Especially, fundamental issues related to the processing-structure-property relationships have not been studied in details. It has been realized that the electromechanical properties and the scaling effect of the one-dimensional ZnO nano-structures are very important issues that need to be particularly addressed, since a better understanding of the growth mechanisms under various processing conditions and the processing-structure-property relationships will open great

technology opportunities for controlled on-chip fabrication of ZnO nanostructures for nano-electromechanical applications. Another limitation is the high production cost due to the complex equipment, long processing time and low growth rate. There is still an underlying question of how to scale up nanoscale production using these approaches.

Currently, the microwave energy has been used to large scale synthesize multi-walled carbon nanotubes [45]. Therefore, a novel microwave thermal vapor deposition method was investigated to fabricate zinc oxide micro-and nano-structures. Microwave heating is a relatively new technique for materials processing which is fundamentally different from conventional heating methods. In the conventional heating process, the heat generated by external heating elements is transferred to the materials via radiation, conduction or convection. In this case, the temperature on the surface is always higher than that in the internal area of the sample. In the microwave process, the heat is generated internally within the material instead of originating from external heating sources, so an inverted temperature gradient is produced during the microwave heating process. The surface of the sample is cooler than the interior due to the thermal losses. Another advantage of microwave processing is the microwave electromagnetic fields can greatly enhance the reaction/diffusion and increase the crystal growth rate during processing of various materials. Moreover, both zinc source and substrates have high thermal run away properties when subjected to microwave energy. Thus, due to this fast heating and cooling character, the microwave evaporation-condensation process can save much energy and time, further reduces the cost of the final product.

The microwave system used to synthesize the ZnO micro and nanostructures are shown in Figure 3.1. It consists of a microwave generator, a circulator, a T-H tuner, and a cavity, etc. The microwave power can be adjusted from 0 to 3000 W at a frequency of 2.45 GHz. The

function of the circulator is to prevent power being reflected by the load, thus avoiding overheating of the magnetron. The forward and reflected powers are monitored by a power meter that is helpful in determining impedance matching. The T-H tuner is an additional device used to optimize impedance matching. When those stubs are adjusted properly, the tuner becomes a matching network that maximizes the power transmitted to the load by matching the source impedance to that of the load. As an important part of the cavity, sliding short is used to adjust the length of the cavity such that it can resonate at 2.45GHz. High field intensity can be attained when the cavity resonates. A quartz tube, which is used as the reaction chamber, passes through the cavity. Reaction gases are introduced at one end of the quartz tube and exhausted at the other end. The flow rates are controlled by the set of the mass flow controller.

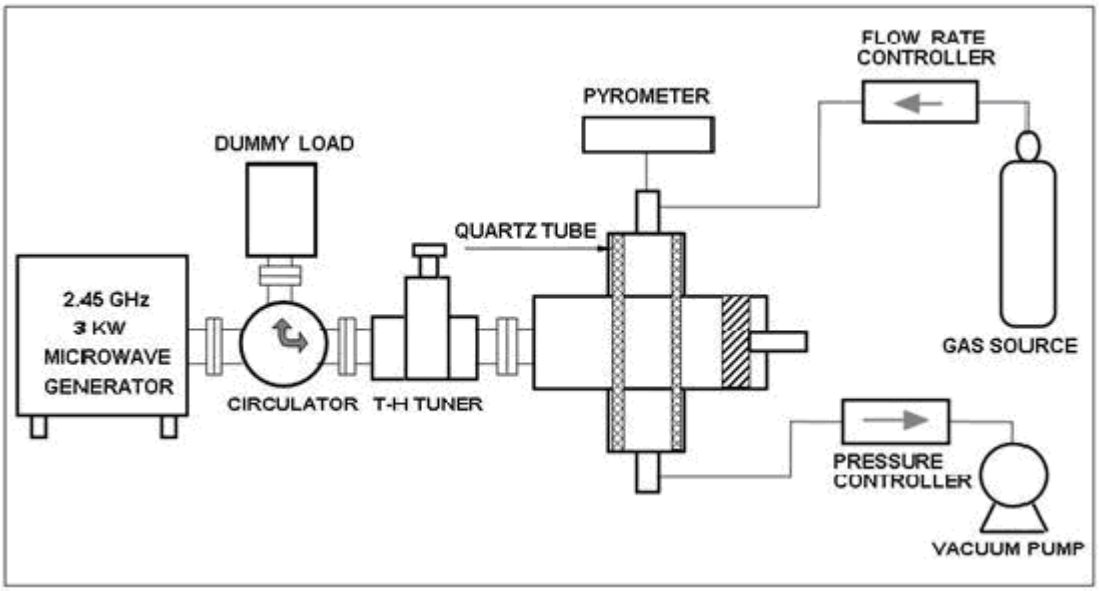


**Figure 3.1.** Schematic of the microwave system

## 3.2 SYNTHESIS OF ZINC OXIDE WITHOUT SUBSTRATES

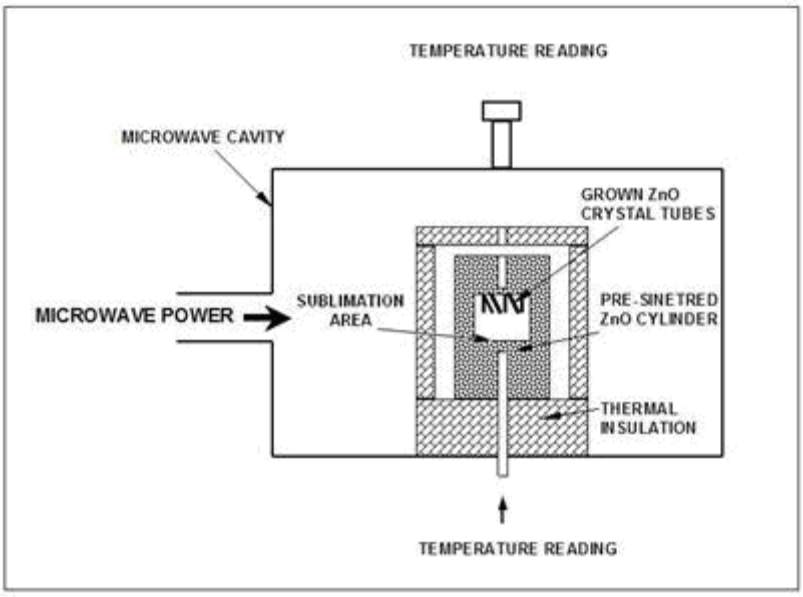


**Figure 3.2.** Schematic of the microwave growth of ZnO single crystal tubes without substrates

A schematic of the microwave growth of ZnO single crystal micro and nanotubes is shown in Figure 3.2. A pre-sintered ZnO cylinder with a hollow core of diameter 7 mm, which forms a self-encapsulated growth chamber, was positioned in the microwave cavity, surrounded with thermal insulation materials that are transparent (or with low absorption) to the microwaves to maintain the surface of the ZnO cylinder at a desired temperature. Because the heat was generated directly within the ZnO cylinder during microwave heating, the center area of the cylinder had a much higher temperature than the surface area due to the thermal losses around the surface. By adjusting the dimensions of the ZnO cylinder and the insulation conditions, a desired temperature profile could be produced. ZnO has a high melting point of 1975 °C, and sublimes or thermally decomposes rapidly at temperatures above 1400 °C. When zinc oxide was heated up to 1300°C by the microwave energy, the zinc oxide on the bottom surface of the

cylinder chamber quickly sublimated to provide Zn and oxygen vapor, while ZnO crystal tubes were nucleated and grown in the lower temperature zone on the top surface of the chamber. By varying the dimension (the distance between the sublimation and deposition area) of the hollow core and thus the microwave energy distributions inside the microwave cavity, the temperature difference between these two areas can be adjusted for high rate and high quality growth of crystal micro and nanotubes. The self-contained vapor phase growth is a unique feature of the encapsulated microwave-heating process and is critical for the growth of high quality ZnO single crystals as it can avoid considerable contaminations in grown ZnO crystals and the failure of the growth apparatus, which often happens to conventional-heating methods. Based on the synthesis process and experimental findings, the growth mechanism may be proposed as vapor-solid and self-catalyzed model. At the high temperature area, ZnO is vaporized to generate Zn and oxygen vapor. Then, these vapors are transported to the lower temperature zone to form a very thin ZnO film to act as a nucleation layer. Hence, after an initial period of nucleation and incubation, ZnO one dimensional structures continue to grow along the preferential direction [001] after vaporized the zinc source nucleates directly on the ZnO thin film. As a result, we can get different one dimensional ZnO micro and nanostructures. It was found that the tubular structure became predominant when the temperature exceeded 1300 °C. But the real reason and growth mechanism is still under investigation now.

Scanning electron microscopy (SEM) was used to characterize the structure of ZnO single crystal micro-and nanotubes. SEM is a kind microscopy used to examine physical features with dimensions from several microns down to a few nanometers. A focused beam of electrons passing through a vacuum is scanned and bombarded across the surface of the specimen and electrons emitted from the sample surface are used to form an image on a monitor screen. A

range of emissions from the specimen occurs, including backscattered (or primary reflected) electrons, secondary electrons and X-rays, and all can be utilized to obtain topographical and elemental information. Because the amount of energy given to the secondary electrons of the sample as a result of the bombarded is small, only those secondary electrons that are produced within a very short distance to the surface are able to escape from the sample. Thus the secondary electrons topographical images have very high resolution down to several nanometers. Routinely, a detector close to the specimen surface collects secondary electrons. Each captured electron causes a flash of light in a scintillator, which passes down a light guide to a photomultiplier, and this converts it to an electrical signal. The final signal is proportional to the number of secondary electrons emitted from the specimen and is used to modulate the brightness of a display spot on the monitor screen. The orientation or morphology of surface features influences the number of secondary electrons reach the detector, which creates variations in image contrast that represent the sample's surface topography.

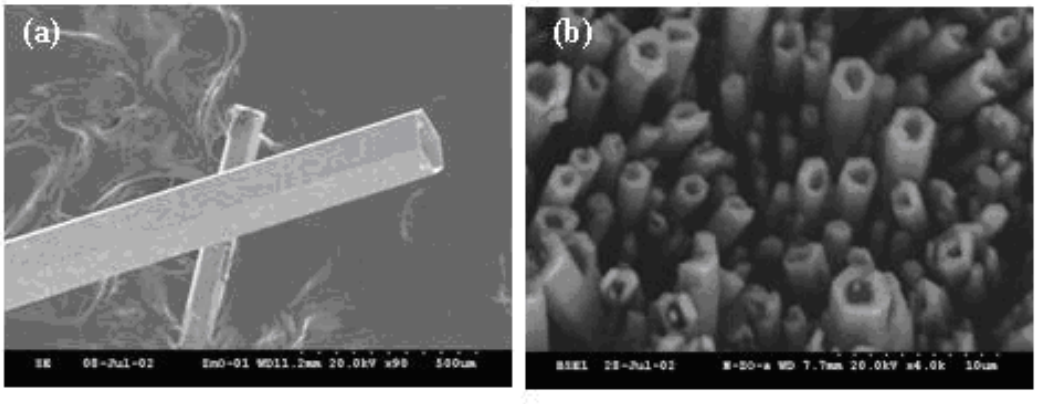


**Figure 3.3.** Single crystal ZnO (a) microtubes (b) nanotubes

Figure 3.3 shows a typical scanning electron microscopy (SEM) image of microwave-grown ZnO microtubes and nanotubes. These as-prepared products are colorless, fully transparent, contamination-free, and of near-perfect crystallinity, which can be handled with tweezers under a stereomicroscope allowing electroding and assembly for property characterizations. The ZnO crystals are grown in a hexagonal hollow tubular with a well faceted end and side surfaces. By adjusting microwave growth conditions, such as the temperature and time, the cross-sectional dimension of the ZnO micro/nanotubes can be up 150 μm, the wall thickness is about 0.3– 1 μm, and length up to 2 to 4 mm.

X-ray Deffraction (XRD) is a powerful, non-destructive analytical method for examine the chemical composition and crystallographic structure properties of materials, such as crystal structure and orientation, lattice parameters, film texture, etc. This is achieved by using the method in various of modes. A crystal lattice is a regular three-dimensional distribution (cubic, rhombic, etc.) of atoms in space. These are arranged so that they form a series of parallel planes separated from one to another by a distance d, which varies according to the nature of the material. For any crystal, planes exist in a number of different orientations that each with its own specific d spacing. When a monochromatic X-ray beam with wavelength $\lambda$ is projected onto a crystalline material at an angle $\theta$, diffraction occurs only when the distance traveled by the rays reflected from successive planes differs by a complete number n of wavelengths. By varying the angle theta, the Bragg's Law conditions are satisfied by different d-spacings in polycrystalline materials. Plotting the angular positions and intensities of the resultant diffracted peaks of radiation produces a pattern, which is characteristic of the sample. In this research, the XRD was used to determine the ZnO crystal orientation. The Laue x-ray back reflection patterns revealed

that the ZnO single crystal tubes grow along the <0001> direction with six (1100) planes joined at the (1000) mirror plane forming a perfect hexagon, as shown in Figure 3.4.

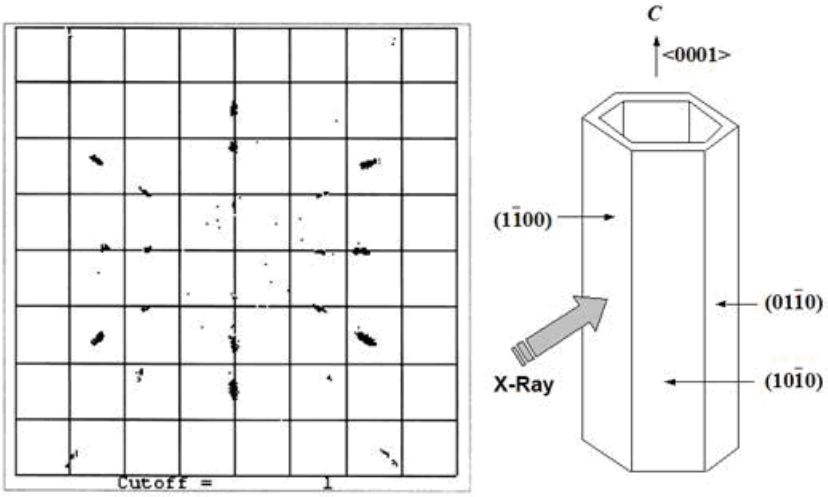


**Figure 3.4.** Laue X-ray back reflection patterns of the ZnO microtube

## 3.3 SYNTHESIS OF ZINC OXIDE WITHOUT SUBSTRATES

Much effort has focused on the on-chip controlled fabrication of nano/microstructures that is required by most planar device platform [37-40]. Therefore, one-dimensional structures of nanowires, nanobelts and microrods also have been prepared on different substrates materials (sapphire, silicon carbide, polycrystalline alumina) in the microwave processing system, which is schematically shown in Figure 3.5. The ZnO source material is the powder mixture of ZnO and graphite with molar ratio 1:1. The mixed powder is ground and pre-compressed to a quarter inch

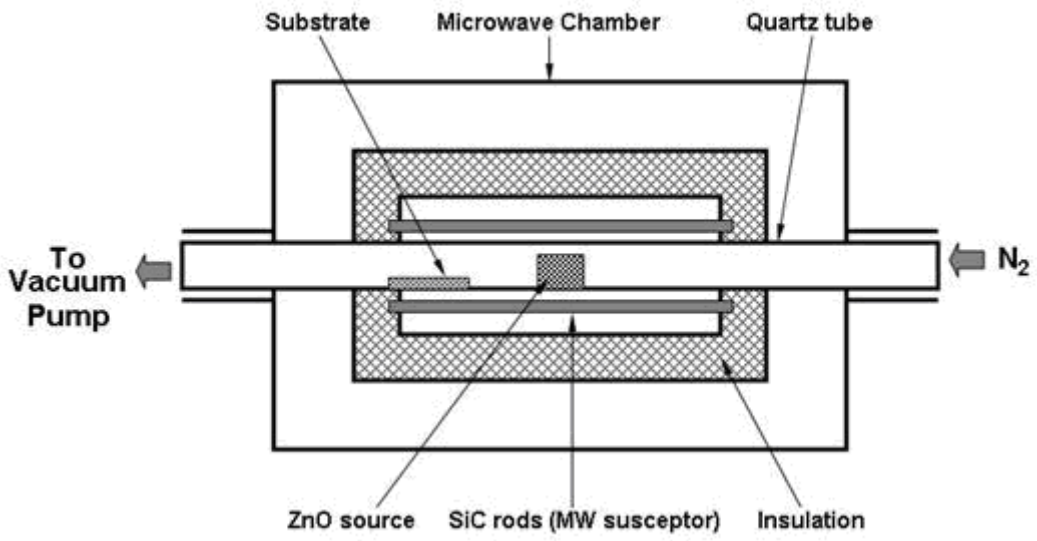


**Figure 3.5.** Schematic of the microwave growth of ZnO crystal structures on substrates

diameter cylinder. The cylinder is placed in a quartz tube and located in the center area of the microwave cavity. The substrates are typically placed 6~8 cm from the source material. The system is pumped down to a pressure of 300 torr, and nitrogen gas is then passed through the quartz tube at a constant flow rate of 25 sccm. The temperature of the source cylinder is ramped up to 1100 °C in 3~5 minutes and kept at that temperature for about 25 minutes, then the microwave power is shut down and the sample is cooled down to a room temperature naturally. Gray-colored products are found on the substrate. Because the heat is generated directly within the material in the microwave cavity, the ZnO/graphite mixture material absorbs much more microwave energy than the substrate, resulting in much higher temperature of the source cylinder compared to the substrate. By adjusting the separation distance of the source cylinder and the substrate, a desired temperature profile can be produced. The growth of ZnO structures followed the self- catalyzed and saturated thermal vapor-liquid-solid (VLS) mechanism, which is

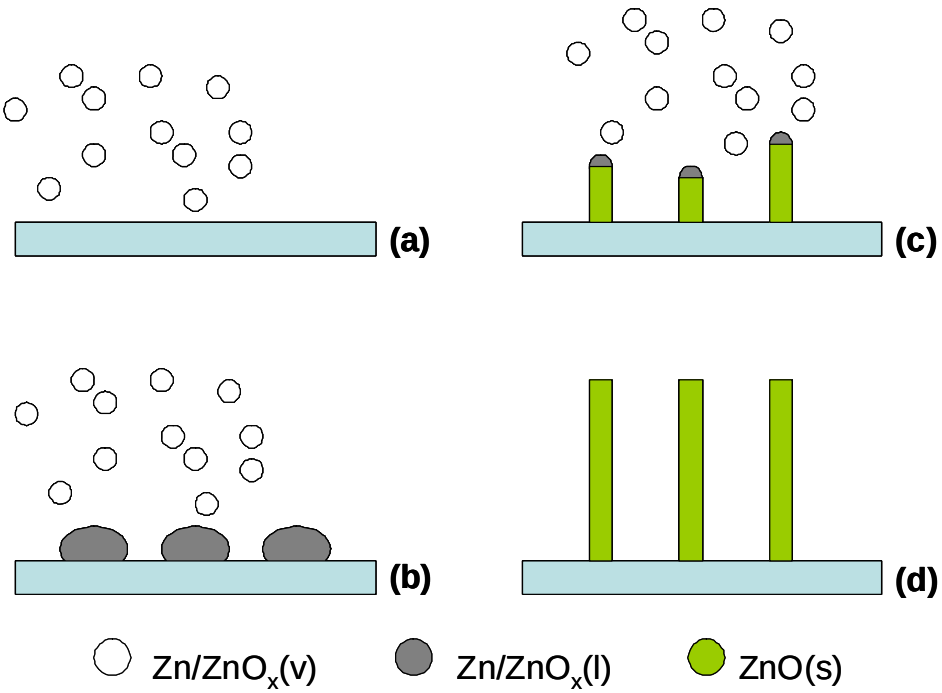


**Figure 3.6.** Schematic illustration of self-catalyzed and saturated VLS mechanism

illustrated in Figure 3.6. At the high temperature area (1100 °C), ZnO reacts with graphite or CO (formed in situ) to generate Zn, zinc suboxides and CO/CO2 vapor. The Zn and zinc suboxides mixture vapor is transported to the low temperature zone where condensation occurs to form liquid alloy droplets as nuclei for ZnO nano/microrostructures. The droplets are oxidized and enhanced absorption and diffusion of zinc oxides occurred at the liquid tips resulting in ZnO single crystal growth. The possible reaction may be as follows:

$$ZnO(s)+C(s)\rightarrow Zn(v)+CO(v) \quad (1)$$

$$ZnO(s)+CO(v)\rightarrow Zn(v)+CO_2 \quad (2)$$

$$ZnO(s)+(1-x)C(s)\rightarrow ZnO_x(v)+(1-x)CO(v) \quad (3)$$

$$ZnO(s)+(1-x)CO(v)\rightarrow ZnO_x(v)+(1-x)CO_2 \quad (4)$$

$$Zn(l) + ZnO_x(l) + O_2 \rightarrow ZnO(s) \quad (5)$$

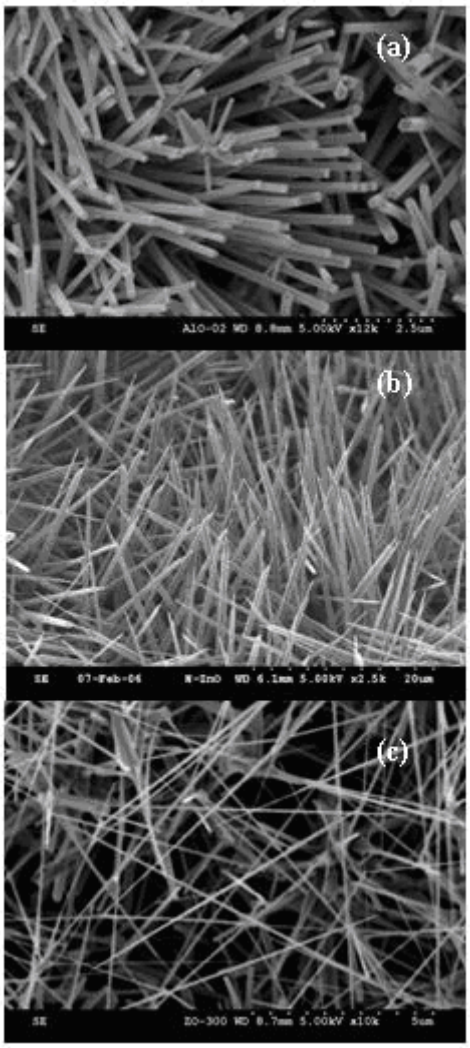


**Figure 3.7.** SEM images of ZnO nanostructures grown on (a) sapphire (110), (b) silicon carbide, (c) alumina

Scanning electron microscopy (SEM) images reveal that the products consist of a large quantity of ZnO nanostructures grown on three types of substrate materials, including sapphire (110), silicon carbide, and alumina (Figure 3.7). In the ZnO nanowires grown on the sapphire and the silicon carbide substrates, the diameter and the length is in the range of 70 to 400

nanometers and a few micrometers respectively. For the nanowires on the sapphire (110) substrate, the perfect hexagon end plane can be clearly identified in the SEM image (Figure 3.7A), providing strong evidence that the nanowires have a trend to grow along the <0001> direction and are well faceted at the end and side surfaces. For the substrate of silicon carbide, shown in Figure 3.7B, the cross-section of the nanowires is also hexagon, but the top tip is needle-like different from that of those nanowires on the sapphire. On the alumina plate, mass wool like nanobelts was observed without certain growth direction as shown in Figure 3.7C, with typical lengths in the range of several tens to hundreds of micrometers. X-ray diffraction (XRD) measurement was taken to examine the crystal structure of these ZnO nanostructures. All XRD patterns show that the samples are hexagonal wurtzite structure with the lattice constants of a=0.325nm and c=0.521nm. Figure 3.8 shows a typical XRD pattern of ZnO nanowires on the sapphire (110) substrate.

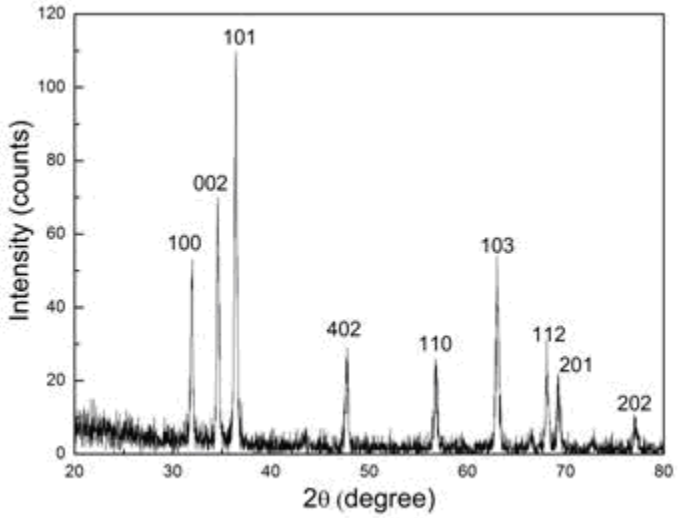


**Figure 3.8.** XRD pattern of ZnO nanowires on sapphire (110) substrate

The growth orientation is important for many applications of nano/microstructures. Using the proper substrate and the reaction conditions, the well-aligned nanostructures can grow vertically on the substrate. The study shows that there is a good epitaxial interface between the (0001) plane of the ZnO rod and the (110) plane of the substrate [46]. Therefore, the ZnO nanowires on the sapphire (110) should be preferentially oriented in the c-axis direction. Figure 3.7A also proved this prediction. Moreover, the orientation and diameter of the nanowires and nanorods can be controlled by some types of catalysts such as Ni or Au on the substrates. The mechanism is usally called catalyzed vapor-liquid-solid mechanism (VLS). In catalyzed VLS growth mechanism, it is generally believed that the catalyst particle at the tip determines the size and growth rate of the nanowire, and the surface termination of the substrate may have little effect on the growth. There are four main processes involved in this mechanism. Firstly, the catalyst such as Au or Ni ultra thin film usually of 10 nm is deposited on the substrate. Secondly, upon heating such substrate at the appropriate temperature, small size nanoparticles or droplets or eutectics of the catalytic material are created. Thirdly, when the vapors of the material of interest of deposition are transported towards the substrates, eutectics are formed. And finally, upon saturation of the eutectic, nanowire growth is started. A schematic cartoon image of the catalyzed VLS growth mechanism is shown in Figure 3.9. First, an Au thin film layer of about 10nm was sputtering on the sapphire (110) substrate as catalyst in the synthesis of ZnO nanowires using an metal Au target (99.999% purity, 2 inch diameter, 1/8 inch thickness, Angstrom Science, Inc.) in an AJA ATC 1300F custom magnetron sputter system. The sputtering was performed in argon atmosphere at room temperature. The flow rate of the Ar gas was set to 15 sccm, the DC power was 100 W, and the chamber pressure was down to $5x10^{-3}$ Torr. Thus, vertically well-aligned single crystal ZnO microrods with uniform diameter and

identical length have been synthesized in our microwave system. Figure 3.10 shows typical scanning electron microscopy (SEM) images of ZnO microrod arrays grown on a sapphire (110)

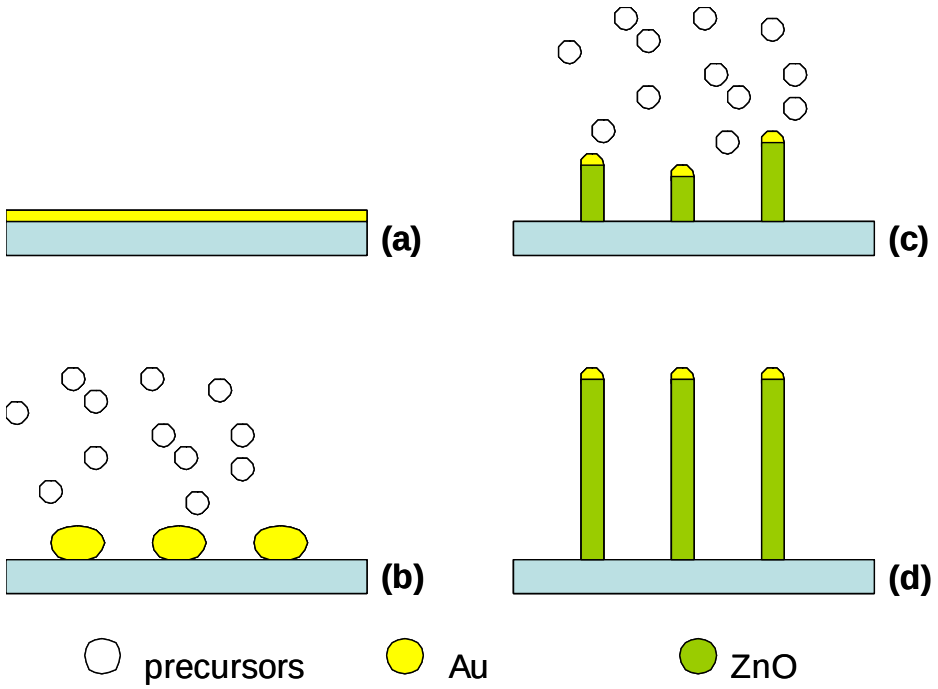


**Figure 3.9.** A cartoon illustration of the catalyzed vapor-liquid-solid growth mechanism showing the evolution of nanowires

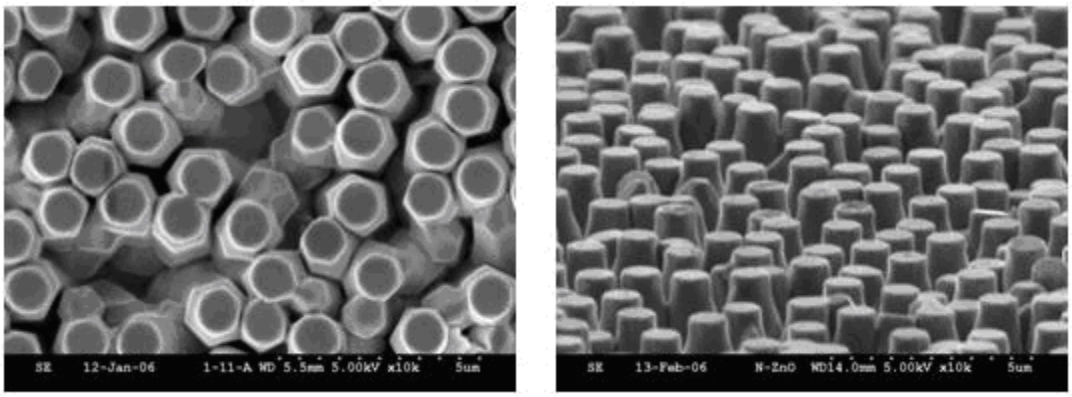

**Figure 3.10.** SEM images of highly crystallized ZnO microrods. Left: top view; Right: side view with 60º tilted.

substrate coated with a 10nm thick Au layer that was deposited by DC magnetron sputtering. At high magnification, the diameter of the ZnO microrods can be determined to be about 800nm. Nearly all of the rods grow vertically from the substrate. Hexagon end planes of the rods can be clearly identified in the SEM images, providing strong evidence that these rods grow along the <0001> direction and are indeed well-faceted at both the end and side surfaces. It is noted that the microwave grown ZnO microrods have identical lengths; the top ends of all ZnO microrods are in the same horizontal level, demonstrating a quite uniform growth during the microwave thermal evaporation-deposition process. The nature of these ZnO microrods with well-faceted surface, uniform diameter and identical length will have important implications when they are used as effective optoelectronic devices, such as electrical field emission devices. The crystal structure and orientation of the microwave grown ZnO microrod arrays are investigated using X-ray diffraction (XRD) method. From the XRD 2θ scan data of the ZnO microrods (Figure 3.11) only one sharp peak ZnO (002) is found at 34.32 degree position with very high intensity, indicating that the ZnO microrods are highly crystalline grown along with the c-axis orientation.

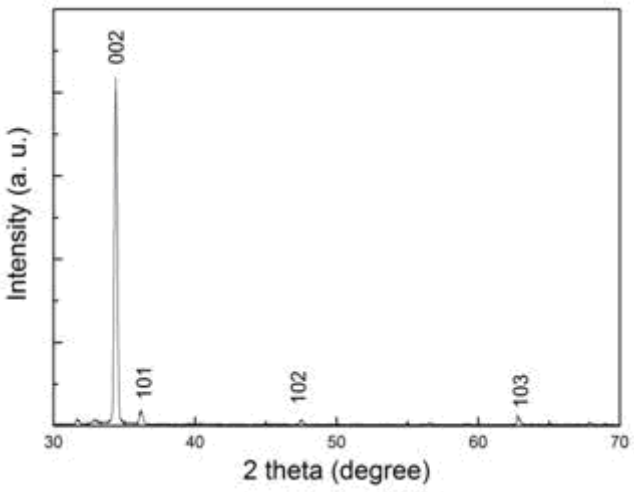


**Figure 3.11.** XRD pattern of ZnO microrod arrays

## 3.4 PHOTOLUMINESCENCE OF ZNO NANOSTRUCTURES

Photoluminescence (PL) is a nondestructive and contactless spectroscopic method of probing the electronic structures of materials. Light is shined in the samples, which is absorbed by the sample and upon de-excitation, light is emitted by the sample known as photo-excitation, and this mechanism is generally known as photoluminescence i.e, light is incident upon the sample and the emitted light is collected. In order to probe the band gap of a material, light of shorter wavelength (greater energy) is desired to excite the material. Photo-excitation causes electrons within the material, usually from valance band to move into permissible excited states. When these electrons return to their equilibrium states, the excess energy is released and may include the emission of light (a radiative process) or may not (a nonradiative process). The energy of the emitted light (PL) relates to the difference in energy levels between the two electron states involved in the transition between the excited state and the equilibrium state. The quantity of the emitted light is related to the relative contribution of the radiative process. The intensity and spectral content of this photoluminescence is a direct measure of various important material properties such as chemical composition, structure, impurities, kinetic processes and energy transfer.

In semiconductors the most common radiative transition is between energy states in the conduction band and the valence bands. The energy difference is commonly known as the band gap. Band gap determination is very important for new compound semiconductors. The photoluminescence energy associated with the radiative transitions which involve localized defect levels can be used to identify specific defects. To return to equilibrium state after excitation, both radiative and nonradiative processes take place in the process. The amount of photoluminescence and its dependence on the level of photo-excitation and temperature are

directly related to the dominant recombination process. Analysis of photoluminescence helps to understand the underlying physics of the recombination mechanism. In general, a nonradiative processe is associated with localized defect levels, which determine the material quality and subsequent device performance. Therefore, material quality can be measured by quantifying the amount of radiative recombination. An energy diagram representation is shown in figure 3.12.

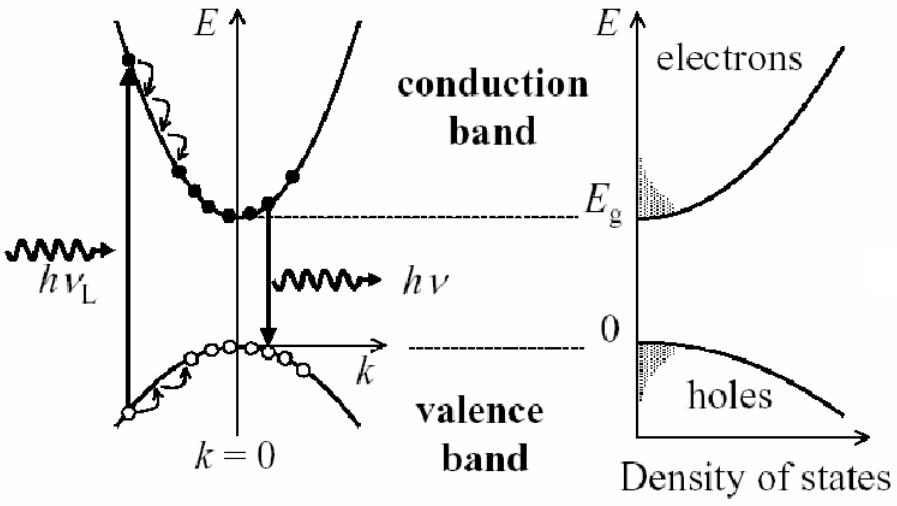


**Figure 3.12.** Schematic diagram of the PL mechanism

Photoluminescence (PL) spectra of microwave grown ZnO microtubes were measured at room temperature with a 266 nm microchip laser (Microchip NanoUV-266, JDS Uniphase) as an optical pumping source, which was operated at a repetition rate of 10 Hz and 4 ns pulse length with an estimated peak power 1-1.5 kW and an average power 4-6 mW. The laser beam was focused on the side-wall of the ZnO microtube at an incidence angle 60 degree to the symmetric axis (c axis) of the ZnO microtube (Figure 3.13A), and the photon emissions were collected perpendicularly of the sample tube by a monochromator (ISA, Edison). A strong near band-edge emission peak was detected at a wavelength of 377.8 nm with a full-width at half-maximum

(FWHM) of 11 nm. A smaller shoulder peak near 392-395 nm was noted that might be attributed to oxygen vacancies in the ZnO crystals. The 532 nm peak in Figure 3.13A was from the second order harmonic of the excitation laser source.

The PL spectrum of microrod arrays also was measured at room temperature using a fluorescence spectrophotometer (Hitachi 4000) with a Xe lamp as the excitation light source. A strong emission peak was detected at a wavelength of 378 nm that is contributing to the near-band-edge emission (Figure 3.13B).

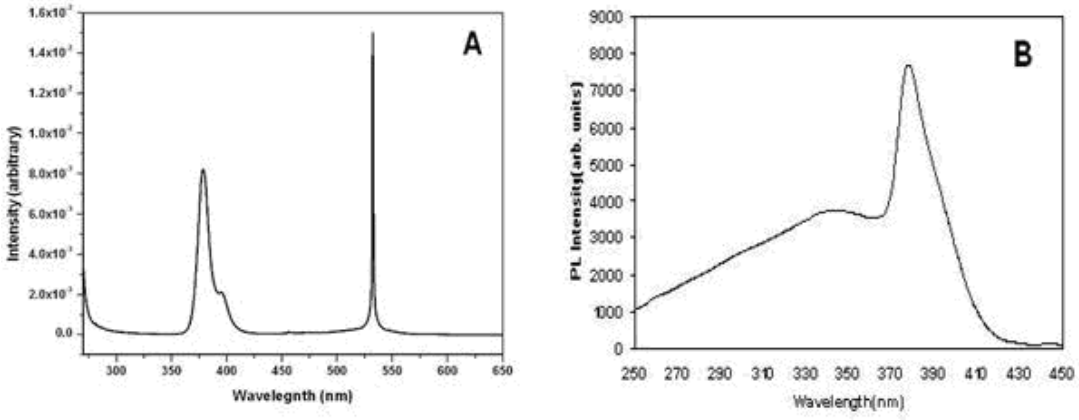


**Figure 3.13.** Photoluminescence spectra (PL) of ZnO. A microtubes, B microrods

## 3.5 CONCLUSIONS

Large-scale one-dimensional ZnO microtubes, microrods, nanowires, nanotubes, and nanobelts were fabricated in the microwave process system by a thermal evaporation-deposition method. XRD and SEM investigations showed that these products are pure, structurally uniform, and single crystalline. The temperature, substrate, and catalyst showed significant impacts on the

controlled on-chip growth of those ZnO structures. When the growth temperatures were below 1150°C, ZnO crystal wires or belts (with diameters from 50 nanometers to a few microns) were obtained; when the growth temperature exceeded 1300 °C, the hexagonal tubular growth became predominant. In addition, vertically well-aligned single crystal ZnO microrods can be achieved while the proper substrate sapphire (110) and the catalyst Au are selected. The photoluminescence (PL) of ZnO microtubes and microrods were measured and exhibited strong ultraviolet emission at room temperature, indicating potential applications for short-wave light-emitting photonic devices. Moreover, the presented synthesis of ZnO lower size structures using microwave is a simple and easy-controlled approach, which also provides exciting prospects for fabricating nano/microstructures of many other semiconductors, such as GaN, SnO2, and CdO.

# 4.0 ZINC OXIDE NANOWIRE ARRAYS FOR HIGH TEMPERATUER GAS SENSING

## 4.1 INTRODUCTION

High temperature gas sensors have been attracted much attention due to the growing concern of environmental protection, safety and energy saving, especially in harsh industries such as automotive, aerospace, and space exploration [47]. In particular, nitrogen oxides (NOx) coming from combustion facilities and vehicles causes a wide variety of health and environmental impacts because of various compounds and derivatives in the family of nitrogen oxides, including nitrogen dioxide, nitric acid, nitrous oxide, nitrates, and nitric oxide. The exhaust of NOx gases is strictly regulated. Therefore, there is an increasing need to detect low concentrations of nitrogen oxides at elevated temperature, which will help to reduce environmental pollution and increase fuel efficiency.

Acoustic technology has been widely investigated for gas sensing applications in the past years due to high sensitivity and structural simplicity. For example, thickness shear mode (TSM) quartz resonator with active layer has been widely used for gas detection through the measurement of resonance frequency shift. The active layer that absorbs/desorbs the target gas will have a mass loading change. The frequency change is related to mass change by the Sauerbrey equation:

$$\Delta f = -\frac{2 f_0^2 \Delta m}{A(\rho_q \mu_q)^{1/2}} \quad (1)$$

Where $f_0$ is the resonant frequency, $A$ is the active electrode area and $\rho_q$ and $\mu_q$ are the density and shear modulus of the crystal, respectively.

However, for high temperature (>350ºC) and in-situ gas sensing in advanced power generation systems, the applicability of quartz crystal based on bulk acoustic wave (BAW) resonator is limited. At elevated temperature, temperature fluctuation, even very small, still produces large resonance frequency shift because of high temperature coefficient of frequency, which leads a large temperature-induced mass sensing error. In addition, with temperature increase the material properties of the piezoelectric crystal are subjected to substantial changes and it may even lose piezoelectricity, which significantly affects the performance of acoustic wave resonator sensors. The highest operation temperature of quartz BAW resonator is reported to be about 450ºC because of high mechanical loss at higher temperature and α-β phase transition at 573ºC, at which the quartz crystal losses its piezoelectricity [48].

Langasite family compounds, including LGS, LGT, and LGN, have the Ca3Ga2Ge4O14 type trigonal structure, which was discovered in 1980 [49]. Currently there are approximately 100 known compounds with this structure. Unfortunately, most of them melt incongruently and thus are difficult to produce. LGS, LGT, and LGN are the three most commonly cited compounds, since they melt congruently around 1470ºC which allows large single crystals can be produced by the conventional Czochralski melt pulling technique with no phase transition between the melting point and room temperature [50]. Electromechanical properties were also investigated [51, 52]. The propagation characteristics of surface acoustic wave (SAW) and bulk

**Table 4.1.** Properties of langasite [60]

| | |
|---|---|
| **Density (Kg/m3)** | 5764 |
| **Melting point(℃)** | 1470 |
| **Phase transistion temperatures(℃)** | None (from room temperature to its melting point) |
| **Moh's hardness** | 6.6 |
| **Crystal structure** | Trigonal, point group 32, space group P321 |
| **Lattice parameter(Å)** | a=8.1-8.2, c=5.1-5.2 |
| **Coeff. Thermal Expansion (ppm/K)** | a11=5.1 a33=3.6 |
| **Elastic compliances(1012 M2/N)** | S11=8.75, S33=5.31, S12=-4.02, S13=-1.88, S44=21.99, S66=25.54 |
| **K2 (%)** | 0.3-0.4 |
| **Acoustic velocity (m/s)** | 2400 |
| **Temperature coefficient (ppm/K)** | 1-2(room temp) |
| **Frequency constant (KHz.mm)** | 1380 |
| **Piezoelectric constant (1012 C/N)** | d11=-6.2, d14=5.4 |
| **Attenuation value (dB/cm)** | 1.9 (shear mode), 0.5(long. mode) |

acoustic wave (BAW) on LGS substrate were studied in the 90's [53, 54]. These studies show that LGS has several highly desirable properties superior to the current material quartz. LGS has a higher electromechanical coupling, which will allow a bandwidth three times wider than that of quartz. The acoustic velocity of the LGS family is smaller than the velocity of quartz, leading one to expect a small-sized SAW filter. In addition, LGS has the same temperature compensation property as quartz so that the frequency is stable within a reasonable temperature range. In addition, the Q-value of bulk-wave resonators was measured about twice that of quartz [55, 56]. Due to the high phase transformation temperature LGS has been explored for high temperature BAW and SAW device, and sensor applications [57-59]. Key properties of langasite are listed in Table 4.1 [60]. Langasite has a chemical formula of $A_3BC_3D_2O_{14}$ [15], where A, B, C and D indicate particular cation sites. A is a decahedral site coordinated by 8 oxygen atoms. B is octahedral site coordinated by 6 oxygen atoms, and C and D are tetrahedral sites coordinated by 4 oxygen atoms. The LGS crystal and structure are shown in figure 4.1 and 4.2 [61].

**Figure 4.1.** Langasite (LGS) crystal

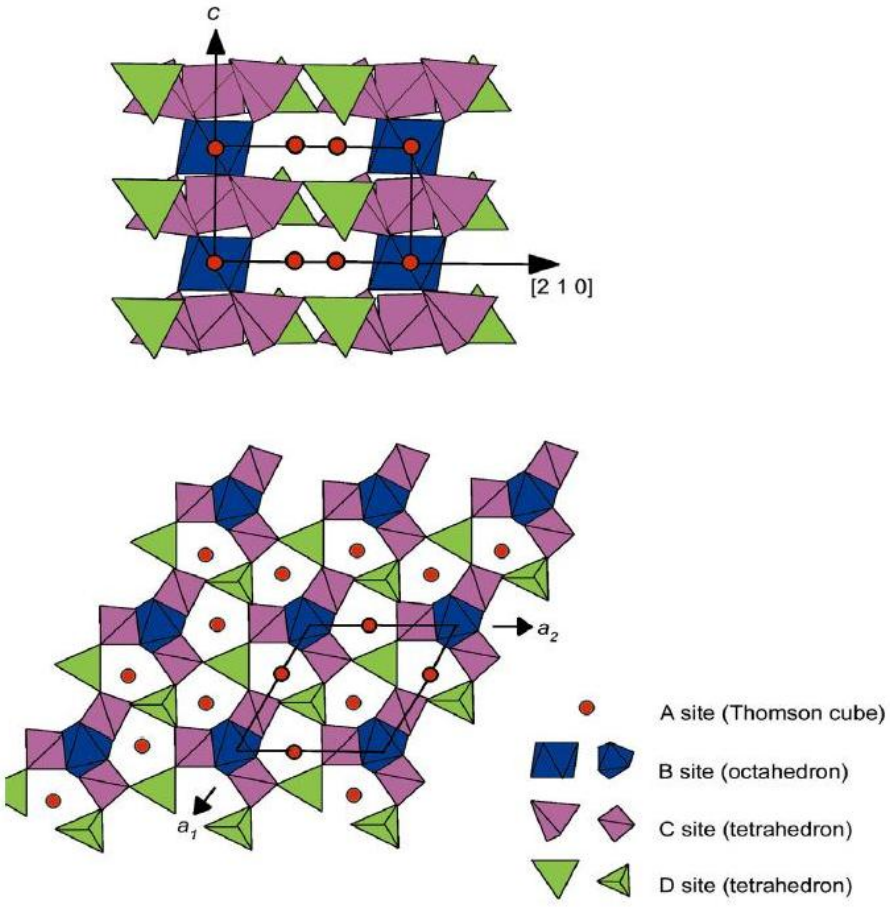


**Figure 4.2.** Crystal structure of Langasite (LGS) [61]

Zinc oxide, an n-type metal oxide semiconductor with wide bank gap, is one of the most widely applied oxide gas-sensing materials due to its high chemical stability, low cost, and good flexibility in fabrication [62]. ZnO films also have been extensively investigated for surface acoustic wave devices and bulk acoustic wave devices, especially for the detection of inflammable and toxic gases owing to its excellent piezoelectricity, substantial electromechanical coupling coefficient, and good temperature stability [63, 64]. However, the sensing performance such as the response speed is often limited by the grain sizes, surface states, and gas adsorption and dissociation rate and the diffusion rate in the thin film materials [65]. The emergence of nanoscale science and technology in recent years is making a significant impact on gas sensors. Novel nanoscale sensors show great promise as they have faster response and higher sensitivity than planar sensor configurations, due to their smaller dimensions combined with dramatically increased sensing surface and strong binding properties. To date, various one-dimensional ZnO nanostructures have been realized in forms of nanowires, nanobelts, and nanotubes [18, 37, 66]. Those ZnO nanostructures have a high surface to volume ratio, and have been regarded as promising material to improve the gas sensing performance. Recently, gas sensors based on ZnO nanostructures have been demonstrated for toxic and combustible gas sensing, and these sensor show increased sensitivity and accuracy [67].

Thus, it is believed that the combination of ZnO nanowire arrays with high temperature acoustic wave resonator such as langasite thickness shear mode (TSM) resonators would provide an ideal gas sensing platform for both higher sensitivity and enhanced response speed. In this chapter, we present our study on the fabrication and characterization of langasite thickness shear mode (TSM) resonator gas sensors using ZnO nanowire arrays as the active layer.

## 4.2 PREPARATION AND CHARACTERIZATION OF GAS SENSOR

The thickness shear mode (TSM) langasite device with ZnO nanowire arrays is schematically shown in figure 4.3. The sensor started from 6 MHz Y-X cut polished langasite thickness shear mode resonator (Fomos-Materials Company, Russia) with gold electrodes. ZnO nanowire arrays were grown on one side of the resonator according to a two-step hydrothermal method [68].

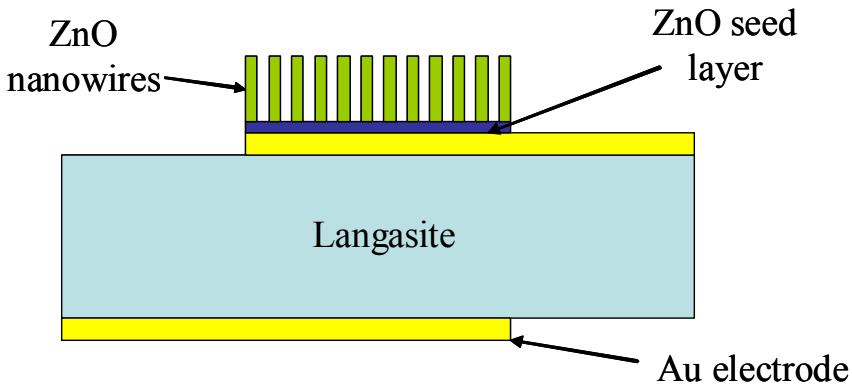


**Figure 4.3.** Schematic of langasite gas sensor coated with ZnO nanowire arrays

First, the langasite resonator was cleaned thoroughly by acetone/ethanol sonication, and then blown dry by nitrogen gas. After that, the resonator was wet with a drop of 5mM zinc acetate dehydrate (98%, Aldrich) in ethanol, and then blown dry with a stream of nitrogen after 10 seconds. This coating step was repeated five times. The substrate with a film of zinc acetate crystallites was heated to 350℃ in air for 20 min to yield layers of ZnO islands with their (0001) planes normal to the substrate surface as shown in figure 4.4. The zinc acetate deposition and decomposition procedure was carried out three times to ensure a complete and uniform coverage of ZnO seeds. The hydrothermal reaction solution for ZnO nanowire arrays growth was prepared

by mixing 25mM zinc nitrate hydrate, 25mM hexamethylenetetramine and 6mM polyethylenimine solution in a bottle with an autoclavable screw cap. Since only one side needed to grow ZnO nanowire arrays, the other side of the resonator was first protected by coated PMMA film in case of any contamination. The seeded resonator was immersed vertically in the solution, and the sealed bottle was heated to 90ºC for 6 hours inside a conventional laboratory oven. Subsequently, the resonator was rinsed repeatedly with deionized water and annealed in a muffle furnace at 400ºC for 1 hour to remove any residual organics and stabilize nanostructures. The morphology and structure of grown ZnO nanowire arrays were characterized using scanning electron microscopy (SEM) and x-ray diffraction (XRD).

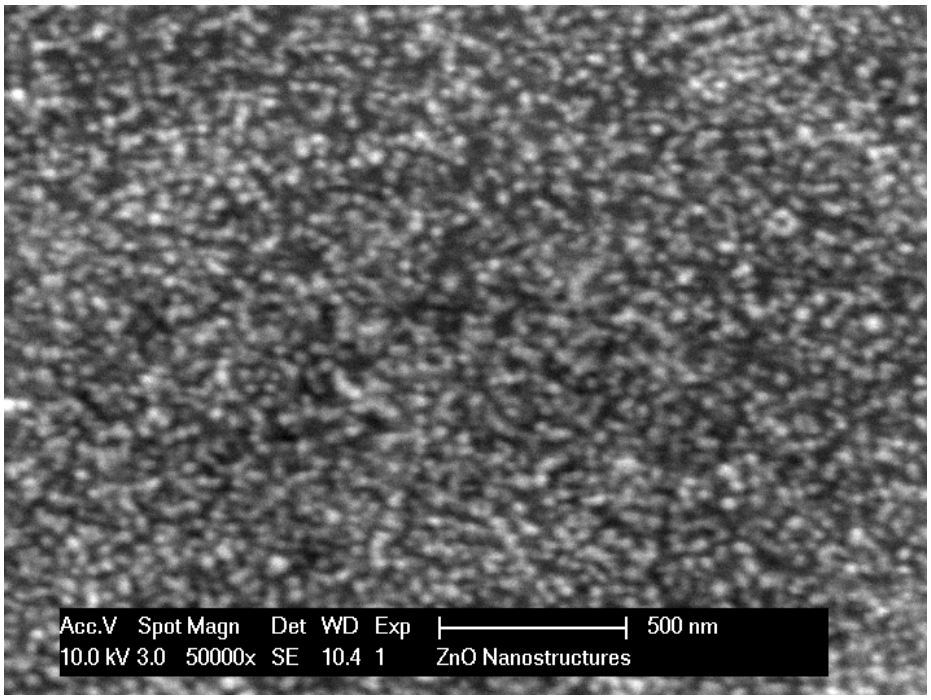


**Figure 4.4.** SEM image of ZnO seeding layer

The XRD pattern in figure 4.5(a) shows that the grown ZnO nanowire arrays can be indexed to the wurtzite phase of ZnO with lattice constants of a=0.325 nm and c=0.520 nm. Only

one sharp peak ZnO (002) is found at 34.32 degree position with strong relative intensity. The absence of peaks for other ZnO orientation indicates that ZnO nanowires have a preferred orientation along the c-axis. Figure 4.5(b) and (c) show typical scanning electron microscopy (SEM) images of ZnO nanowire arrays. The nanowires are found to be uniformly distributed and well aligned normal to the surface of the substrate. In addition, the nanowires have a diameter ranging between 50 and 100 nm, and a length of about 1.5 um.

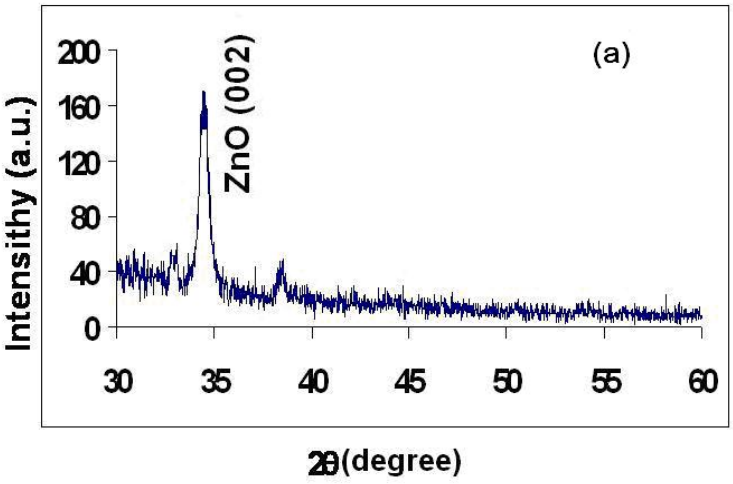


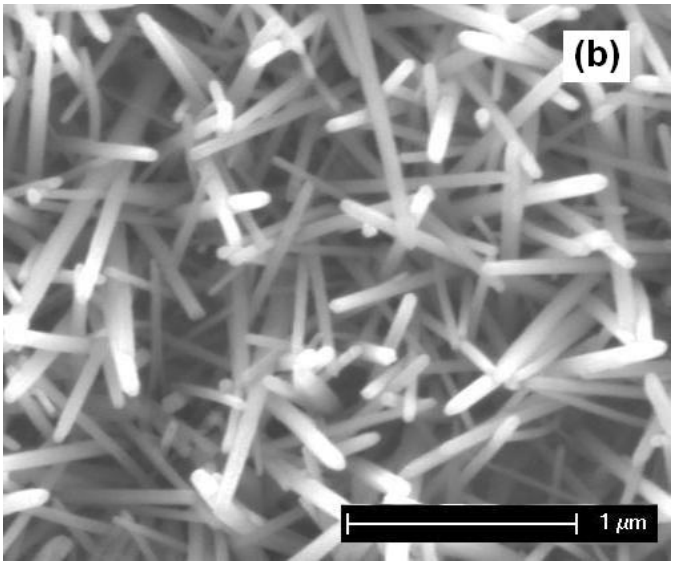

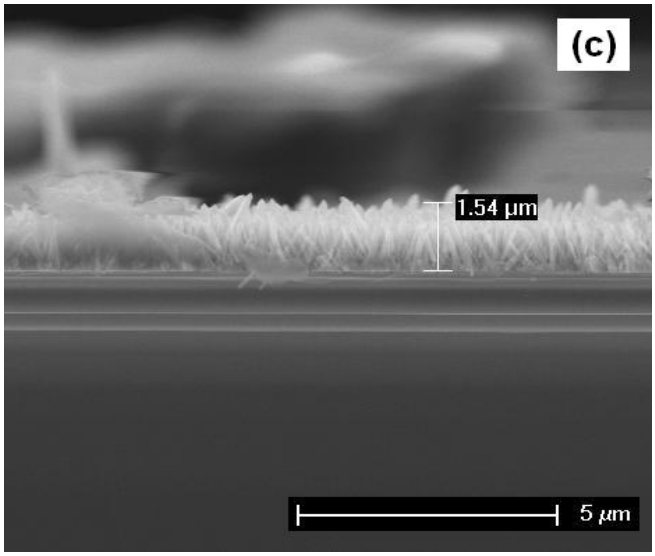


**Figure 4.5.** Characterization of ZnO nanowire arrays (a) XRD, (b) & (c) SEM images: top and cross section

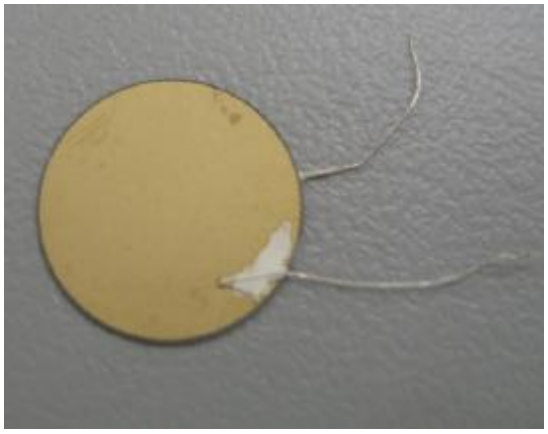

**Figure 4.6.** LGS gas sensor coated with ZnO nanowire arrays

After ZnO nanowire array was grown on the LGS resonator, silver wires of diameter 0.005 inch were connected to the top and bottom electrode of the resonator by high temperature silver paste. Then, the sensor was placed on the level hot plate at 60°C for 4 hours to solidify the silver paste. Figure 4.6 shows the langasite thickness shear mode resonator gas sensor, the top surface was coated with ZnO nanowire arrays as the sensitive layer.

## 4.3 EXPERIMENTAL SETUP AND TESTING

Sensor testing was performed in our custom designed CVD 200M system (Tek-Vac Industries Inc.) as shown in Figure 4.7. The TEK-VAC CVD 200M system is an excellent and versatile experimental chemical vapor deposition system. It offers continuous high temperature operation (1100°C) over a broad pressure range. The quartz tube (50mm outside diameter) reactor is enclosed with a high watt density Thermolyne furnace and insulated ceramica wool for rapid temperature acceleration to the set point. The process temperature is controlled by a PID temperature controller. The water cooled, double "O" ring sealed, spool pieces act as collets to support and seal the quartz tube to the process. A horizontal support mechanism and spool piece clamps, prevents the collapse of the vacuum or pressure end caps during operation. Access to the high temperature reactor region is easily accomplished with a flanged cantilevered supported susceptor located on the right spool piece. The flange with its associated cantilever is withdrawn from the reactor, the flange has 8 pin ceramic feed-through for making electrical connections to the inside of the reactor. The system is also supplied with three gas flow controllers with positive shut-off valves for the multiple injection applications.

The LGS resonator mounted on the ceramic plate was placed in the air-tight quartz tube chamber in our custom CVD 200M system for atmospheric and temperature control. Very thin silver wires were bound to the resonator's electrodes through high temperature conductive paste. And the other end of platinum wires was connected to the switch unit (34970A, Agilent), which allows to choose the desired resonator for measurement. The impedance spectrum of resonators was achieved through an impedance analyzer (4294A, Agilent), which was used to extract the fundamental resonance frequency through data fitting method. A computer with Hi-Speed GPIB

Controller (GPIB-USB-HS, NI) and program (Labview7.0, NI) were used for automatic measurement and data saving. The schematic of test set-up is shown in Figure 4.8.

**Figure 4.7. C**ustom CVD 200M system

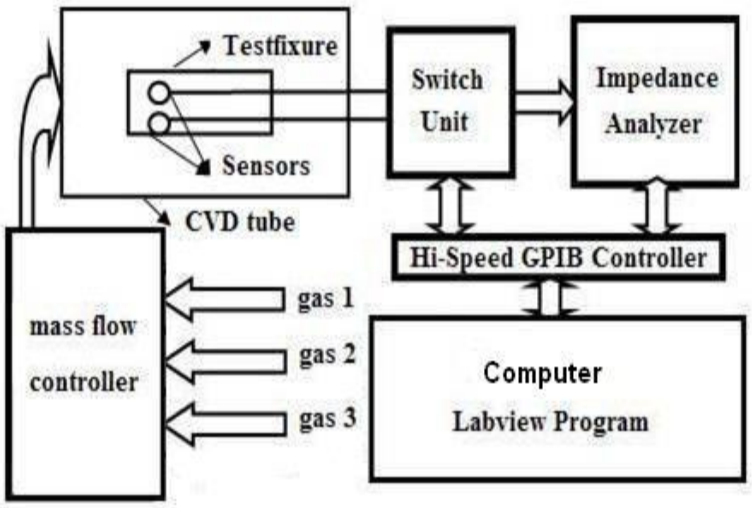


**Figure 4.8.** Schematic of test set-up

Gas species of interested were continuoustly flowed into the chamber, and the flow rate and gas composition were controlled manually using mass flow controllers (3 flow valves, MKS 179A, with multi-channel mass flow controller MKS 1179A). The testing gases were $NO_2$ and $NH_3$ with various concentrations in dry air with a total flow rate of 200 sccm at 300℃. Here 300℃ was selected due to the frequency of LGS resonator was most stable at this point. Generally, the test result was not related to the flow rate if the flow remained constant.

## 4.4 RESULTS AND DISCUSSION

Figure 4.9 shows the time-cycling response of the ZnO nanowire arrays to 250ppm $NO_2$ in dry air at the optimal operating temperature 300℃. First, 200 sccm dry air was droved through the chamber until the langasite resonator's frequency change become smaller than 1 Hz/min. In this state, we can say that the langasite resonator reaches a balance. Usually, this process takes about 3 hours. Then, 250ppm $NO_2$ in dry air was applied to the test system for 10 minutes with the same flow rate as the previous step. Thereafter, 200 sccm dry air was used again to recover the device. All the processes were undertaken at 300℃ and controlled humidity environment. The frequency of the ZnO nanowire arrays sensors reduces with the presence of $NO_2$. The reversible cycles of the response curve indicate a stable and repeatable operation of gas sensing. However, here is found that the desorption process of $NO_2$ is much slower than adsorption process.

A frequency-changing rate $S_f = |\Delta f / \Delta t|$ is defined to reflect the sensor sensitivity [69]. The larger $S_f$ value means the bigger frequency shift per unit time and thus the higher

sensitivity. Figure 4.10 shows the corresponding relationship between $S_f$ and the $NO_2$ gas concentration. It is obvious that the frequency-changing rate increases with increasing $NO_2$ concentration.

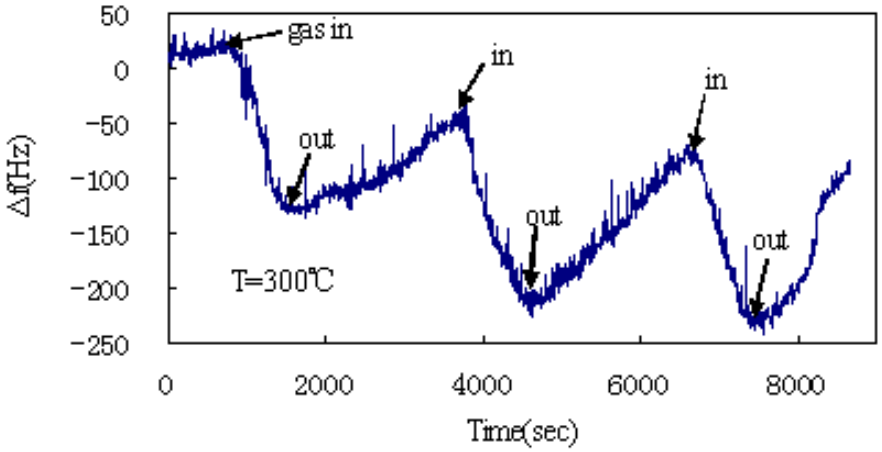


**Figure 4.9.** Time cycling response to $NO_2$ at 300℃

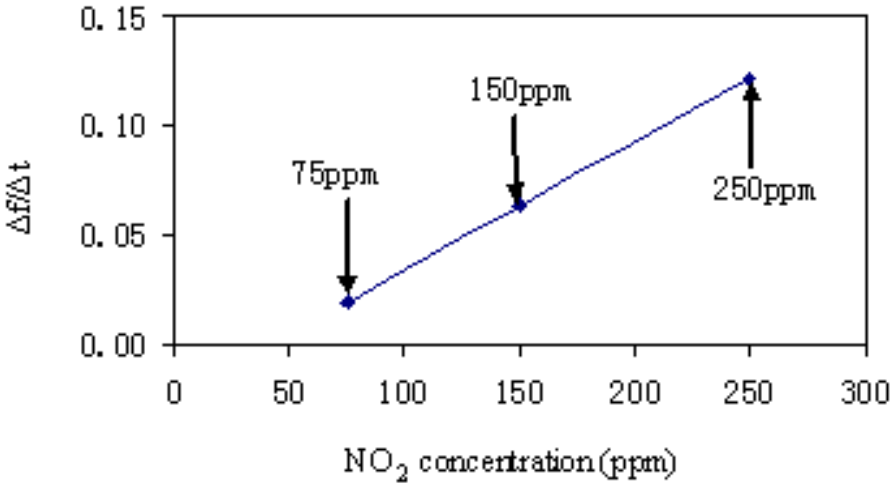


**Figure 4.10.** Frequency sensitivity vs. $NO_2$ concentration at 300℃

The response of ZnO gas sensor to reducing gas $NH_3$ was also tested. Figure 4.11 shows the time cycle response to 250ppm $NH_3$ and Figure 4.12 shows sensitivity to different

concentrations. Both experimental procedures were same as $NO_2$. It could be seen that the ZnO gas sensor presents sensitive and reversible response to $NH_3$. The sensitivity also increases with increasing $NH_3$ concentration.

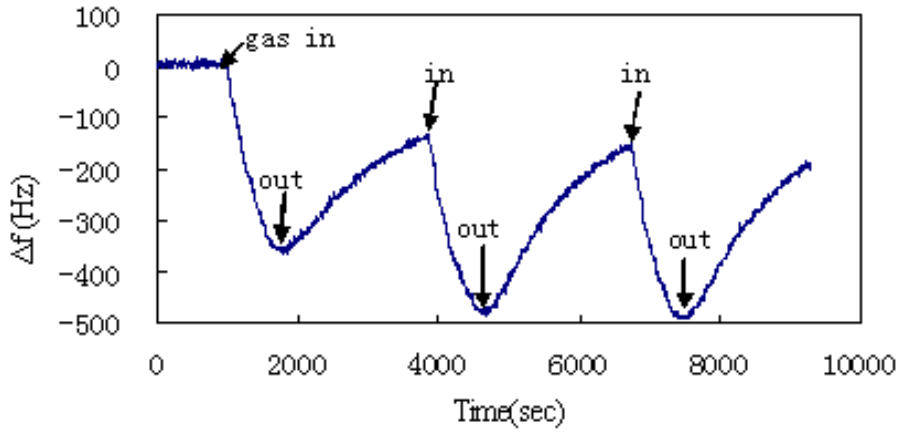


**Figure 4.11.** Time cycling response to 250ppm $NH_3$ at 300℃

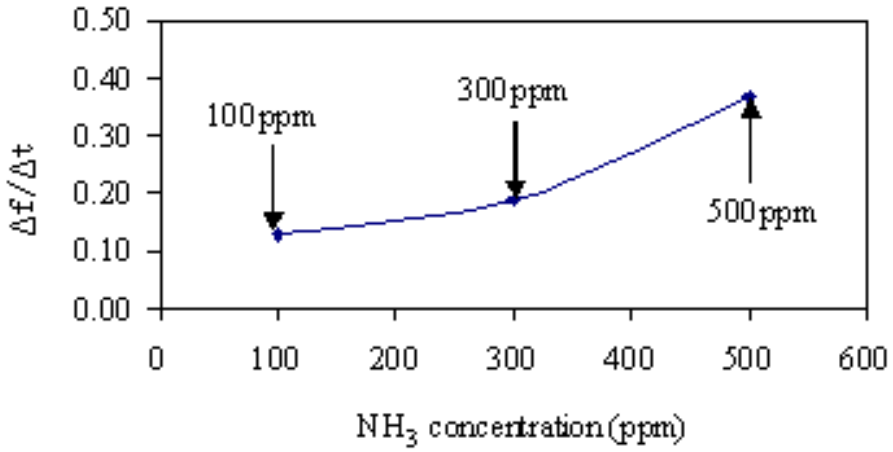


**Figure 4.12.** Frequency sensitivity vs. $NH_3$ concentration at 300℃

In the $NO_2$ detection, $NO_2$ can be adsorbed or can interact with the oxygen adsorbed onto the active ZnO nanowire layer surface according to the following reactions [69]:

$$NO_{2g} + e^{-} \rightarrow NO_2^{-} \quad (2)$$

$$NO_{2g} + O_2^{-} + 2e^{-} \rightarrow NO_2^{-} + 2O^{-} \quad (3)$$

The adsorbed ions $NO_2^{-}$ are desorbed as $NO_2$ gas when $NO_2$ flow is stopped and consequently in this process a recovery of the initial conditions takes place. Moreover, those oxygen vacancies on the surface of ZnO nanowires also might involve in the processes of physical or/and chemical adsorptions of $NO_2$ [70]. These oxygen vacancies are the chemisorption sites:

$$NO_2(g) + V_O \rightarrow (V_O - O_{ads}) + NO(g). \quad (4)$$

Oxygen desorption occurs by the reaction,

$$2(V_O - O_{ads}) \rightarrow 2(V_O)_s + O_2(g) . \quad (5)$$

The existence of new $NO_2^{-}$ and NO species on the ZnO surface indicates the reaction between $NO_2$ and ZnO, which causes the mass change. The formation of new species may also change the mechanical and electronic properties of the ZnO nanowires layer. Furthermore, the possible ZnO/langasite interfacial stress changes may also affect the resonant frequency of the device. However, the precise verification of this interfacial effect is difficult due to complicated behavior of ZnO-langasite sensor. Therefore, the high sensitivity of ZnO gas sensor is achieved due to the small grain size and high surface to volume ratio associated with the ZnO nanowires. At this scale, the vertically aligned morphology of ZnO nanowires provides not only a variety of channels for surface interactions between chemisorbed oxygen species and target gases, which make more surface exposed to the testing gas, but also more oxygen vacancies compared with the flat thin film. As a result, the sensing properties of ZnO nanowire arrays were improved.

As the sensing mechanism of $NH_3$, it also is a process of physical and chemical adsorption. Besides $NH_3$ molecules are adsorbed on the sensitive layer at a short time due to the

large surface area of ZnO nanowires, there is a chemical interaction between the reducing gas $NH_3$ and the negatively charged $O^-$ ions on the nanowires surface, as described by Equation (6) [71]:

$$2NH_3+3O^- \rightarrow 3H_2O + N_2 + 3e^- \quad (6)$$

## 4.5 CONCLUSIONS

In summary, The LGS resonator high temperature gas sensor was fabricated. Ordered ZnO nanowire arrays were grown on the langasite resonator as the sensitive layer by two-step hydrothermal method at low temperature. The gas sensor coated with ZnO nanowire arrays exhibited good gas sensing properties to $NO_2$ and $NH_3$. The reproducibility is good since the metal oxides are very stable. The response of the sensor is fast due to the huge surface area of ZnO nanowires. In addition, this work demonstrates that the combination of nanowire arrays with langasite thickness shear mode resonators could provide a promising high temperature gas sensing platform with both high sensitivity and enhanced response speed.

# 5.0 FABRICATION AND CHARACTERIZATION OF ZINC OXIDE NANOCOMPOSITES

## 5.1 INTRODUCTION

Polymer-based nanocomposites are becoming an attractive set of materials due to their multifunction and many potential applications [72]. These materials are expected to possess unique electric, magnetic, optical, and mechanical properties which can be significantly different from those of the individual material. Applications of nanocomposites may encompass several industries including electronics, display, energy, and other industries. Novel properties of nanocomposites can be obtained by successfully imparting the characteristics of nanomaterials to a single matrix material. These materials differ from both the pure polymers and the nanomaterials in some physical and chemical properties. Encapsulation of nanomaterials inside polymers is the most popular and interesting approach to synthesize nanocomposites.

Polyimides are a class of polymers with material properties that are used in many applications. Polyimides are synthesized by reaction of a dianhydride and a diamine. The first commercial polyimide was developed by Dupont in 1961, based on pyromellitic dianhydride and 4,4-diaminodiphenyl ether [73]. Polyimides show stability at high temperatures and exhibit high glass transition temperatures in the range of 300-400°C. These materials offer mechanical

properties, as well as chemical resistance and low dielectric constant [74]. For these reasons, polyimides are desirable materials for many structural and electronic component applications.

The objective of our work is to combine ZnO nanowires with polyimide polymer matrix to develop a novel polymeric nanocomposite for multifunctional applications that require self-sensing and self-actuation capabilities. We propose to design ZnO nanowires-polymer composites whose morphology in the polymer matrix is micro-tailored by itself or external electric fields. The goal is to achieve controlled alignment and dispersion of ZnO nanowires in the polymer matrix, resulting in a composite that combines electrostrictive and piezoelectric properties. Electromechanical response of such nanocomposite is expected to exceed the best single-phase ceramics, polymers or thin films currently available and preserve advantages of the polymers.

## 5.2 FABRICATION OF ZNO-POLYIMIDE NANOCOMPOSITES

For polymeric matrix composites, the assembly of composite materials is the key to success. ZnO nanowires, however, have rarely been used as inclusions in a polymer matrix because of the difficulty in achieving efficient dispersion. Intrinsic van der Waals attraction among nanowires, in combination with their high surface area and high aspect ratio, often leads to significant agglomeration, thus preventing efficient transfer of their superior properties to the matrix. In this study, two methods: self-alignment and external electric field assisted alignment were developed to efficiently disperse ZnO nanowires into a given polyimide matrix on a nanoscale level to produce the novel ZnO-polyimide nanocomposite.

### 5.2.1 ZnO Nanowires Self-alignment Method

The self-alignment method is a kind of bottom-up fabrication process. First, vertically aligned ZnO nanowires are controlled to grow on the substrate. Then, the liquid polyimide is spincoated into the ZnO nanowire layer on the substrate to produce the ZnO/Polyimide nanocomposites. The structure of ZnO nanocomposite prepared with this method is schematically shown in Fig. 5.1. The difficulty of this process is to make the liquid polyimide fully fill in the nanowires layer. Here we tried to overcome those problems in two directions: one is to make ZnO nanaowires have proper length, density and gap between each other to fit polyimide casting. The other is to find the optimized process parameters of the second step, such as polymer concentration, spin coating speed, to get the uniform nanocomposites.

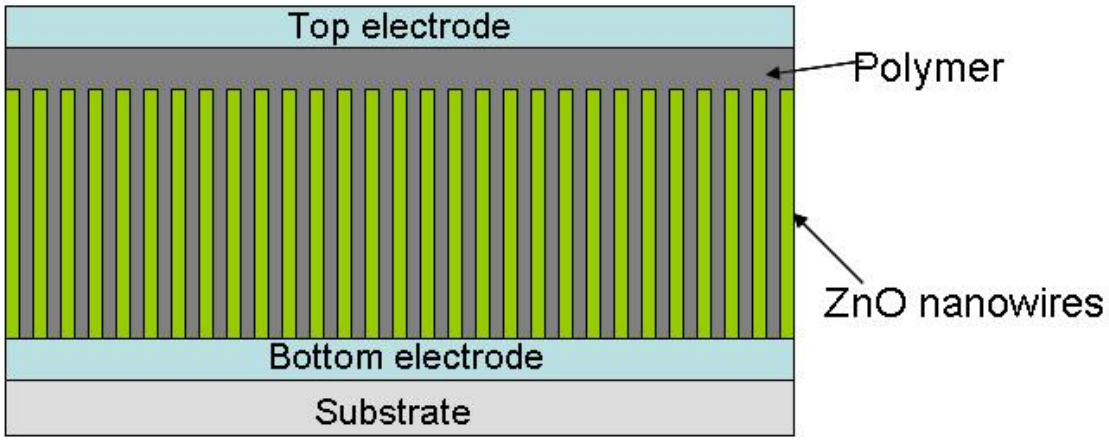


**Figure 5.1.** Schematic diagram of self-alignment ZnO nanocomposite

High-quality vertical self-aligned ZnO nanowire arrays were synthesized on the top of substrates with Au electrode according to a two-step hydrothermal method [68] same as in chapter 4. First, the thin films of Au and Cr were sputter deposited on the Si (100) wafer using

metal Au and Cr targets (99.999% purity, 2 inch diameter, 1/8 inch thickness, Angstrom Science, Inc.) in a AJA ATC 1300F custom magnetron sputter system. The Si substrate was ultrasonically cleaned in acetone for 10 minutes, rinsed in deionized water, blown dry with the nitrogen gas, and subsequently placed on the hot plate at 120ºC for 30 minutes before deposition. The sputtering was performed in argon atmosphere at room temperature. The flow rate of the Ar gas was set to 15 sccm, the DC power was 100 W, and the chamber pressure was down to $5x10^{-3}$ Torr. Here the thin film of Cr was 10 nm as the adhesive layer and Au was 100 nm as the lower electrode. For the ZnO nanowire growth, the substrate with the electrode was first cleaned thoroughly in acetone and ethanol sonication for 10 minutes respectively and blown dry using the flowing nitrogen gas. Then, the substrate was wet with a droplet of 5mM zinc acetate dehydrate (98%, Aldrich) in ethanol, rinsed with clean ethanol after 10 seconds, and then blown dry with a stream of nitrogen. This coating step was repeated three times. The substrate with a film of zinc acetate crystallites was heated to 350℃ in a muffle oven for 20 min to yield layers of ZnO islands with their (0001) planes parallel to the substrate surface. The zinc acetate deposition and decomposition procedure was carried out twice to ensure a complete and uniform coverage of ZnO seeds on the substrate with enough gaps among those crystalline inlands. The hydrothermal reaction solution for ZnO nanowire arrays growth was prepared by mixing 25mM zinc nitrate hydrate ,25mM hexamethylenetetramine solution, and 6mM polyethylenimine (branched, 600 molecular weight, Aldrich) in a bottle with an autoclavable screw cap. The seeded substrate was immersed vertically in the solution, and the sealed bottle was heated to 90ºC for 3h inside a conventional laboratory oven. Because nanowire growth slowed after this period, substrates were repeated introduced to fresh solution baths in order to obtain desired length of nanowire arrays. The arrays were then rinsed with deionized water and annealed in a

muffle furnace at 400ºC for 30 minutes to remove any residual organics and to optimize the nanowires performance.

The polymer used as a matrix was low stress commercial polyimide PI-2611 bought from HD Microsystems Inc. Since the pure polyimide was too thick to completely cast into the ZnO nanowires layer as shown in figure 5.2(a), it was first diluted by the solvent T9039 (HD Microsystems Inc.). The mixed solution was prepared by homogenizing for 1 hour (350 rpm with a 6 mm diameter rotor) and stood at room temperature overnight for stabilization of the solution. The homogenous solution was dropped onto the surface of the substrate covered by ZnO nanowires layer, then the sample was placed into the vacuum oven (Isotemp 282A) and held under vacuum for one minute to allow all bubbles to dissipate out solution. After that, the sample was taken out and kept in the normal pressure for 30 minutes to make sure the polyimide flow in the nanowires layer as far as possible and relax. Two steps of spin coating process were employed in the deposition using G3P-8 specialty coating system (Cookson Electronics Inc.): the first run was 500 rpm for 5 seconds to make the polyimide to gradually cover the substrate and the second run was a high speed 2000 rpm for 30 seconds according to the desired thickness of films. A soft-bake was done on the hot plate at 120 ºC for 2 minutes after coating. Subsequently, the soft-baked films were cured at 350 ºC for 30 minutes in the muffle oven to convert the polyamic acid into a fully aromatic, insoluble polyimide to obtain the solvent-free ZnO-polyimide nanocomposite.

Dispersion of ZnO nanowires into the polymer matrix was assessed via scanning electron microscopy. Figure 5.2 shows the morphology of polyimide-ZnO nanowire nanocomposites with different weight ratio of polyimide PI-2611 and solvent T9039. The concentration of polyimide is important for the final incorporation between ZnO nanowires and the polyimide. We found

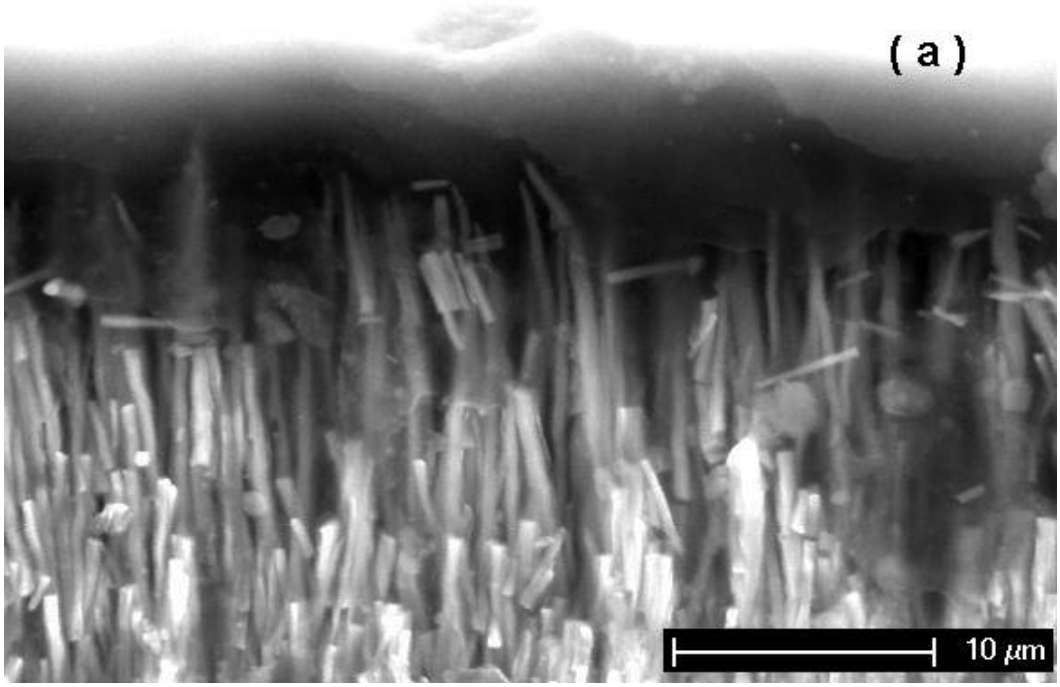
( a )
10 μm

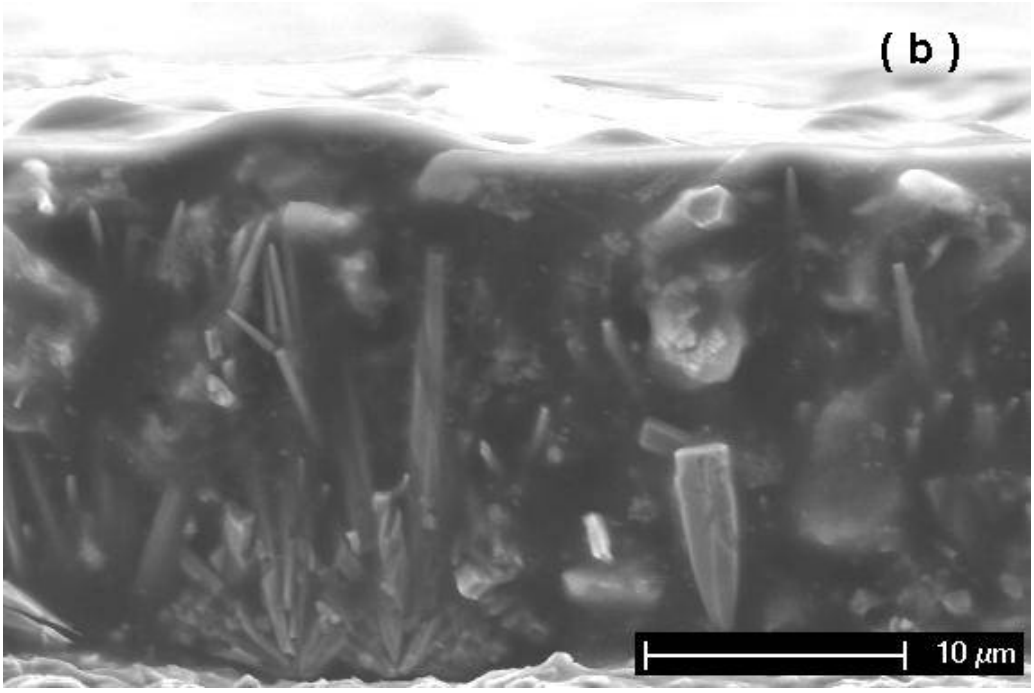
( b )
10 μm

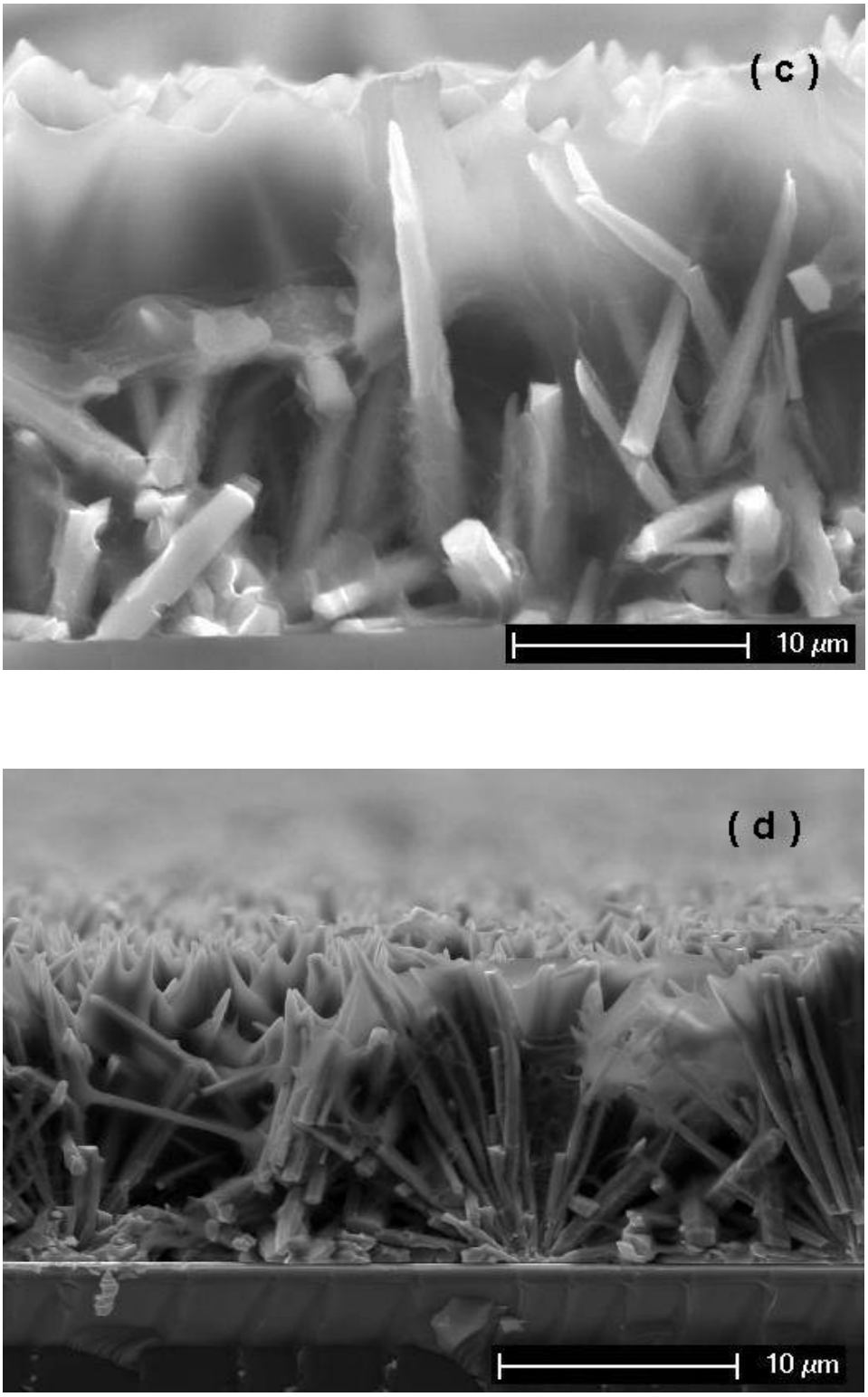


**Figure 5.2.** SEM images of nanocomposites with ZnO grown for 30 hours and different wt% of PI2611 and T9039. (a) pure, (b) 1:0.5, (c) 1:1, (d) 1:2.

that the pure polyimide was difficult to completely spin into the internal space of the nanostructure due to the high solution viscosity and large surface stress of nanowires shown in figure 5.2(a). So a kind of solvent T-9039 was used to dilute the polyimide first to reduce the viscosity. Here three different mixtures of weight ratio 1:0.5, 1:1, and 1:2 were investigated. For weight ratio 1:0.5, it was found that the ZnO nanowires were highly covered by the polyimide without obvious voids, but the top surface of the composite was not flat and smooth due to some bumps as shown in figure 5.2(b). Figure 5.2(c) shows the nanocomposite with weight ratio 1:1. The solution could be easier to flow down to the bottom of the nanowires layer due to higher mobility. But the incorporation between ZnO nanowires and the polyimide seemed weak after curing. There were some small voids in the composite and a lot of concavities on the top surface because there was not enough polyimide to fill into the space owing to the dilution. When the polyimide was further diluted to weight ratio 1:2 as shown in figure 5.2(d), the voids in the composite and the concavity on the surface became more severe. Based on above discussion, the weight ratio around 1:0.5 seems to be the best choice which can give us good dispersion of ZnO nanowires in the polyimide, meanwhile balance the top surface roughness of the nanocomposite film.

During the nanocomposite fabricating procedure, the polymerization is also highly affected by the dimensions of ZnO nanowires themselves. Figure 5.3 shows the morphology of nanocomposites with different growing time of ZnO nanowires. According to a two-step hydrothermal method, it has been observed that the longer the growing time the higher the height of ZnO nanowires. However, we found that it was negative for the final dispersion of nanowires in the polyimde matrix if ZnO nanowires were too long, such as shown in figure 5.3(c). As the nanowires grew from the seed layer and the diameter increased as increment of growing time, the

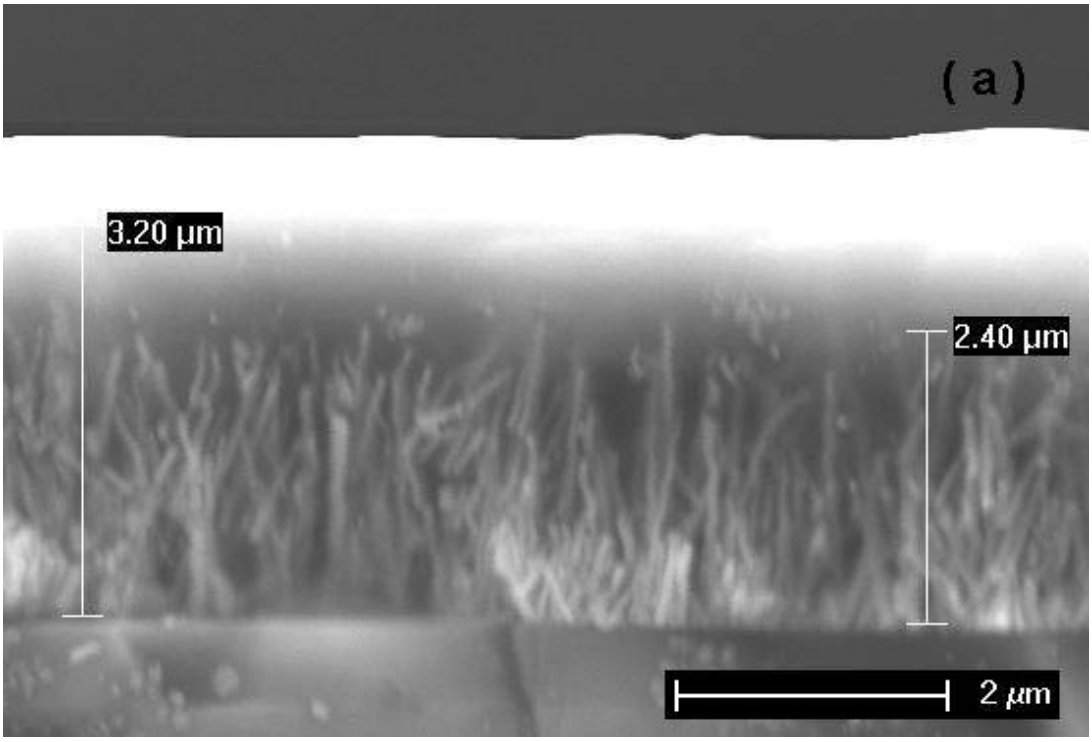
( a )
3.20 µm
2.40 µm
2 µm

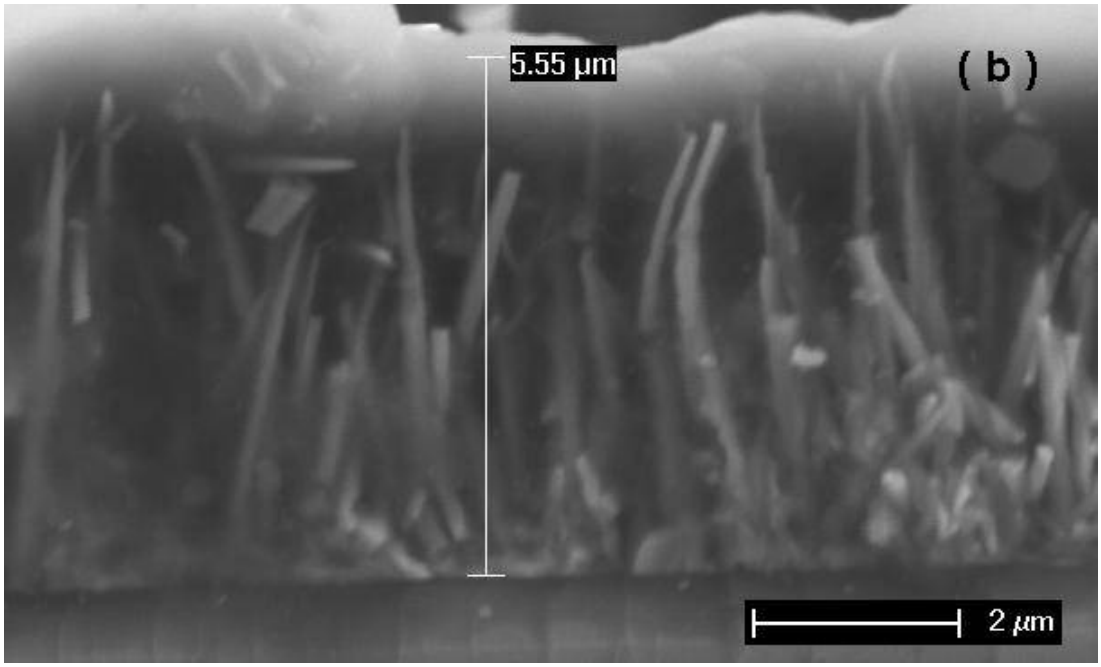
5.55 µm
( b )
2 µm

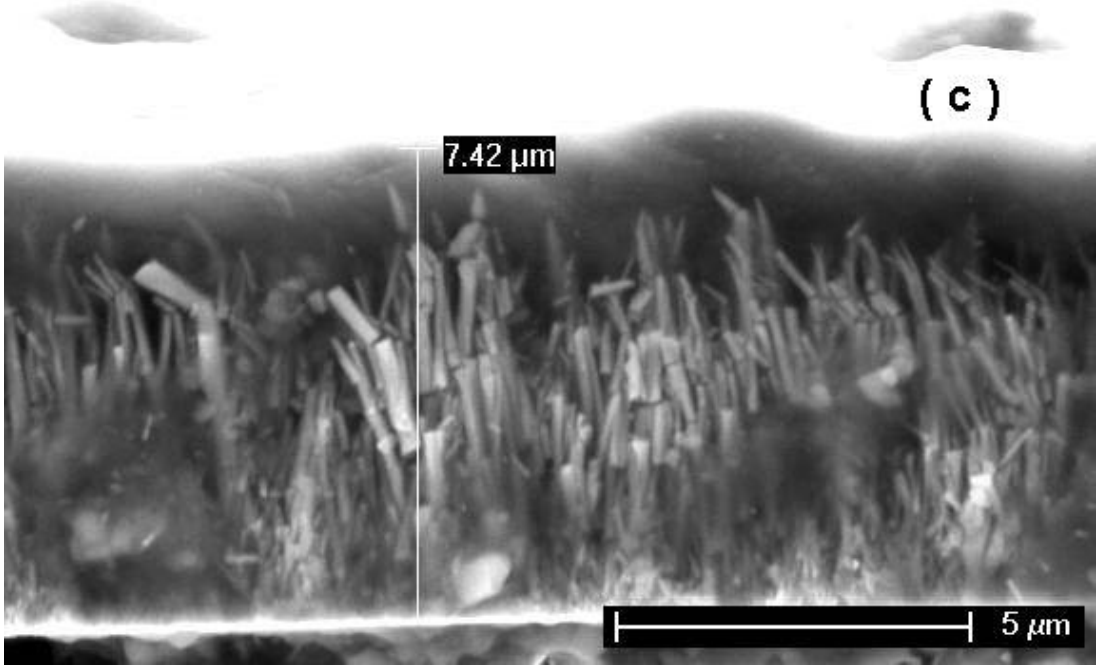


**Figure 5.3.** SEM images of nanocomposites using 1:0.5 wt% of PI2611 and T9039 and with different growing time of ZnO nanowires. (a) 8 hours, (b) 16 hours, (c) 24 hours.

lower parts of nanowires became much closer, even contacted together. So it was very difficult for polyimide to free cast into the bottom of the nanowire layer and a nearly pure ZnO layer appeared in the lower part of the nanocomposite film, which conflicted with the original design to get a kind of polymer-base composite with uniform dispersion of ZnO nanowires. The top surface was also obviously influenced by the longer nanowires and there were some pin holes. Meanwhile, some voids were seen from the cross-section of the composite because there was not enough polyimide to fill in the large internal space among nanowires. The discovery in figure 5.3(C) drove us have to think shorter ZnO nanowires. When we reduced the growing time of ZnO nanowires from 24 hours shown in figure 5.3(c) to 16 hours shown in figure 5.3(b), the length of ZnO nanowires was getting shorter and the internal space of the lower part of

nanowires layer also became larger, which was more convenient for polyimide casting. Although voids in the upper part of the composite film were reduced compared to figure 5.3(c), the top covered polyimide was thin, which caused the surface was not flat due to the effect of below ZnO nanowires. When we further reduced the growing time of ZnO nanowires to 8 hours, the homogenous dispersion of ZnO nanowires in a polymer matrix was achieved as shown in figure 5.3(a). The thickness of nanocomposite film was 3.2 um with a flat top surface.

The surface roughness of the ZnO-polyimide nanocomposite was evaluated by Scanning Probe Microscope (SPM) (Veeco, Dimension V). SPM is a branch of microscopy that produces high-resolution, three-dimensional images by scanning a sharp tip over the specimen surface. The tip is part of a flexible cantilever mounted on one end of a cylindrical piezoelectric tube mounted near the top of the microscope. Voltages applied to the X and Y electrodes on the piezoelectric tube deflect the tube horizontally to produce a precise raster scan over the sample surface. A voltage applied to the Z electrode on the piezoelectric tube controls the vertical height of the tip. An image of the surface is obtained by mechanically moving the probe in a raster scan of the specimen, line by line. Forces between the tip and the sample surface cause the cantilever to bend or deform and the laser beam coupled with the cantilever is reflected and detected by photo detector. Finally the laser beam signal change can be converted into height variation of the sample surface and thus the morphology of the film can be obtained. Figure 5.4 shows scanning results. ZnO nanowires in the nanocomposite film were grown for 8 hours and the used polyimide was diluted by the solvent T9039 with weight ratio 1:0.5. The surface of the nanacomposite film is quite smooth and the variation of the height is less than 100 nm.

In summary, the thin film nanocomposite with uniformly dispersed ZnO nanowires in the polyimide matrix was achieved using the self-alignment method. This fabrication process

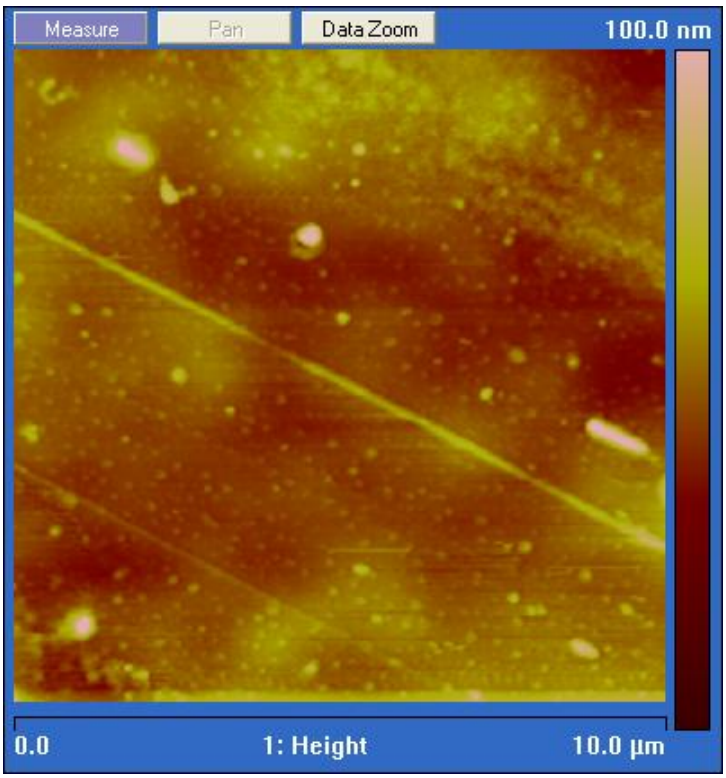


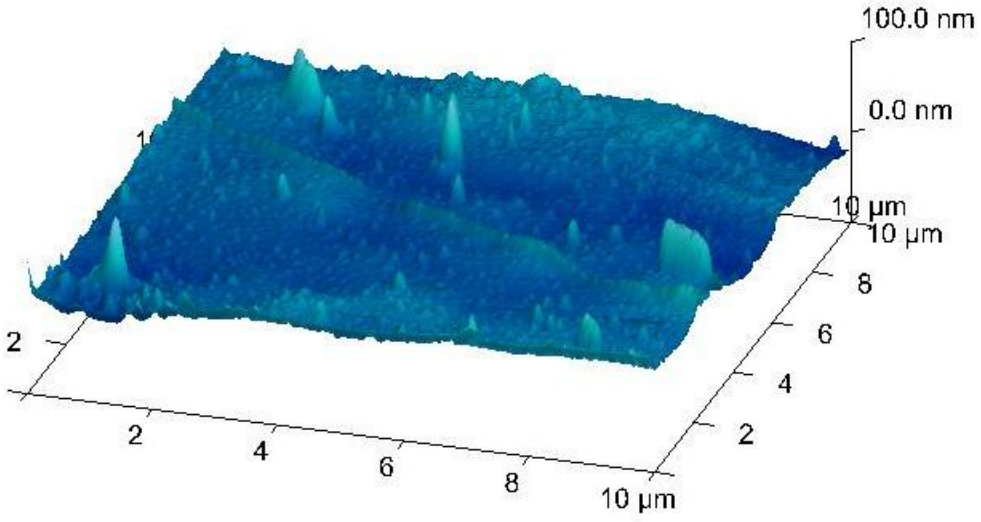


**Figure 5.4.** SPM images of top surface of the nanocomposite film with ZnO grown for 8 hours and polyimide solution diluted with wt% 1:0.5. Top: 2-D scanning picture, Bottom: 3-D contour of top surface.

included the controlled growth of ZnO nanowires on the substrate and the polymer spin-coating. The results of sample analyses indicated that the morphologies of the designed nanocomposites were significantly influenced by the viscosity of the polymer and the geometrical structure of ZnO nanowires. The optimum parameters of composite preparation were obtained. For the final sample, a diluted polyimide by solvent T9039 with weight ratio 1:0.5 was used, and the inclusion of ZnO nanowires was grown for 8 hours with the length of 2.4um.

### 5.2.2 External Electric Field Assisted Alignment Method

The term dielectrophoresis (DEP) was first used by Pohl [75] to describe the translational motion of neutral matter caused by polarization effects in a nonuniform electric field. In a nonuniform electric field, the neutral particle will find a translantional force upon it. This occurs because under the influence of the nonuniform field it acquires a polarization that has the effect of putting a negative charge upon the side nearer the positive electrode, and a positive one on the side nearer the negative electrode. Because the particle is neutral, the two charges on the body are in fact equal. But the fields operating on the two regions are unequal. This gives rise to a net force. The usual result of such a polarization of a neutral body in a nonuniform field is to bring about a force impelling the neutral body toward the region of stronger field. For a discrete, electrically neutral particle surrounded by suspending medium and subjected to a two-pole, spatially inhomogeneous electric field, it is sufficient to consider only the dipole derived polarization force. In figure 5.5 [76], a pin-plate electrode configuration is shown to create a spatially inhomogeneous electric field $E$. The effective dipole moment $m_1$ and $m_2$ induced in the particle are represented by the equal and opposite charge distribution $\delta^+$ and $\delta^-$ at the particle boundaries. Note that the magnitude of the cumulative charge on each side of the particle is

equal ($\delta^+ = -\delta^-$), and that the net charge on each particle is zero. However, because the applied electric field is inhomogeneous, the local electric field is different on the opposite sides of each particle, and a net translational force acts on the particles. This is the dielectrophoretic force $F_{DEP}$ as described by Pohl. The direction of the DEP force depends on the orientation of the induced dipole with respect to the field direction. For particle that are more polarizable than their suspending medium, the induced dipole moment vector is in the same direction (collinear) as the field vector, and a positive dielectrophoretic force directs the particles toward regions of strong electric field gradient (figure 5.5a). For particles that are less polarizable than their suspending medium, the induced dipole vector is in the opposite direction (antiparallel) of the field vector, and a negative dielectrophoretic force directs the particles toward regions of weak electric field gradient (figure 5.5b). Also note that if the dipole moment of the particle is not oriented parallel to the direction of the electric field, a net torque will act on the particle.

Recently, dielectrophoresis, due to simple operation and high efficiency, has been widely used for manipulating and aligning nanoparticles [77], carbon nanotubes [78], metallic nanowires [79], and semiconductor nanowires [80]. It was reported that the density and orientation of one dimensional nanostructure strongly depended on the magnitude and the frequency of the electric field. In this project, we used the external electric field to generate dielectrophoresis to assemble and align ZnO nanowires across metal electrodes in the polyimide matrix, and further fabricate the designed nanocomposites.

ZnO nanowires used in this work were synthesized through the same way: two-step hydrothermal method as before [68]. ZnO nanowires were grown on the glass substrates, and subsequently those substrates were sonicated in ethanol for 2 hours to shake off nanowires from the substrates into the solution. After that, ethanol was vaporized on the hot plate and white

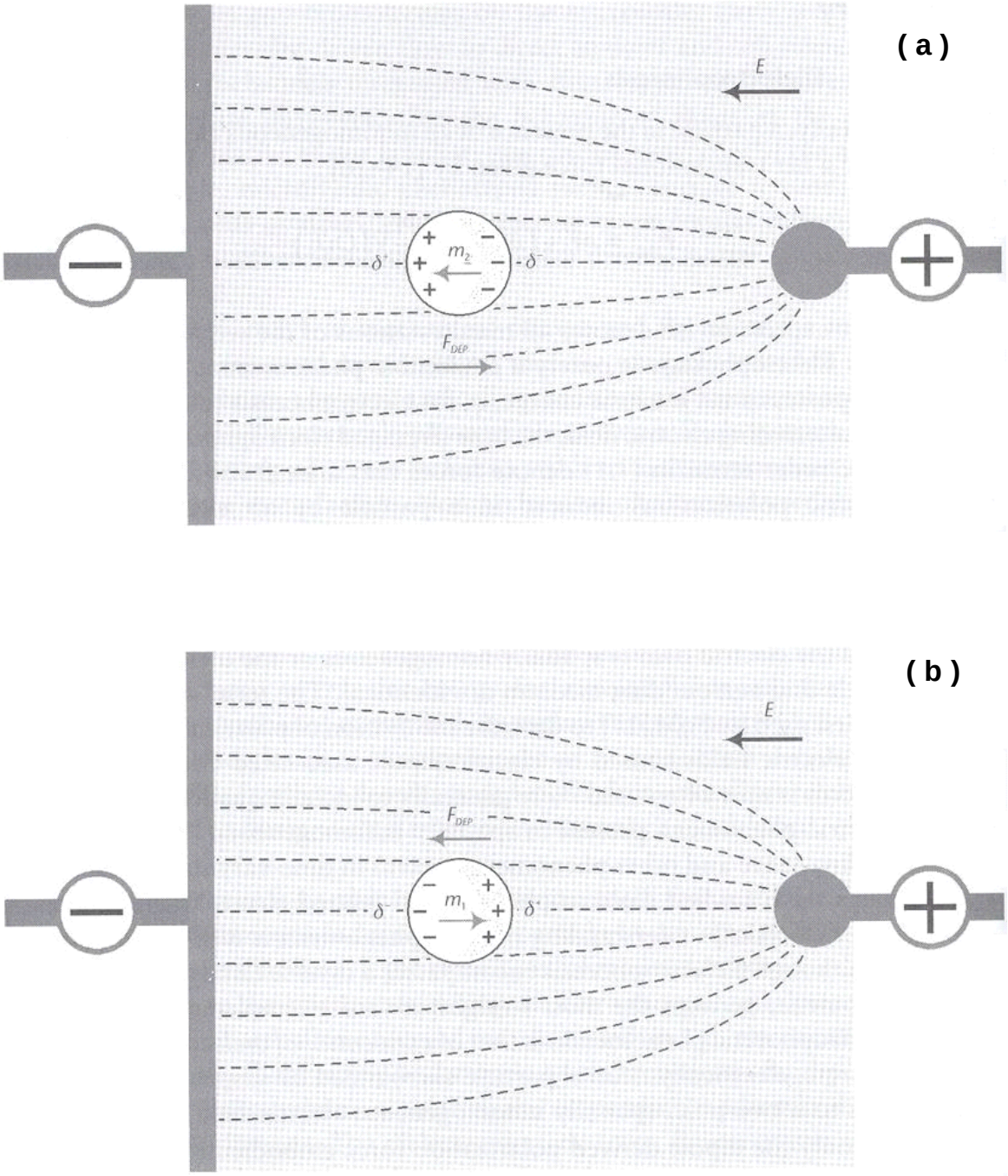


**Figure 5.5.** (a) Positive dieletrophoresis and (b) negative dielectrophoresis [76].

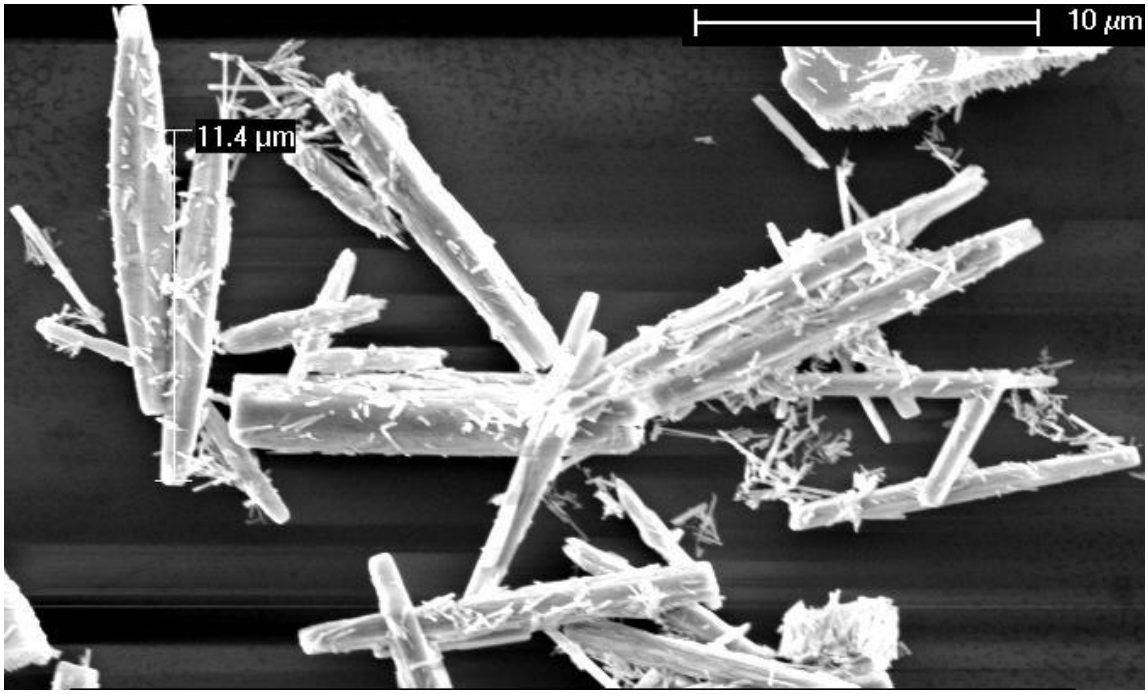


**Figure 5.6.** SEM image of ZnO nanowires for electric field assisted alignment

residuals were collected on the bottom of the beaker. They were pure, structurally uniform, single crystalline. And the length was about 11 μm as shown in figure 5.6.

External electric field assisted alignment of the ZnO nanowires was studied using interdigitated (IDT) electrodes schematically shown in figure 5.7. The fabrication process, depicted in figure 5.8, started from a clean 3 inch glass wafer. A 100 nm Au film was sputtered on the glass substrate with a 10 nm Cr film as the adhesive layer between Au and glass using AJA ATC 1300F custom magnetron sputter system same as mentioned before. The photoresist AZ4210 was then spin coated on the substrate by the Karl Suss RC8 spinner (SUSS MicroTec Inc., USA), followed by a soft bake at 95 °C for 5 min to evaporate the solvent and densify the film on a level hot plate. After the photoresist was exposed by UV light and developed, a wet etch step using Au and Cr etchant was performed. The wafer was then rinsed using acetone and deionized water, and subsequently dried with a gentle stream of nitrogen gas. After those steps,

arrays of interdigitated electrodes have been fabricated on the substrate with the geometries defined by the mask, where the finger width and gap was 40 and 40 μm, respectively.

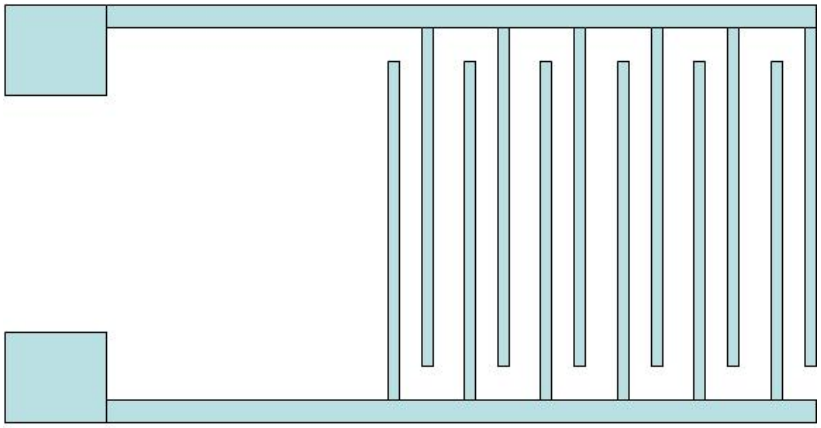

**Figure 5.7.** Schematic of interdigitated electrodes

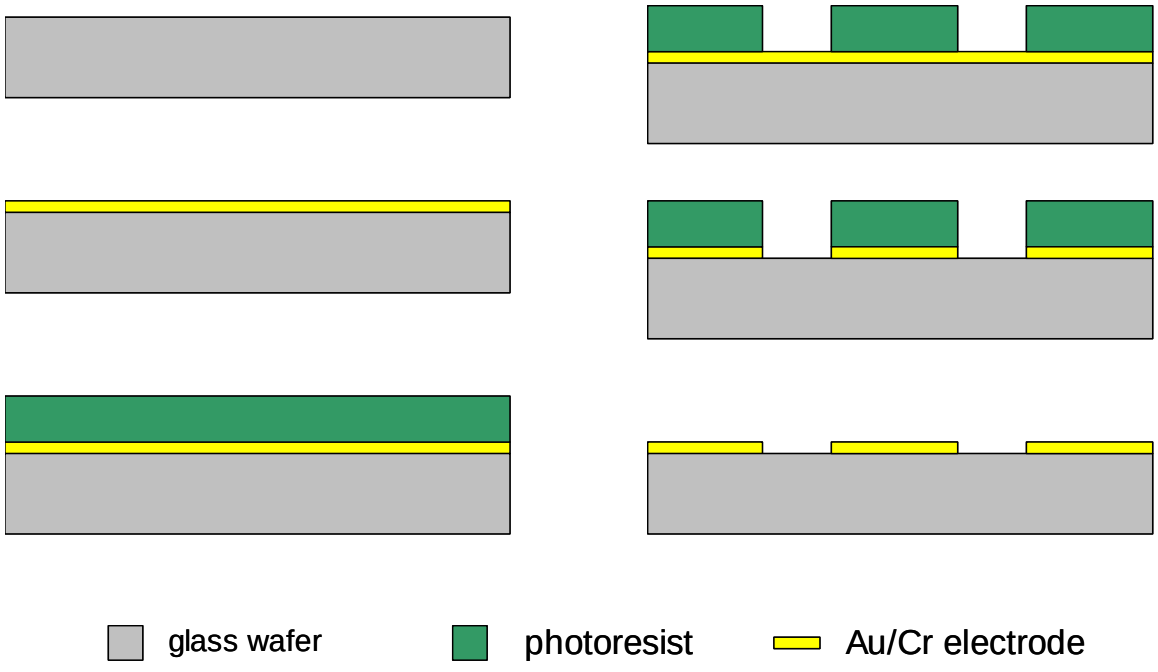


**Figure 5.8.** Fabrication process of interdigitated electrodes

The polymer used as a matrix was polyimide PI-2611 and the solvent used to dilute polyimide was T9039. Both were purchased from HD MicroSystems. Since the pure polyimide had much high viscosity, it was first diluted by the solvent T9039 according to weight ratio. The mixed solution was prepared same as before. It was stirred for 1 hour (350 rpm with a 6 mm diameter rotor) and stood at room temperature overnight for stabilization of the solution. The as-synthesized ZnO nanowires were dispersed into the polyimide solution according to weight ratio, and was stirred for 10 min (400 rpm with a 6 mm diameter rotor) and then sonicated for half an hour in an ultrasonic bath. Subsequently, the ZnO nanowires suspension was spin coated onto the interdigitated electrode using G3P-8 specialty coating system (Cookson Electronics Inc.). There were two steps in the spin-coating process: the first step was 500 rpm for 5 seconds to make the polyimide to gradually cover the substrate and the second step was a high speed 2000 rpm for 30 seconds in term of the desired thickness of films. Alignment experiments were conducted by applying an alternating current (AC) electric field (alternating voltage $V_{ac}$ peak to peak) with a direct current (DC) offset voltage ($V_{dc}$) to the electrodes for 10 minutes. The circuit is schematically shown in figure 5.9. Electrodes were wired to the function generator (Model DS345, Standard Rearch System) through a power amplifier (AVC 790, PCB Piezotronics Inc.). After the alignment, the sample was performed a soft bake on the hot plate at 120ºC for 2 minutes. Subsequently, the soft-baked films were cured at 350ºC for 30 minutes in the muffle oven to convert the polyamic acid into a fully aromatic, insoluble polyimide to obtain the solvent-free ZnO-polyimide nanocomposite.

Optical microscope and scanning electron microscope (SEM) were utilized to characterize the dispersion of the ZnO nanowires in the polymer matrix. It was observed that the surface morphology of the nanocomposite thin film was affected by the concentration of the polyimide

solution. If we used too much solvent T9030 to dilute polyimide PI2611 as shown in bottom SEM image of figure 5.10, the surface roughness became worse because there were not enough polyimide left after curing to cover ZnO nanowires. So the mixed solution with weight ratio 1:1 was used to achieve desired surface morphology of the nanocomposite film (top SEM image of figure 5.10).

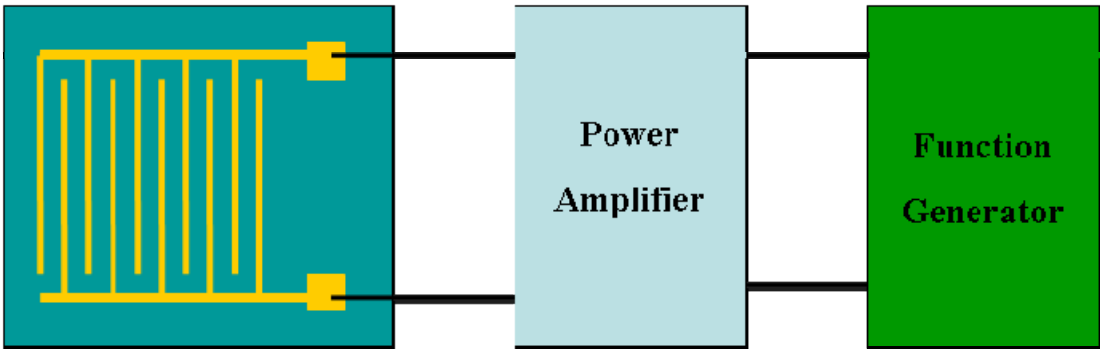


**Figure 5.9.** Schematic drawing of the wiring scheme (not to scale)

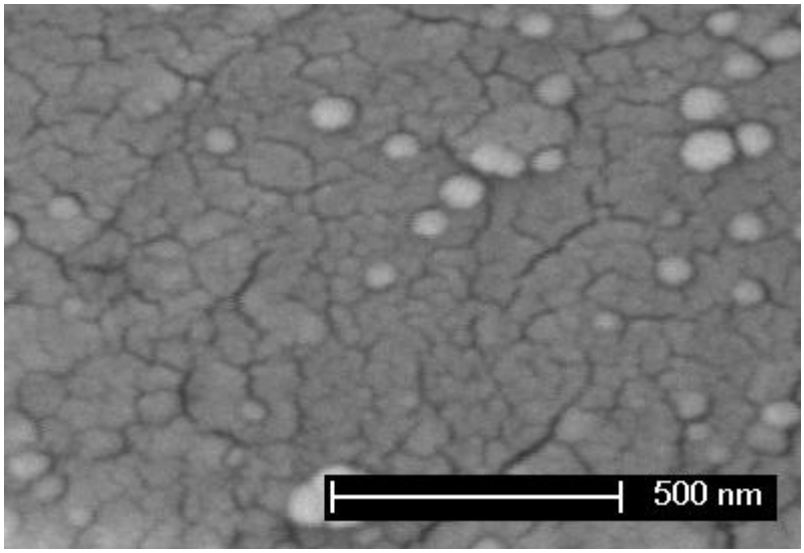

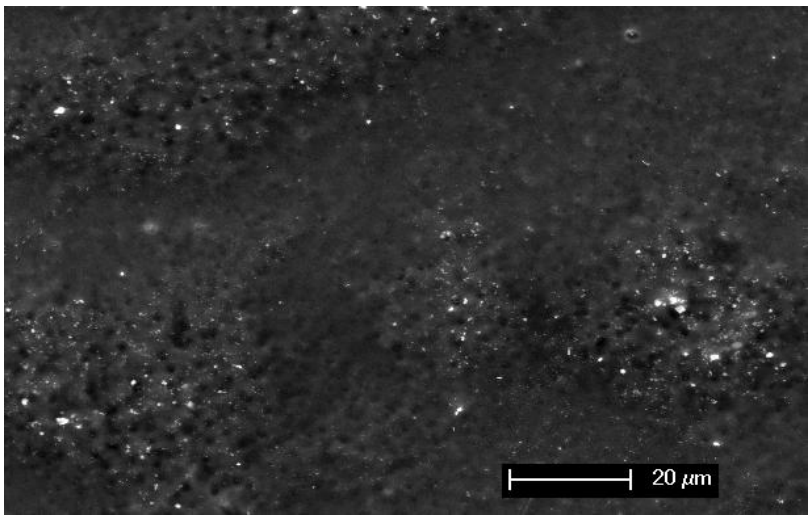


**Figure 5.10.** SEM images of nanocomposites with different PI2611 and T3090 weight ratio. Top 1:1, Bottom 1:4.

Figure 5.11 shows the optical image of ZnO nanowires alignment assisted by applying 10v peak to peak AC voltages with 10v DC offset voltage under different frequencies of 100, 1000, and 10000 Hz. For the frequency of 100Hz, most of nnaowires random dispersed between the electrodes or on the electrode, only some of them were horizontally aligned in the electric field as shown in figure 5.11(a). When the frequency increased to 1000 Hz in figure 5.11(b), almost all ZnO nanowires were attracted to stick on the edge of electrodes and uniformly deposited along the direction of the electric flux. As the frequency further increased to 10000Hz shown in figure 5.11(c), ZnO nanowires again became random dispersion across the whole electric field, only a few remained horizontal at the edge of the electrodes. The result in figure 5.11 indicates that the degree of alignment of ZnO nanowires has a strong correlation with the frequency of the alternate current electric field, and there is a resonant frequency around 1000 Hz, under which ZnO nanowires could be well distributed in the polymer matrix.

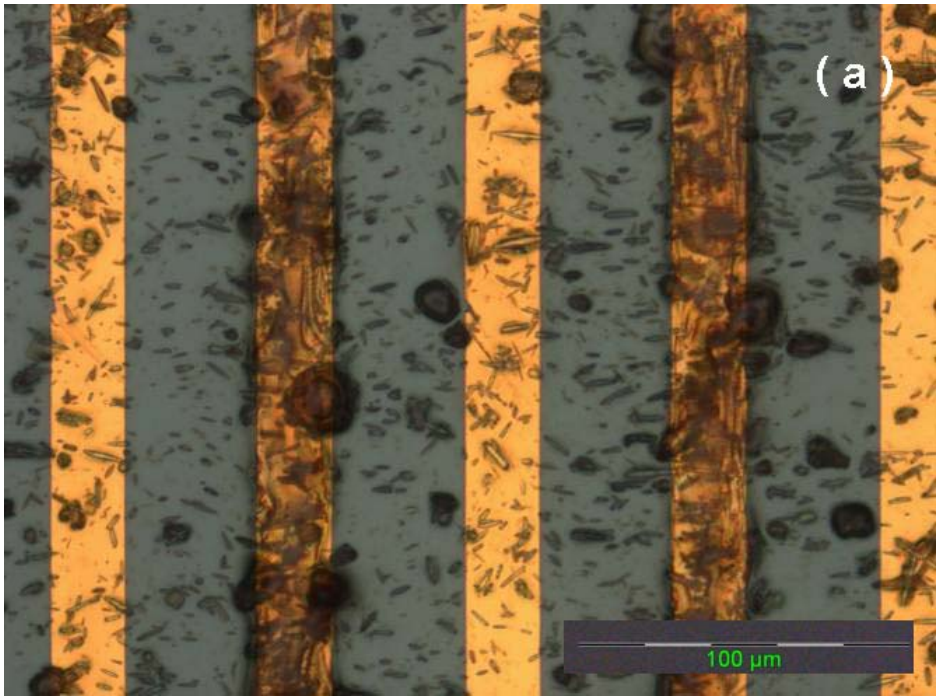
( a )
100 µm

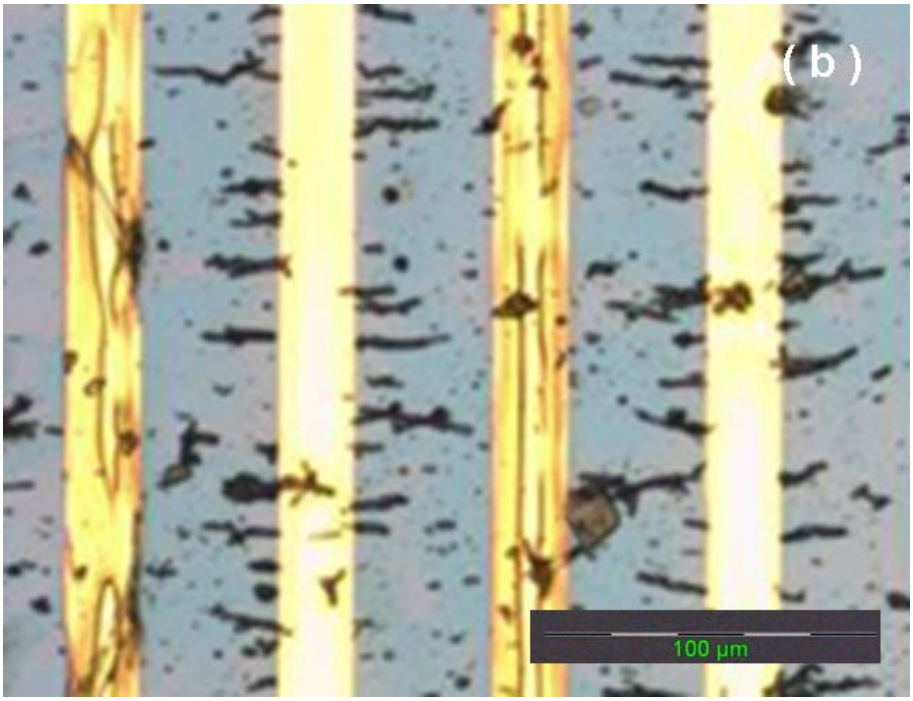
( b )
100 µm

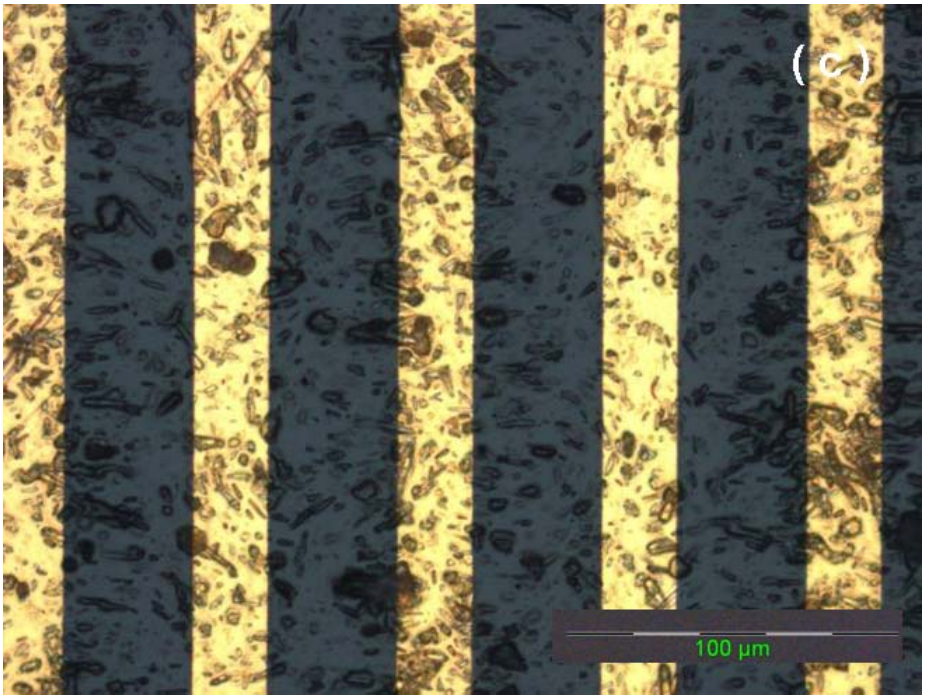


**Figure 5.11. O**ptical images of ZnO nanowires aligned by applying 10v peak to peak AC voltages with 10v DC offset voltage under different frequencies. (a) 100 Hz, (b) 1000 Hz, (c) 10000Hz.

The effect of magnitude of AC voltage on ZnO alignment was also studied. Figure 5.12 illustrates the optical image of the samples aligned by the electric field with different magnitudes. Here the used electric field has magnitudes of 2v, 10v, 20v AC voltage and 10v DC offset voltage and frequency of 1000Hz. For an AC voltage of 2v, ordered ZnO nanowires were deposited across the gap with a large spacing as shown in figure 5.12(a). When the AC voltage was 10v, more nanowires were aligned in the electric field and the average spacing between ZnO nanowires became smaller (figure 5.12b). When the AC voltage increased to 20v, the concentration of aligned ZnO nanowires was getting even higher (figure 5.12c). The images of optical microscope demonstrate that the number of aligned nanowires across the electrodes increased with increase in the applied ac electric field strength. These results imply that the

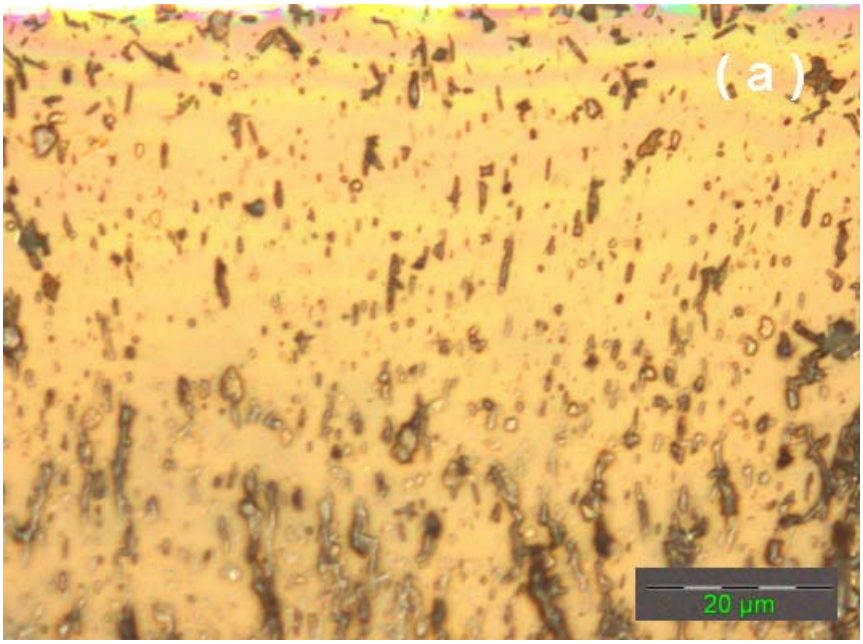
( a )
20 µm

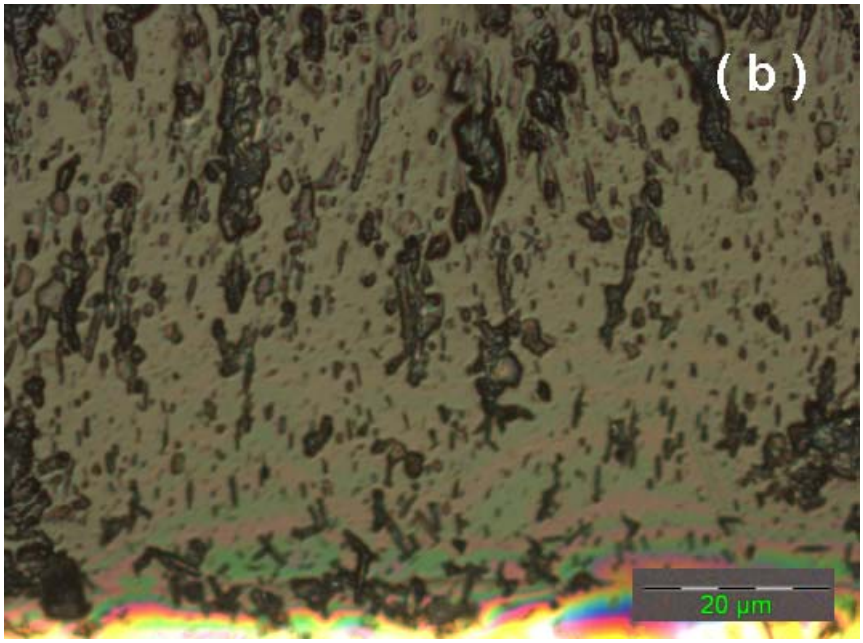
( b )
20 µm

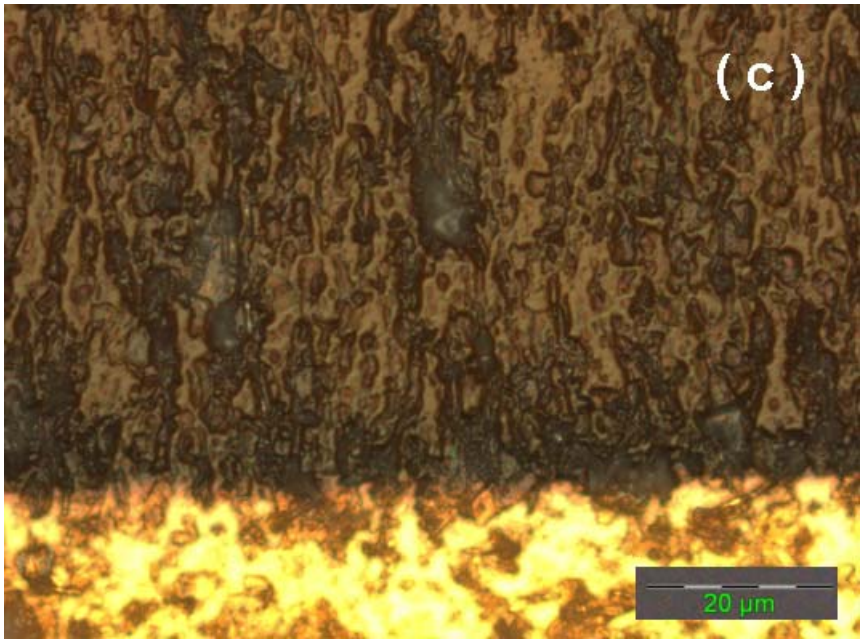


**Figure 5.12. O**ptical images of ZnO nanowires aligned by different AC voltages peak to peak with a frequency of 1000 Hz and a DC offset voltage of 10v. (a) AC 2v, (b) 10v, (c) 20v.

number of ordered ZnO nanowires in the gap can be easily controlled by the ac potential and will be proportional to the magnitude of the AC electric field.

The assembly was further extended to investigate the effect of the DC offset voltage on the deposition position of ZnO nanowires. Different DC offset voltage of 0v, 1v, 2v, 10v were applied to the electric field with 10v AC peak to peak voltage and frequency of 1000Hz. The experimental results are shown in figure 5.13. A remarkable effect of DC offset voltage on the deposition position of the nanowires was observed. When a pure AC electric field was applied, the nanowires were almost all deposited at the edge of the electrode finger, many areas in the gap did not have any nanowire, and the top surfaces of electrodes were nearly clean (figure 5.13a). When the voltage increased to 1v, the site of the nanowires assembly moved to the center of the gap, and some started to appear on the surface of the electrode finger as shown in figure 5.13(b).

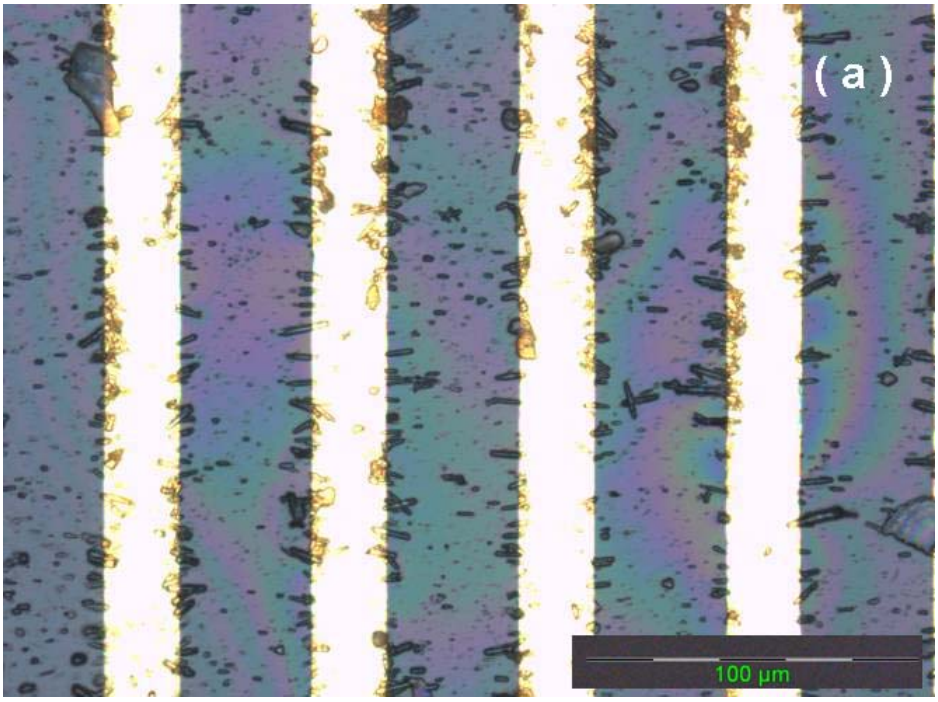
( a )
100 µm

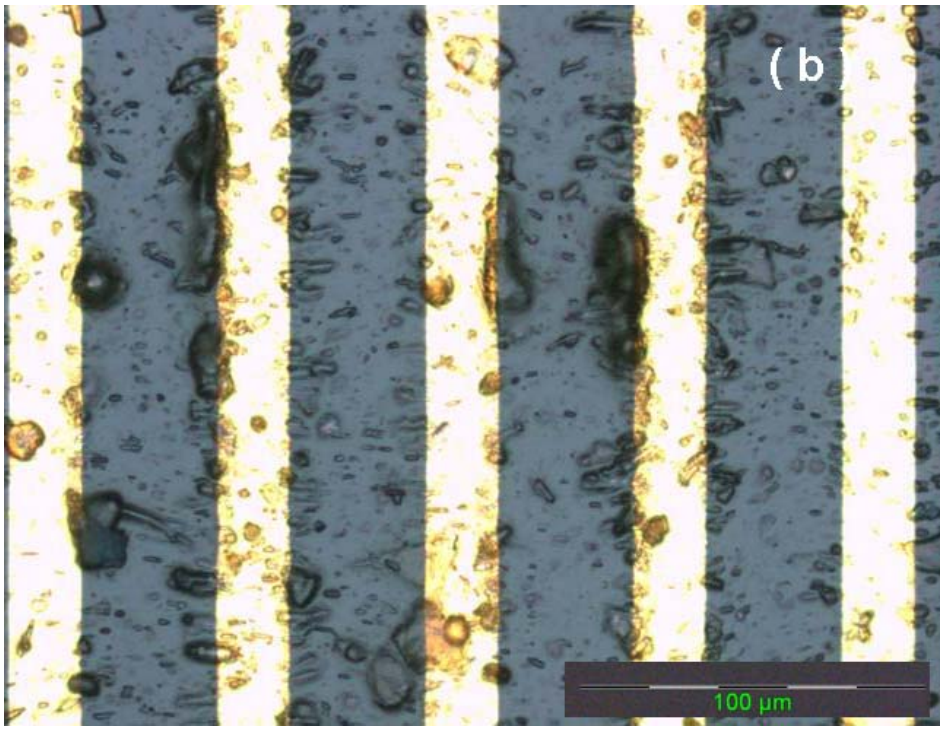
( b )
100 µm

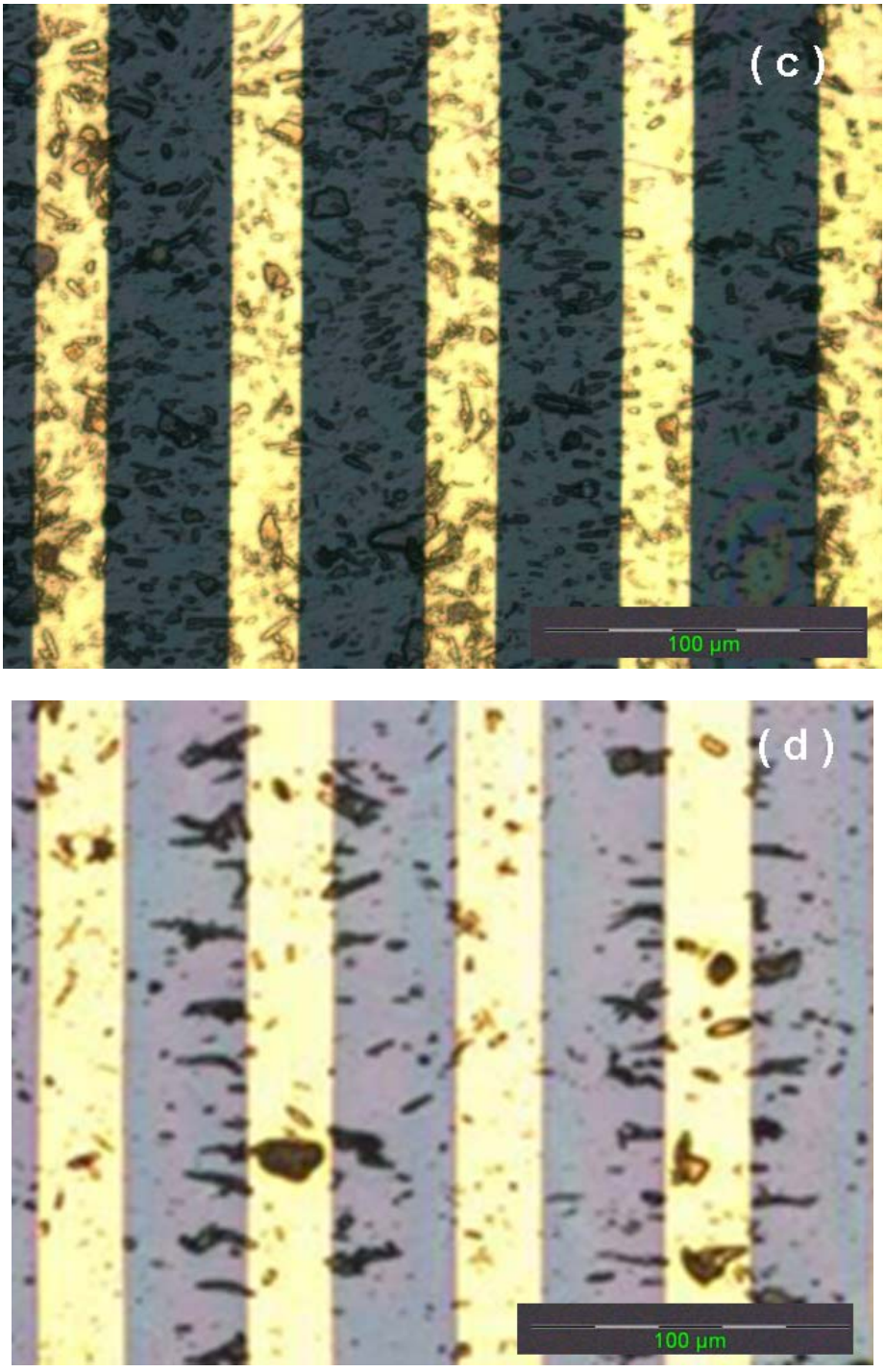


**Figure 5.13. O**ptical images of ZnO nanowires aligned by 10v AC voltages peak to peak and a frequency of 1000 Hz and different DC offset voltage. (a) 0v, (b) 1v, (c) 2v, (d) 10v.

When the DC voltage further increased to 2v, the nanowires were uniformly distributed in the gap and more of them also were deposited on the electrode (figure 5.13c). For the DC voltage of 10v in figure 5.13d, most of nanowires were attracted on the edge of the positive electrode and a few nanowires were combined together to form a large nanowire bundle. Meanwhile, some nanowires became big agglomeration on the electrode. However, for the ground electrode of DC electric field, almost no nanowires were found at the edge. The results in figure 5.13 demonstrate that the DC offset voltage has a strong effect on the deposition site of ZnO nanowires. Smaller or larger DC voltage both will affect the uniformity of nanowires alignment and attract most of nanowires on the edge of the electrode. Only proper selection such as 2v can get uniform distribution of ZnO nanowires across the whole electrode area.

The above aligned pattern of ZnO nanowires can be interpreted as being the result of a dielectrophoretic force. When an external electric field is applied to the electrode, the electric polarization is induced in the ZnO nanowires. Because of the structure anisotropy of the ZnO nanowires, the dipole moment in the direction parallel to the nanowire axis is quite stronger than that in the perpendicular direction. Therefore, ZnO nanowires could be aligned along the direction of the electric field if the dielectrophoretic force could overcome the restriction of the polymer medium. A dielectrophoretic force on a nanowire, induced by polarization in a nonuniform oscillating electric field, is related to the geometry of the nanowire, its material properties, and the spatial distribution of the ac electric field. The dielectrophoretic force can be written as [81]

$$F_{DEP} = \frac{1}{4} v \,\mathrm{Re}\left[\frac{\varepsilon_p - \varepsilon_m}{\varepsilon_p + 2\varepsilon_m}\right] \nabla |E|^2 \qquad (1)$$

$$E = E_{AC} + E_{DC} \qquad (2)$$

where $E_{AC}$ is the electric field generated by the AC voltage between the electrode finger, $E_{DC}$ is the electric field generated by the DC offset voltage, $v$ is the dimensional constant of the ZnO nanowire, and $\varepsilon_m$ and $\varepsilon_p$ are the permeability of the medium(polyimide solution) and nanowire, respectively. The induced force is proportional to both a polarized dimension of nanowires and the gradient of the electric field square. The dielectrophoretic force is also dependent on the complex, frequency-dependent permittivity. Here, the AC frequency, the electric field distribution, the DC offset voltage, and the electrode shape were used to control the deposition pattern. In the case of the interdigitated electrodes as shown figure 5.7, the ac electric field gradient is almost negligible (i.e. $\nabla E^2 \cong 0$ ) along the vertical direction and so the dielectrophoretic force in this direction is close to zero. In contrast, the electric field rapidly changes in the horizontal direction, across the electrodes. The field changes particularly abruptly near the electrode edges. Therefore, it was observed in figure 5.12 that the higher ac electric field increased the alignment yield by forcing the alignment of the ZnO nanowires in the horizontal direction of the electrode gap because the dielectrophoretic force is proportional to the gradient of the electric field square. When the DC offset voltage varies, the electric field $E_{DC}$ will change accordingly, which consequently leads to the change of the electric field distribution in the polyimide solution and moves the deposition site of the nanowires as shown in figure 5.13. As we know that the permeability of the polyimide medium and the nanowires are determined by the applied frequency, thus there is a strong correlation between the dielectrophoretic force and the frequency of the ac electric field in term of equation (1). As shown in figure 5.11, the degree of the alignment of nanowires is depending on the frequency and there is a resonant frequency under which the horizontal orientation of most ZnO nanowires can be achieved.

We also studied ZnO nanowires concentration in the polymer solution to determine its effect on nanowires assembly. Here two different ZnO nanowires weight ratios were used. Figure 5.14 shows the optical images of fabricated nanocomposites. For 10 wt% ZnO nanowires, it was seen that a few nanowires congregated during the alignment and affected the nanowires uniform distribution in the polymer as shown in figure 5.14(a). As the weight ratio decreased to 5%, the dispersion of ZnO nanowires in the nanocomposite became much better (figure 5.14b).

In summary, the nanocomposite with controlled alignment of ZnO nanowires in the polyimide matrix was achieved using electric field assisted method. Highly oriented ZnO nanowires were dispersed in the polymer by applying an AC electric field with a DC offset voltage. The experimental results showed that the density and the alignment degree of ordered ZnO nanowires significantly depended on the magnitude and the frequency of the applied ac electric field. The DC offset voltage had strong effect on the deposition sites of nanowires. In addition, the optimal parameters, such as polyimide PI2611 and solvent T9039 weight ratio, ZnO nanowires weight ratio, also have been investigated. Because this method is fast and efficient, the electric assisted assembly will be an important technique for the aligned ZnO nanowire nanocomposite.

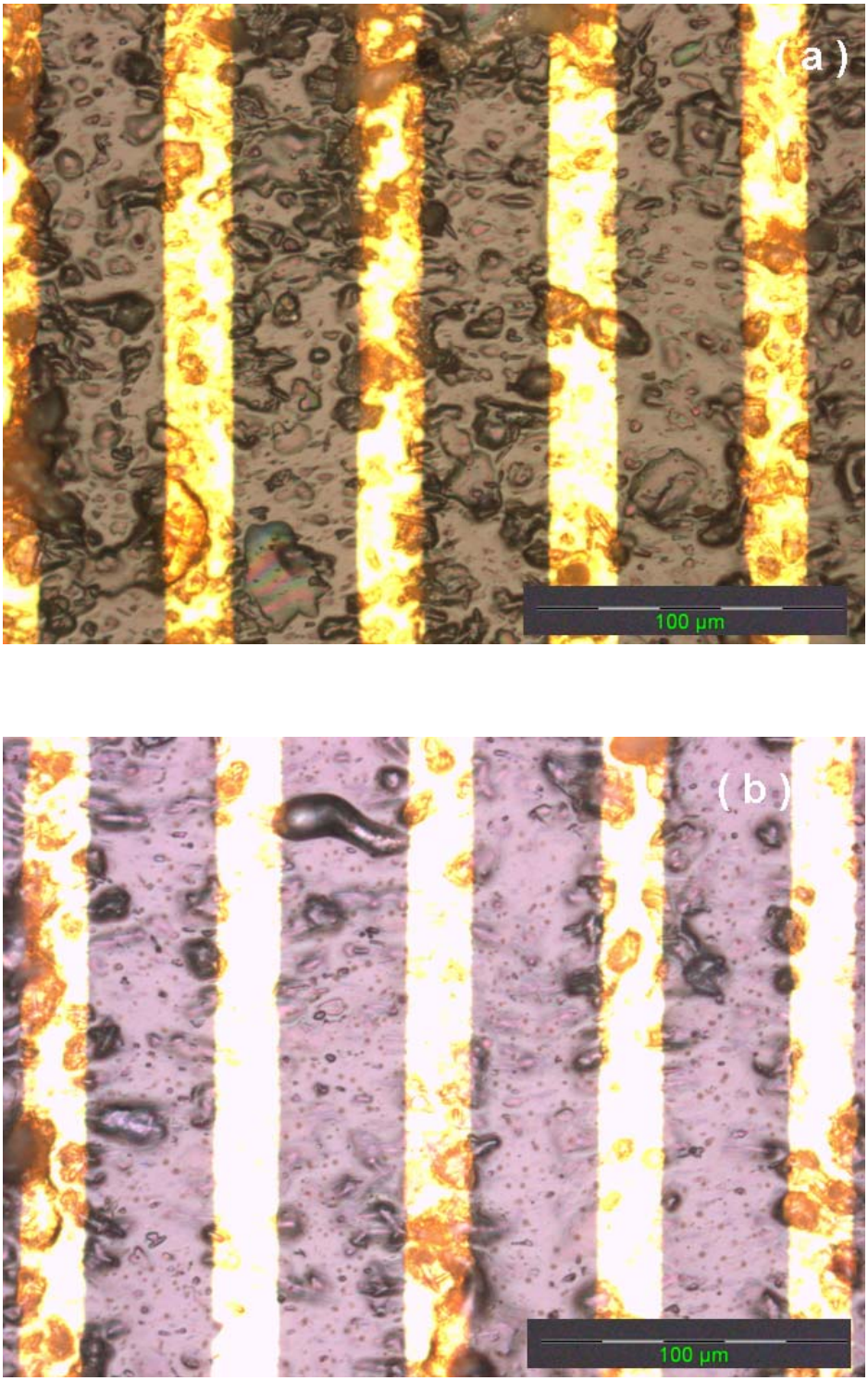


**Figure 5.14. O**ptical images of nanocomposites aligned by 10v AC voltages peak to peak and a frequency of 1000 Hz and different DC offset voltage of 2v under varying ZnO nanowires weight ratiowires. (a) 10%, (b) 5%.

## 5.3 CHARACTERIZATION OF ZNO-POLYIMIDE NANOCOMPOSITES

### 5.3.1 Characterization of nanocomposites from self-alignment method

Dielectric characterization of nanocomposite films provides us with a qualitative tool to analyze the dispersion of ZnO nanowires in the polyimide. The dielectric response of a polymer is a result of its capacitive nature (ability to store charge). The capacitance (Cp) of the composite could be given by:

$$C_p = \frac{Q}{V} = \frac{I_{out}}{V_{in}\omega}\sin(\theta) \qquad (3)$$

Where, Q is the charge on the capacitor under a voltage V, angular frequency $\omega = 2\pi f$ , where $f$ is the test frequency and $\theta$ is the phase angle.

The dielectric properties of the material are described by complex permittivity $\bar{\varepsilon}$. It has a real and a complex part given by

$$\bar{\varepsilon} = \varepsilon \ + j\varepsilon' \qquad (4)$$

$\varepsilon$ and $\varepsilon'$ are the dielectric constant and loss, respectively.

As we know that for a common two-plate capacitor, the capacitance (Cp) also could be written as in another format:

$$C_p = \frac{\varepsilon\ \varepsilon_0 A}{d} \qquad (5)$$

where $\varepsilon$ is the dielectric constant of the nanocomposite, A is electrode area, d is the thickness of the sample, and $\varepsilon_0$ is the permittivity of free space where $\varepsilon_0 = 8.854 \times 10^{-12}$ F/m. Since ZnO nanocomposites prepared by self-algnment method have a similar two parallel plate structure to

the normal capacitor. So we can rewrite equation (5) to get the dielelctric constant of the nanocomposite $\varepsilon$ like below:

$$\varepsilon = \frac{C_p d}{\varepsilon_0 A} \tag{6}$$

The dielectric loss is given by

$$\varepsilon' = D \cdot \varepsilon \tag{7}$$

$D$ is the dissipation factor.

Figure 5.15 shows the schematic of the experimental setup used to measure the capacitance of the ZnO nanocomposite films. The samples were prepared by the self-alignment method. The nanocomposite sample was then loaded in wafer holder of a magnetron sputtering system ATC1300 (AJA International, North Scituate, MA) and covered with a stainless shadow mask. The shadow mask was designed and fabricated with arrays of square geometry. 10nm thick Cr layer and 100nm thick Au electrode layer were direct-current (DC) sputtered to form the

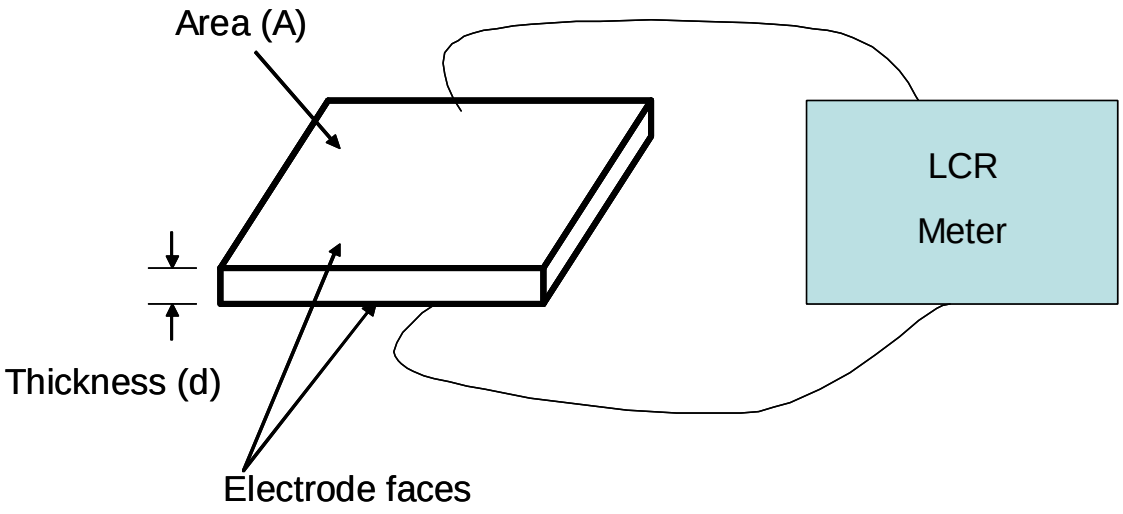


**Figure 5.15.** Measurement of dielectric properties of ZnO nanocomposites prepared by self-alignment method

top electrodes of the dielectric devices. The thickness (d) of the film was 5.6um, and the area (A) of top electrodes was $4mm^2$.

The dielectric constant and the loss tangent of the nanocomposite devices were measured at frequencies of 100Hz, 1 kHz, 10 kHz, 100 kHz, and 1 MHz, respectively, using an Agilent precision LCR Meter (model 4284A, Agilent Technologies). The dielectric permittivity and loss versus frequency are plotted in figure 5.16. Addition of ZnO nanowires to the polymer has a dramatic effect on the dielectric constant and loss. At 1 KHz the dielectric constant of the nanocomposite increases by nearly 3 times of the pure polyimide. Meanwhile, it is noted that the dielectric permittivity decrease as the frequency increases from 100 Hz to 1MHz. As we know, dielectric constants of bulk ZnO and polyimide materials are 10.4 and 2.9 at frequency of 1KHz. Therefore, the addition of ZnO nanowires naturally has a contribution to the increment of dielectric constant of nanocomposites. Meanwhile, due to the nanometer scale of these ZnO nanowire inclusions, their high surface area and a distance between them which is comparable to the nano dimension, there is an increasing influence of the interface on the physical properties of composites. Thus the properties of the interface can become a large influence on the dielectric properties of the nanocomposites.

For the tangent loss, the nanocomposite is also much higher than the pure polymer and significantly changes in the low frequency range, which has the maximum magnitude at 100Hz. When the frequency is more than 100 KHz, it becomes stable again. Why the nanocomposite has worse tangent loss? One possible reason is due to the increasing leakage current induced by addition of ZnO nanowires.

The room temperature *IV* characteristic of the device was measured by a Keithley 238 high current source measure unit (Keithley Instrument Inc.). The result in figure 5.17 shows that

the pure polyimide film device is insulated. When inclusions of ZnO nanowires were added into the polymer, the conductivity of the nanocomposite device was significantly increased compared to the pure polymer film.

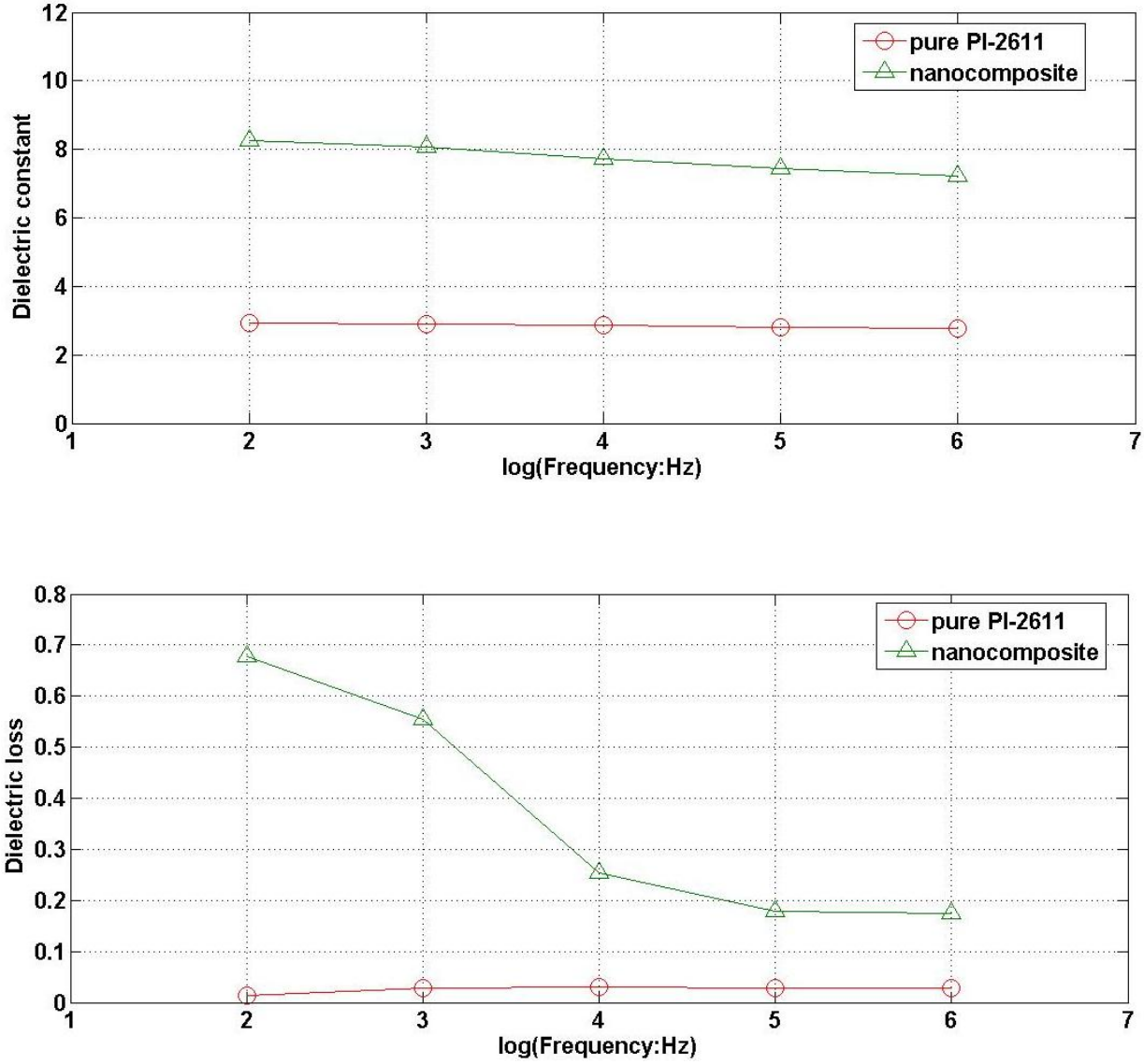


**Figure 5.16.** Dielectric constant and loss as a function of frequency for ZnO nanocomposites prepared by self-alignment method

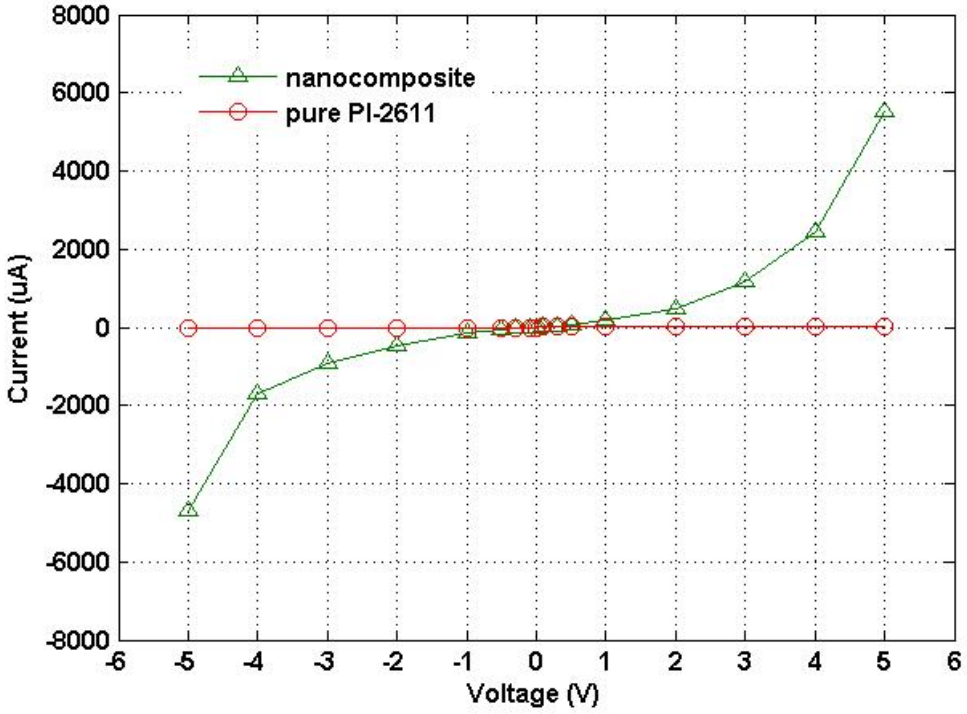


**Figure 5.17.** *IV* characteristic of ZnO nanocomposites prepared by self-alignment method

### 5.3.2 Characterization of nanocomposites from electric field assisted alignment method

The dielectric characteristics of ZnO nanocomposites prepared by electric field assisted alignment method were also studied. This kind of dielectric device is fabricated on an interdigitated electrode array. The structure of the device is different from the common two-plate capacitor. Due to symmetry of the field distribution near interdigitated electrodes, the whole system of interdigitated electrodes can be modeled as just two electrodes of width d and length, $L = l \cdot n$ ($l$ is IDT finger length, n is finger pairs) each with positive surface charge, +σ, and negative surface charge, -σ. The electric field in an isotropic dielectric can be approximated as

$$E = \frac{V}{\pi r} \qquad (8)$$

where r is the radial distance from the point located equidistance from either electrode [82]. Electrode charge density σ can be defined in terms of the electric field near the electrode surface

$$\sigma = 2\varepsilon_0 \varepsilon E \tag{9}$$

where $\varepsilon$ is dielectric constant of the material. The differential charge on the surface can be written as

$$dQ = \sigma L \cdot dr \tag{10}$$

Total charge, Q, can be obtained through integrating the charge over the electrode surface. The capacitance $C_p$ is determined from the relationship between the charge on the surface and the potential between the two electrodes [83]

$$C_p = \frac{Q}{V} = \frac{1}{V}\int_a^{2a} dQ = \ln 4 \frac{\varepsilon_0 \varepsilon L}{\pi} \tag{11}$$

So we can rewrite equation (11) to get the dielelctric constant of the nanocomposite $\varepsilon$ like below:

$$\varepsilon = \frac{\pi \cdot e^{C_p}}{4\varepsilon_0 L} \tag{12}$$

The dielectric loss is same as given by equation (7): $\varepsilon^{'} = D \cdot \varepsilon$

The schematic measurement setup of the dielectric nanocomposite devices is shown figure 5.18. First, 5 pairs of Cr/Au interdigitated electrodes were deposited on the polyimide thin film using a magnetron sputtering system ATC1300 (AJA International, North Scituate, MA) with a stainless shadow mask, where the finger length and gap was 12mm and 370μm, respectively. Cr thin film was 10nm thick as the adhesive layer and Au thin film was 100nm thick as the electrode. Then, micro tailored ZnO nanocomposite was prepared on the substrate with the external electric field assisted alignment method. Here, weight ratio of polyimide PI-

2611 and solvent T9039 was 1:1 and 5 wt% of ZnO nanowires was used as the inclusion. The magnitude and the frequency of the applied ac electric field were 120V and 1000Hz. The DC offset voltage was 5V.

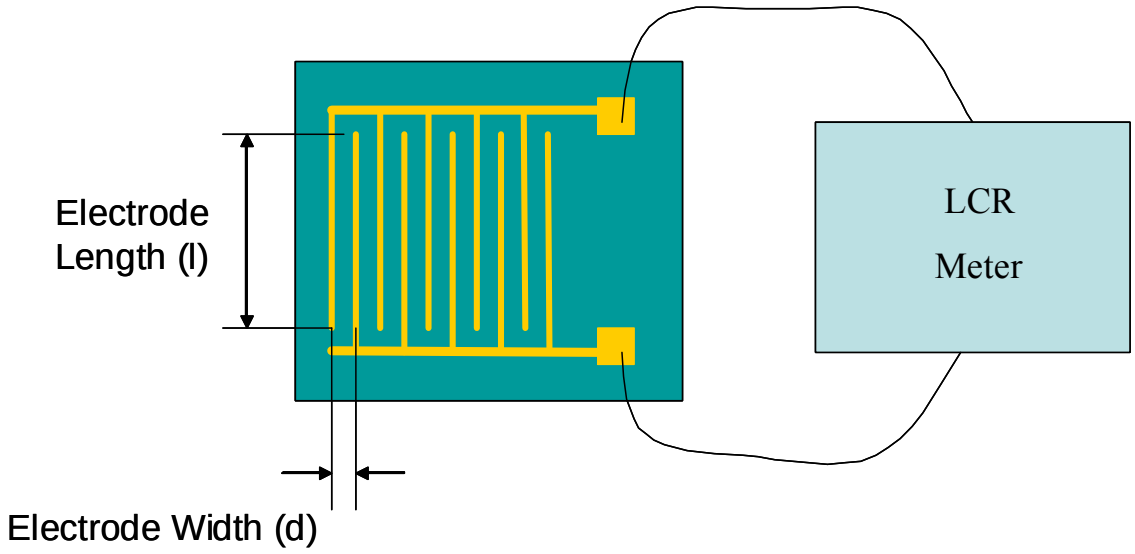


**Figure 5.18.** Schematic diagram of dielectric measurement setup for ZnO nanocomposites prepared by electric field alignment method

The dielectric capacitance and the loss tangent of the nanocomposite devices were measured using an Agilent precision LCR Meter (model 4284A, Agilent Technologies). Figure 5.19 shows the dielectric permittivity and loss versus frequency. It is found that the dielectric constant of the nanocomposite is much larger than the pure polyimide when ZnO nanowires were controlled dispersed in the polymer by the external electric field. At lower frequency, both nanocomposite and pure polyimide have bigger dielectric permittivity. As the frequency increases, both decrease and become stable finally. For the dielectric loss, the nanocomposite is also much larger than the pure polymer, especially at the low frequency. The higher dielectric

constant of nanocomposites also comes from both ZnO material itself and interfacial effects. The tangent loss is bigger due to leakage current induced by ZnO nanowires.

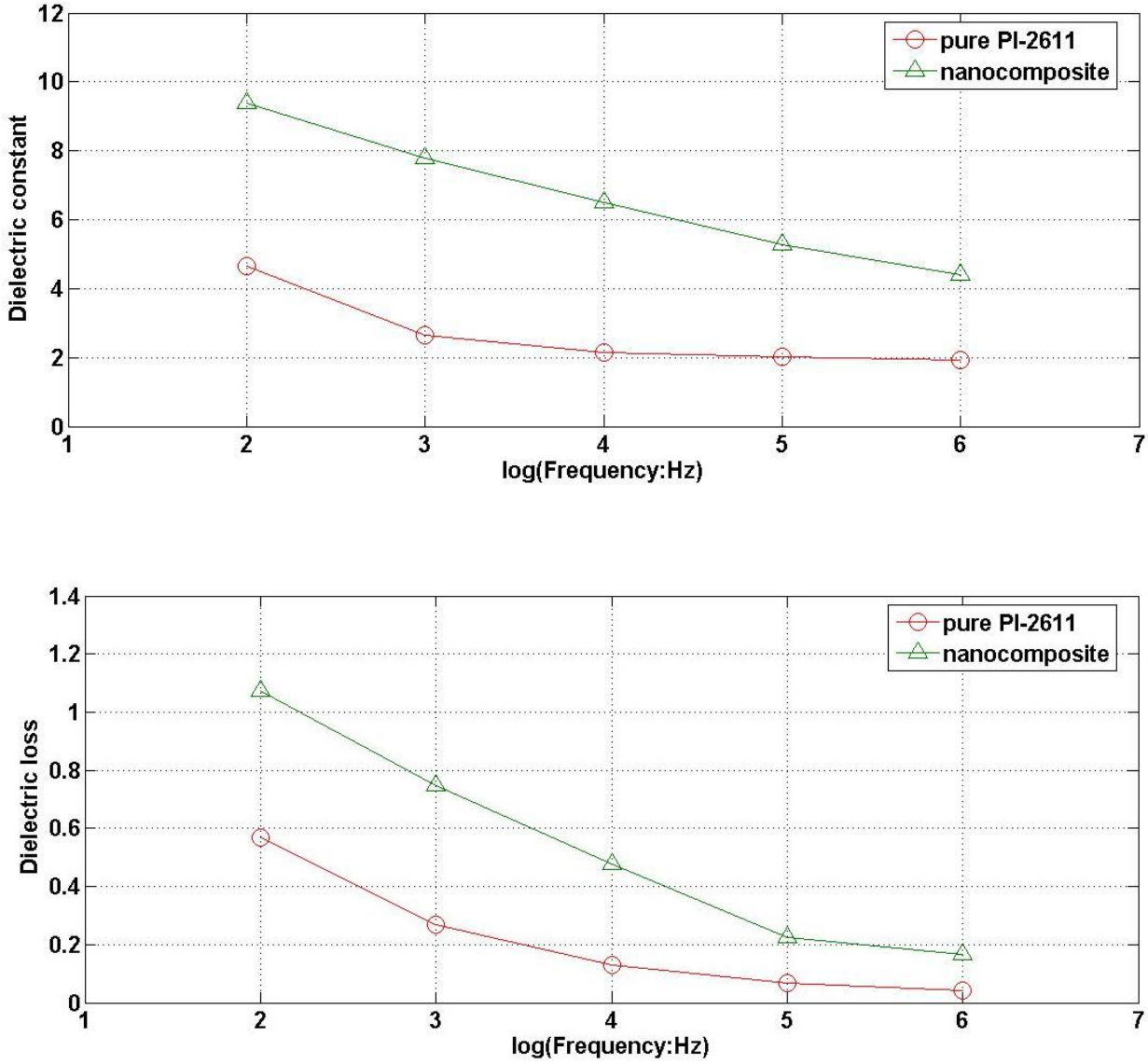


**Figure 5.19.** Dielectric constant and loss versus frequency for ZnO nanocomposites prepared by electric field alignment method

The room temperature *IV* characteristic of the device was measured by a Keithley 238 high current source measure unit (Keithley Instrument Inc.). Figure 5.20 shows that the pure polyimide film device is insulated. When ZnO nanowires were uniformly dispersed in the polyimide matrix assisted by the external electric field, the conductivity of the nanocomposite device was significantly increased.

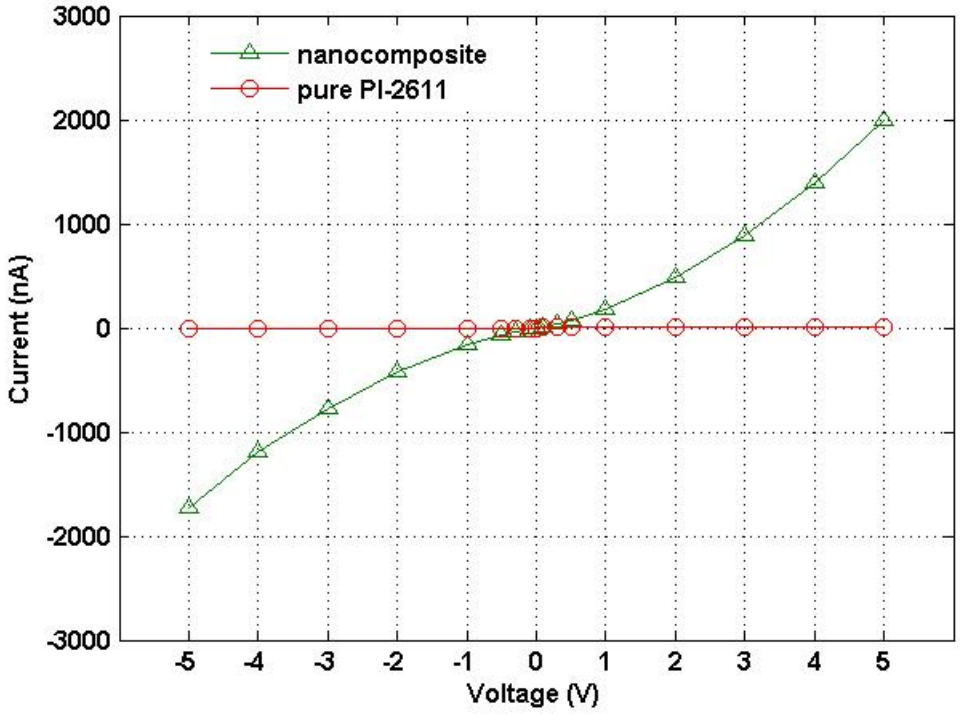


**Figure 5.20.** *IV* characteristic of ZnO nanocomposites prepared by electric field alignment method

## 5.4 CONCLUSIONS

In summary, the nanocomposite with controlled alignment of ZnO nanowires in the polyimide matrix was achieved using self-alignment method and external electric field assisted method. For the self-alignment process, the morphologies of the designed nanocomposites were dramatically influenced by the viscosity of the polymer and the geometrical structure of ZnO nanowires. For the nanocomposite prepared by the electric field assisted alignment, the density and the alignment degree of ordered ZnO nanowires significantly depended on the magnitude and the frequency of the applied ac electric field. The DC offset voltage had strong effect on the deposition sites of nanowires. The resultant nanocomposite devices exhibited great dielectric constant and conductivity enhancement at room temperature due to the interfacial effect between ZnO nanowires and the polymer matrix. These nanocomposites combing the superb properties of ZnO nanowires with the polyimide polymer matrix provide a smart material candidate for multifunctional applications that require self-sensing and self-actuation capabilities. The self-alignment method and electric field assisted alignment method provide a bright route to combine superb properties of nanomaterials with the lightweight, flexibility, and manufacturability of dielectric polymers for future generations of multifunctional materials. The novel nanocomposites prepared by those techniques will have tremendous impact in intelligent materials and structure applications, including piezoelectric sensors and actuators, biological sensors, structural health monitoring and vibration control in numerous industrial, civil, medical and aerospace applications.

# 6.0 CONCLUSIONS AND FUTURE WORK

## 6.1 SUMMARY OF ACCOMPLISHMENTS

The research in this dissertation is focused on investigating fabrication of one dimensional ZnO micro and nanostructures using microwave energy and meanwhile exploring their applications in gas sensing and multifunctional nanocomposites. The primary accomplishments of this research are listed below:

- A novel microwave thermal vapor deposition method was developed to grow one dimensional ZnO micro and nanostructures. This synthesis technique also can be used to fabricate nano/microstructures of many other semiconductors, such as GaN, $SnO_2$, and CdO.
- Large-scale ZnO microtubes, microrods, nanotubes, nanowires and nanobelts were fabricated in the microwave process system and the crystal structures were characterized using XRD and SEM. Those products are pure, structurally uniform, and single crystalline.
- Impacts of temperature, substrate, and catalyst on the controlled on-chip growth of those ZnO structures were studied. When the growth temperatures were below 1150°C, ZnO crystal wires or belts (with diameters from 50 nanometers to a few microns) were obtained; when the growth temperature exceeded 1300 °C, the hexagonal tubular growth became predominant. In addition, vertically well-aligned single crystal ZnO microrods can be achieved while the proper substrate sapphire (110) and the catalyst Au are selected.

- The photoluminescence (PL) of ZnO microtubes and microrods were measured and exhibited strong ultraviolet emission at room temperature, indicating potential applications for short-wave light-emitting photonic devices.
- The LGS resonator high temperature gas sensor was fabricated. The experimental results demonstrate that the combination of ZnO nanowire arrays with langasite thickness shear mode resonators could provide a promising high temperature gas sensing platform with both high sensitivity and enhanced response speed.
- Ordered ZnO nanowire arrays were grown on the langasite resonator as the sensitive layer by two-step hydrothermal method at low temperature. The gas sensor coated with ZnO nanowire arrays exhibited good gas sensing properties to $NO_2$ and $NH_3$. The reproducibility is good since the metal oxides are very stable. The response of the sensor is fast due to the huge surface area of ZnO nanowires.
- The designed nanocomposite with controlled alignment of ZnO nanowires in the polyimide matrix was achieved using self-alignment method and external electric field assisted method. The self-alignment method and electric field assisted alignment method provide a bright route to combine superb properties of nanomaterials with the lightweight, flexibility, and manufacturability of dielectric polymers for future generations of multifunctional materials.
- For the self-alignment process, effects of the viscosity of the polymer and the geometrical structure of ZnO nanowires on the morphology of the nanocomposites were investigated.
- For the electric field assisted alignment process, it was found that the density and the alignment degree of ordered ZnO nanowires significantly depended on the magnitude and the frequency of the applied ac electric field. The DC offset voltage had strong effect on the deposition sites of nanowires.

- The dielectric properties and conductivity of the resultant nanocomposite devices were characterized. The results exhibited great dielectric constant and conductivity enhancement at room temperature due to the interfacial effect between ZnO nanowires and the polymer matrix. These nanocomposites combing the superb properties of ZnO nanowires with the polyimide polymer matrix provide a smart material candidate for multifunctional applications that require self-sensing and self-actuation capabilities.

## 6.2 FUTURE WORK

One dimensional ZnO micro and nanostructures are attracting more research efforts worldwide. Using a novel microwave thermal vapor deposition technique, microtubes, microrods, nanowires, nanorods and nanobelts of ZnO have been synthesized under specific growth conditions. Future work needs to optimize the synthesis process to achieve controlled diameter, length, density of ZnO nanostructures in the microwave system. For high temperature gas sensors, future work needs to explore effects of temperature and morphology of ZnO nanostructure layer on gas sensing performance in more details. For ZnO nanocomposites, besides dielectric and conductive properties, other physical properties, such as photonic, piezoelectric, elastic, and piezoresistive property, need to be particularly studied. In addition, surface properties of ZnO nanowires, such as surface tension, morphology, and wettability of the polymer on the ZnO nanostructure need to be investigated for nanocomposite fabrication.

## BIBLIOGRAPHY


1. T. M. Parker, N. G. Condon, R. Lindsay, F. M. Leibsle, and G. Thornton, Imaging the polar $(000\bar{1})$ and non-polar $(1\,\bar{0}\,1)$ surfaces of ZnO with STM, Surface Science, Vol.415, pp. L1046-L1050, 1998.

2. W. L. Hughes and Z. L. Wang, Nanobelts as nanocantilevers, Applied Physics Letters, Vol. 82, pp. 2886-2888, 2003.

3. S. C. Minne, S. R. Manalis, and C. F. Quate, Parallel atomic force microscopy using cantilevers with integrated piezoresistive sensors and integrated piezoelectric actuators, Applied Physics Letter, Vol. 67, pp. 3918-3920, 1995.

4. C. R. Gorla, N. W. Emanetoglu, S. Liang, W. E. Mayo, Y. Lu, M. Wraback, and H. Shen, Structural, optical, and surface acoustic wave properties of epitaxial ZnO films grown on $(01\bar{1}2)$ sapphire by metalorganic chemical vapor deposition, Journal of Applied Physics, Vol. 85, pp. 2595-2602, 1999.

5. X. D. Wang, C. J. Summers, and Z. L. Wang, Large-scale hexagonal-patterned growth of aligned ZnO nanorods for nano-optoelectronics and nanosensor arrays, Nano Letters, Vol. 4, pp. 423-426, 2004.

6. Z. L. Wang, Zinc oxide nanostructures: growth, properties and applications, Journal of Physics: Condensed Matter, Vol.16, pp. R829-858, 2004.

7. M. H. Zhao, Nanomechanical and electromechanical characterization on zinc oxide nanobelt using atomic force microscopy, PhD thesis, Department of Mechanical Engineering, University of Pittsburgh, USA. 2004.

8. Z. Y. Fan, J. G. Lu, Zinc oxide nanostructures: synthesis and properties, Journal of Nanoscience and Nanotechnology, Vol. 5, pp. 1561-1573, 2005.

9. William L. Hughes, Synthesis and characterization of zinc oxide nanostructures for piezoelectric applications, PhD thesis, School of Materials Science & Engineering, Georgia Institute of Technology, 2006.

10. X. Y. Kong, and Z. L. Wang, Spontaneous polarization-induced nanohelixes, nanosprings, and nanorings of piezoelectric nanobelts, Nano. Letters, Vol.3, pp.1625, 2003.

11. P. Chang, Z. Fan, W. Tseng, D. Wang, W. Chiou, J. Hong, and J. G. Lu, ZnO nanowires synthesized by vapor trapping CVD method, Chemistry of Materials, Vol.16, pp. 5133, 2004.

12. W. I. Park, and G. C. Yi, Electroluminescence in n-ZnO nanorod arrays vertically grown on p-GaN, Advanced Materials, Vol.16, pp. 87, 2004.

13. M. H. Huang, Y. Wu, H. Feick, N. Tran, E. Weber, and P. Yang, Catalytic growth of zinc oxide nanowires by vapor transport, Advanced Materials, Vol. 13, pp. 113, 2001.

14. H. Q. Lee, S. J. Chua, K. P. Loh, E. A. Fitzgerald, and Y. W. Koh, Synthesis an optical properties of well aligned ZnO nanorods on GaN by hydrothermal synthesis, Nanotechnology, Vol. 17, pp. 483-488, 2006.

15. S. E. Ahn, J. S. Lee, K. Kim, S. Kim, B. H. Kang, K. H. Kim, and G. T. Kim, Photoresponse of sol-gel-synthesized ZnO nanorods, Applied Physics Letters, Vol. 84, pp. 5022-5024, 2004.

16. D. Clark, W.H. Sutton, Microwave processing of materials, Annual Review of Materials Science, Vol. 26, pp. 299-331, 1996.

17. J. D. Katz, Microwave sintering of ceramics, Annual Review of Materials Science, Vol. 22, pp. 153-170, 1992.

18. H. B. Cheng, J. P. Cheng, Y. J. Zhang, Q. M. Wang, Large-scale fabrication of ZnO micro-and nano-structures by microwave thermal evaporation deposition, Journal of Crystal Growth, Vol. 299, pp. 34-40, 2007.

19. Huankiat Seh, Langasite bulk acoustic resonant sensor for high temperature applications, PhD thesis, Department of Materials Science & Engineering, Massachusetts Institute of Technology, 2005.

20. D. S. Ballantine, R. M. White, S. J. Martin, A.J. Ricco, E.T. Zellers, G.C. Frye, and H. Wohltjen, Acoustic wave sensors: theory, design, and physical-chemical applications. Applications of modern acoustics, San Diego: Academic Press, 1997.

21. J. Zelenka, Piezoelectric Resonators and their Applications, New York: Elsevier, 1986.

22. S. J. Martin, G. C. Frye, J.J. Spates, and M. A. Butler, Gas sensing with acoustic devices, IEEE Ultrasonics Symposium Proceedings, pp. 423-434, 1996.

23. Milton Ohring, The materials science of thin films, Academic Press, Inc. (1992)

24. J. J. Luo, and I. M. Daniel, Characterization and modeling of mechanical behavior of polymer/clay nanocomposites, Journal of Composites Science & Technology, Vol. 63, pp. 1607–1616, 2003.

25. E.Thostenson, C. Li, and T. Chou, Review nanocomposites in context, Journal of Composites Science & Technology, Vol. 65, pp. 491–516, 2005.

26. D.Schmidt, D. Shah, and E.P. Giannelis, New advances in polymer/layered silicate nanocomposites, Current Opinion in Solid State and Materials Science, Vol. 6, pp. 205–212, 2002.

27. M. Alexandre, and P. Dubois, Polymer-layered silicate nanocomposites: Preparation, Properties and Uses of a new class of materials, Materials Science and Engineering, Vol.28, pp.1–63, 2000.

28. C. Park, O. Park, J. Lim, and H. Kim, The fabrication of syndiotactic polystyrene/ organophilic clay nanocomposites and their properties, Polymer, Vol. 42, pp. 7465–7475, 2001.

29. R.E. Gorga, and R.E. Cohen, toughness enhancements in poly(methyl methacrylate) by addition of oriented multiwall carbon nanotube, Journal of Polymer Science Part B-Polymer Physics, Vol. 42, pp. 2690–2702, 2004.

30. X. L. Xie, Y. W. Mai, and X. P. Zhou, Dispersion and alignment of carbon nanotubes in polymer matrix: A review, Materials Science and Engineering, Vol. 49, pp. 89, 2005.

31. B. Wang, Z. Y. Liang, Ravi Shankar, and Chuck Zhang, Electrical resistivity and mechanical properties of magnetically aligned SWNT, Conference paper, SAMPE - Long Beach, CA, pp. 16 – 20, May 2004.

32. Z. P. Zhou, D. Y. Wan, X. Y. Dou, L. Song, W. Y. Zhou, and S. S. Xie, Postgrowth alignment of SWNTs by an electric field, Carbon, Vol. 44, pp. 158, 2006.

33. T. Kimura, H. Ago, M. Tobita, S. Ohshima, M. Kyotani, and M. Yumura, Polymer composite of carbon nanotubes aligned by a magnetic field, Advanced Materials, Vol 14, pp. 1380-1383, 2002.

34. C. Park, J. Wilkinson, S. Banda, Z. Ounaies, K. E. Wise, G. Sauti, P. T. Lillehei, J. S. Harrison, Aligned single-wall carbon nanotube polymer composites using an electric field, Journal of Polymer Science Part B-Polymer Physics, Vol. 44, pp. 1751-1762, 2006.

35. T. D. Fornes, J. W. Baur, Y. Sabba, and E. L. Thomas, Morphology and properties of melt-spun polycarbonate fibers containing single- and multi-wall carbon nanotubes, Polymer, Vol. 47, pp. 1704, 2006.

36. Emilie J. Siochi, Dennis C. Working, Cheol Park, Peter T. Lillehei, Jason H. Rouse, Crystal C. Topping, Arup R. Bhattacharyya, Satish Kumar, Melt processing of SWCNT-polyimide nanocomposite fibers, Composites: Part B, Vo. 35, pp. 429, 2004.

37. Michael H. Huang, Samuel Mao, H. Feick, H. Yan, Y. Wu, H. Kind, E. Weber, R. Russo, and P. Yang, Room-Temperature Ultraviolet Nanowire Nanolasers, Science, Vol. 292, pp. 1897, 2001.

38. Q. Wan, Q. H. Li, Y. J. Chen, T. H. Wang, X. L. He, J. P. Li, and C. L. Lin, Fabrication and ethanol sensing characteristics of ZnO nanowire gas sensors, Applied Physics Letters, Vol. 84, pp. 3654, 2004.

39. M. Law, L. Greene, Justin C. Johnson, R. Saykally, and P. Yang, Nanowire dye-sensitized solar cells, Nature Materials, Vol. 4, pp. 455, 2005.

40. Y. B. Li, Y. Bando, and D. Golberg, ZnO nanoneedles with tip surface perturbations: Excellent field emitters, Applied Physics Letters, Vol.84, pp.3603, 2004.

41. Z. W. Pan, Z. R. Dai, and Z. L. Wang, Nanobelts of Semiconducting Oxides, Science , Vol.291, pp.1947, 2001.

42. J. P. Cheng, R. Y. Guo, and Q. M. Wang, Zinc oxide single-crystal microtubes, Applied Physics Letters, Vol.85, pp.5140, 2004.

43. J.Q. Hu, and Y. Bando, Growth and optical properties of single-crystal tubular ZnO whiskers, Applied Physics Letters, Vol.82, pp.1401, 2003.

44. G. H. Dua, F. Xu, Z. Y. Yuan, and G. Van Tendeloob, Flowerlike ZnO nanocones and nanowires: Preparation, structure, and luminescence, Applied Physics Letters, Vol.88, pp.243101, 2006.

45. V. K Varadan and J. N. Xie, Large-scale synthesis of multi-walled carbon nanotubes by microwave CVD, Smart Materials and Structures, Vol.11, pp.610-616, 2002.

46. P. Fons, K. Iwata, A. Yamada, K. Matsubara, S. Niki K. Nakahara, T. Tanabe, and H. Takasu, Uniaxial locked epitaxy of ZnO on the a face of sapphire, Applied Physics Letters, Vol.77, pp.1801, 2000.

47. G. W. Hunter, P. G. Neudeck, C. C. Liu, B. Ward, Q. H. Wu, P. Dutta, M. Frank, J. Trimbol, M. Fulkerson, and B. Patton, Development of chemical sensor arrays for harsh environments and aerospace applications, Proceedings of the IEEE Sensors, pp. 1126–1133, 2002.

48. J. Hornsteiner, E. Born, G. Fischerauer, E. Riha, Surface acoustic wave sensors for high temperature applications, IEEE International Frequency Control Symposium, pp. 615–620, 1998.

49. E. L. Belokoneva, M. A. Simonov, A. V. butashin, B. V. Mill, and N. V. Belov, Crystal structure of calcium gallogermanate $Ca_3Ga_4Ge_4O_{14}$=$Ca_3Ge[(Ga_2Ge)Ge_2O_{14}]$ and its analog $Ba_3Fe_2Ge_4O_{14}$=$Ba_3Fe_2[(FeGe_2)Ge_2O_{14}]$, Soviet Physics - Doklady, Vol. 27, pp. 954-957, 1980.

50. B. Chai, H. Qiu, Y. Y. Ji, and J. L. Lefaucheur. Growth of high quality single domain crystals of Langasite family Compounds, IEEE International Frequency Control Symposium, pp. 821-829, 1999.

51. A. A. Kaminskii, I. M. Silvestrova, S. E. Sarkisov, and G. A. Denisenko, Investigation of trigonal $(La_xNd_x)_3SiO_{14}$ crystals: II special laser and electromechanical properties, Physica Status Solidi (a), vol. 80, pp.607-620, 1983.

52. A. B. Ilyaev, B. S. Umarov, L. A. Shamanova, and M. F. Dubovik, Temperature dependence of electromechanical properties of LGS crystals, Physica Status Solidi (a), Vol. 98, pp. K109-114, 1986.

53. M. Sato, K. Moroishi, and S. Ishigami, Filter and resonator using Langasite, IEEE International Frequency Control Symposium, pp.379-383, 1996.

54. J. Detaint, J. Schwartzed, A. Zarka, B. Capelle, J. P. Denis, and E. Philippot, Bulk wave propagation and energy trapping in the new thermally compensated materials with trigonal symmetry, IEEE International Frequency Control Symposium, pp.58-71, 1994.

55. R. C. Smythe, R. C. Helmbold, G. E. Hague, and K. A. Snow, Langasite, langanite, and Langatate resonators: recent results, IEEE International Frequency Control Symposium, pp. 642-646, 1999.

56. A. N. Gotalskaja, D. I. Dresin, S. N. Schegolkova, N. I. Saveleva, V. V. Bezdelkin, and G. N. Cherpoukhina, Langasite crystal quality improvement aimed AT high-Q resonators fabrication, IEEE International Frequency Control Symposium, pp.657-666, 1995.

57. D. Richter, H. Fritze, T. Schneider, P. Hauptmann, N. Bauersfeld, K.-D. Kramer, K. Wiesner, M. Fleischer, G. Karle, and A. Schubert, Integrated high temperature gas sensor system based on bulk acoustic wave resonators, Sensors and Actuators B, Vol.118, pp. 466-471, 2006.

58. E. Ansorge, S. Schimpf, S. Hirsch, J. Sauerwald, H. Fritze, and B. Schmidt, Evaluation of langasite ($La_3Ga_5SiO_{14}$) as a material for high temperature microsystems, Sensors and Actuators A, Vol. 130-131: pp.393-396, 2006.

59. J. A. Thiele and M. Pereira da Cunha, High temperature LGS SAW gas sensor, Sensors and Actuators B, Vol.113, pp. 816-822, 2006.

60. R. C. Smythe, Material and resonator properties of langasite and langatate: a progress report, IEEE International Frequency Control Symposium, pp.761-765, 1998.

61. A. A. Kaminskii, B. V. Mill, G. G. Khodzhabagyan, A.F. Konstantinova, A.I. Okorochkov, and I. M. Silvestrova, Investigation of trigonal $(La_{1-x}Nd_x)_3Ga_5SiO_{14}$ crystals: I. Growth and optical properties, Physica Status Solidi (a), Vol. 80, pp.387-398, 1983.

62. N. Koshizaki, and T. Oyama, Sensing characteristics of ZnO-based NOx sensor, Sensors and Actuators B, Vol. 66, pp. 119-121, 2000.

63. S. J. Ippolito, S. Kandasamy, K. Kalantar-zadeh, W. Wlodarski, K. Galatsis, G. Kiriakidis, N. Katsarakis, and M. Suchea, Highly sensitive layered ZnO/LiNbO3 SAW device with $InO_x$ selective layer for $NO_2$ and $H_2$ gas sensing, Sensors and Actuators B, Vol. 111, pp. 207-212, 2005.

64. S. J. Ippolito, S. Kandasamy, K. Kalantar-Zadeh, and W. Wlodarski, Layered SAW hydrogen sensor with modified tungsten trioxide selective layer, Sensors and Actuators B, Vol. 108, pp. 553-557, 2005.

65. G. S. T. Rao, and D. T. Rao, Gas sensitivity of ZnO based thick film sensor to $NH_3$ at room temperature, Sensors and Actuators B, Vol. 55, pp. 166-169, 1999.

66. Z.L. Wang, Nanobelts, nanowires, and nanodiskettes of semiconducting oxides - from materials to nanodevices, Advanced Materials, Vol. 15, pp. 432-436, 2003.

67. Z.P. Sun, L. Liu, L. Zhang, and D. Z. Jia, Rapid sythesis of ZnO nano-rods by one-step, room temperature, solid-state reaction and their gas-sensing properties, Nanotechnology , Vol. 17, pp. 2266-2270, 2006.

68. L. Greene, M. Law, D. Tan, M. Montano, J. Goldberger, G. Somorjai, and P. Yang, General route to vertical ZnO nanowire arrays using textured ZnO seeds, Nano letters, Vol. 5, pp. 1231-1236, 2005.

69. B. Ruhland, Th. Becker, and G. Muller, Gas-kinetic interactions of nitrous oxides with $SnO_2$ surfaces, Sensors and Actuators B, Vol. 50, pp. 85–94, 1998.

70. C. S. Rout, K. Ganesh, A. Govindaraj, and C.N.R. Rao, Sensors for the nitrogen oxides, $NO_2$, NO and $N_2O$, based on $In_2O_3$ and $WO_3$ nanowires, Applied Physics A, Vol. 85, pp. 241–246, 2006.

71. M. S. Wagh, G. H. Jain, D. R. Patil, S. A. Patil, and L. A. Patil, Modified zinc oxide thick film resistors as $NH_3$ gas sensor, Sensors and Actuators B, Vol. 115, pp. 128–133, 2006.

72. C. Sanchez, B. Julian, P. Belleville, and M. Popall, Applications of hybrid organic–inorganic nanocomposites, J. Mater. Chem., Vol. 15, pp. 3559, 2005.

73. K. Saunders, Organic Polymer Chemistry, Chapman & Hall, 1988.

74. K. Jordan, X. Li, O. Iroh, SPE ANTEC, pp. 2436-2439, 1999.

75. H.A. Pohl, Dielectrophoresis, Cambridge University Press, Cambridge, UK, 1978.

76. Tachung C. Yih, Ilie Talpasanu, Micro and Nano Manipulations for Biomedical Applications, Boston : Artech House, 2008.

77. L. Zheng, S. Li, J. P. Brody, P. J. Burke, Manipulating Nanoparticles in Solution with Electrically Contacted Nanotubes Using Dielectrophoresis, Langmuir, Vol. 20, pp. 8612, 2004.

78. X. Q. Chen, T. Saito, H. Yamada, and K. Matsushige, Aligning single-wall carbon nanotubes with an alternating-current electric field, Applied Physics Letters, Vol. 78, pp.3714, 2001.

79. P. A. Smith, C. D. Nordquist, T. N. Jackson, T. S. Mayera, B. R. Martin, J. Mbindyo, and T. E. Mallouk, Electric-field assisted assembly and alignment of metallic nanowires, Applied Physics Letters, Vol. 77, pp. 1399, 2000.

80. D. Q. Wang, R. Zhu, Z. Y. Zhou, and X. Y. Ye, Controlled assembly of zinc oxide nanowires using dielectrophoresis, Applied Physics Letters, Vol. 90, pp. 103110, 2007.

81. H. W. Seo, C. S. Han, D. G. Choi, K. S. Kim, and Y. H. Lee, Controlled assembly of single SWNTs bundle using dielectrophoresis, Microelectronic Engineering, Vol 81, pp.83, 2005.

82. E. O. Doebelin, Measurement systems: application and design, 4 ed. McGraw-Hill, Inc., 1990.

83. T. R. Filanc-Bowen, G. H. Kim, Y. M. Shkel, Novel sensor technology for shear and normal strain detection with generalized electrostriction, Proceedings of IEEE Sensors, pp. 1648, 2002.